

AD-A094 438

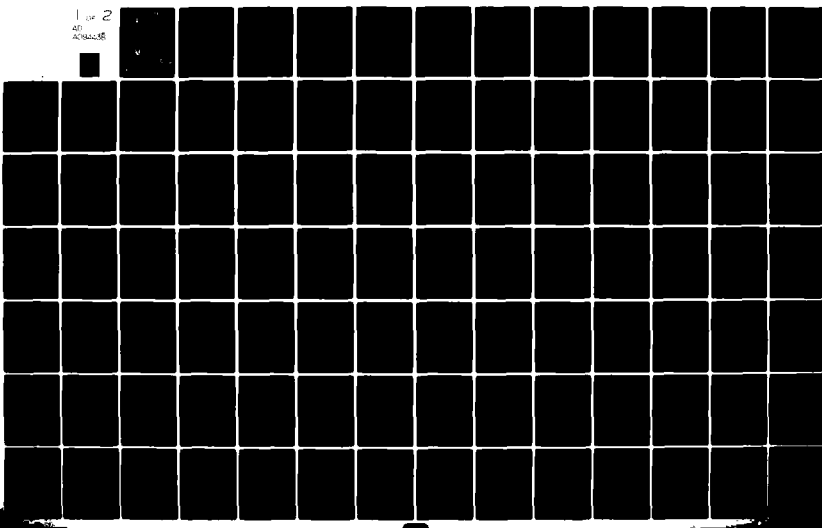
ARMY MISSILE COMMAND REDSTONE ARSENAL AL SYSTEMS SI--ETC F/6 12/1
TURBULENCE MODEL COMPARISONS FOR SHEAR LAYERS AND AXISYMMETRIC --ETC(U)
OCT 79 B J WALKER
DRSMI/RD-80-1-TR

UNCLASSIFIED

SBIE-AD-E950 074

NL

1 of 2
AD-A094 438



AD A094438

AD-E950074

14

LEVEL III

TECHNICAL REPORT RD-80-1

TURBULENCE MODEL COMPARISONS FOR
SHEAR LAYERS AND AXISYMMETRIC JETS

B.J. Walker
Systems Simulation and Development Directorate
US Army Missile Laboratory

October 1979



U.S. ARMY MISSILE COMMAND
Redstone Arsenal, Alabama 35809

Approved for public release; distribution unlimited.

DTIC
ELECTED
FEB 3 1981
S D
B

DEC FILE COFL

SMI FORM 1021, 1 JUL 79 PREVIOUS EDITION IS OBSOLETE

81 2 02 165

DISPOSITION INSTRUCTIONS

**DESTROY THIS REPORT WHEN IT IS NO LONGER NEEDED. DO NOT
RETURN IT TO THE ORIGINATOR.**

DISCLAIMER

**THE FINDINGS IN THIS REPORT ARE NOT TO BE CONSTRUED AS AN
OFFICIAL DEPARTMENT OF THE ARMY POSITION UNLESS SO DESIG-
NATED BY OTHER AUTHORIZED DOCUMENTS.**

TRADE NAMES

**USE OF TRADE NAMES OR MANUFACTURERS IN THIS REPORT DOES
NOT CONSTITUTE AN OFFICIAL INDORSEMENT OR APPROVAL OF
THE USE OF SUCH COMMERCIAL HARDWARE OR SOFTWARE.**

Unclassified

SECURITY CLASSIFICATION OF THIS PAGE (When Data Entered)

REPORT DOCUMENTATION PAGE		READ INSTRUCTIONS BEFORE COMPLETING FORM
1. REPORT NUMBER RD-80-1	2. GOVT ACCESSION NO. AD-H094138	3. RECIPIENT'S CATALOG NUMBER
4. TITLE (and Subtitle) Turbulence Model Comparisons for Shear Layers and Axisymmetric Jets	5. TYPE OF REPORT & PERIOD COVERED Technical Report	
7. AUTHOR(s) B.J. Walker	6. PERFORMING ORG. REPORT NUMBER	
9. PERFORMING ORGANIZATION NAME AND ADDRESS Commander US Army Missile Command ATTN: DRSMI-RDK Redstone Arsenal, Alabama 35809	10. PROGRAM ELEMENT, PROJECT, TASK AREA & WORK UNIT NUMBERS	
11. CONTROLLING OFFICE NAME AND ADDRESS Commander US Army Missile Command ATTN: DRSMI-RPT Redstone Arsenal, Alabama 35809	12. REPORT DATE October 1979	
14. MONITORING AGENCY NAME & ADDRESS (if different from Controlling Office)	13. NUMBER OF PAGES 133	
	15. SECURITY CLASS. (of this report) Unclassified	
	15a. DECLASSIFICATION/DOWNGRADING SCHEDULE	
16. DISTRIBUTION STATEMENT (of this Report) Approved for public release; distribution unlimited.		
17. DISTRIBUTION STATEMENT (of the abstract entered in Block 20, if different from Report)		
18. SUPPLEMENTARY NOTES		
19. KEY WORDS (Continue on reverse side if necessary and identify by block number) Rocket Exhaust Plume Pseudo-Vorticity Vortex Interactions Energy Dissipation Shear Flow		
20. ABSTRACT (Continue on reverse side if necessary and identify by block number) Comparisons were made between experiment and theory to assess the capability of turbulent mixing models to predict the fluid flow-properties in the mixing region of both shear layers and jets. Jets exiting into both moving and quiescent streams were investigated. Both chemically non-reacting and reacting shear layers were investigated. Attention was centered on two turbulence models: (i) $k\epsilon$ and (ii) $k\omega$. The same numerical flow field code was utilized with both turbulence models thus allowing a direct comparison of the		

Unclassified

SECURITY CLASSIFICATION OF THIS PAGE(When Data Entered)

20.

turbulence models without fear of differences in the numerics masking the results.

Results showed that significant errors can be made when utilizing these models for prediction of shear flows of interest. The flow structure for these shear flows is in no way accounted for by the models and hence poor predictions result. It is felt that the basic vortex structure will have to be modeled before significant improvements in the modeling will occur.

Accession For	
NTIS GRA&I	<input checked="" type="checkbox"/>
DTIC TIC	<input type="checkbox"/>
Unannounced	<input type="checkbox"/>
Justification	
By _____	
Distribution/	
Availability Codes	
Avail and/or	
Dist	Special
A	

Unclassified

SECURITY CLASSIFICATION OF THIS PAGE(When Data Entered)

CONTENTS

Section	Page
I. Introduction	7
II. Mathematical Flow Model	7
III. Startline Conditions	13
IV. $k\omega'$ Turbulence Model Formulation	23
V. Non-Reacting Shear Layer Comparisons	53
VI. Non-Reacting Jet Comparisons	69
VII. Reacting Shear Layer Comparisons	80
VIII. Conclusions	89
Appendix A — Location of the Dividing Streamline	97
Appendix B — Laminar Mixing Model	115
References	123
Symbols	125

ILLUSTRATIONS

Figure	Page
1. Compressibility Correction Factor for $k\epsilon$ 2 Turbulence Model	11
2. Boundary Layer Initial Profile	14
3. Shear Layer Initial Profile	16
4. Generalized Specific Profile	17
5. Results for Boundary Layer Initial profile	19
6. Results for Shear Layer Initial Profile	20
7. Results for Generalized Specific Profile	22
8. Comparison of Results Utilizing the Three (3) Input Methods for Determining the Initial Profile	31
9. Velocity Profile Comparison for Air/Air Shear Layer — <i>Table 6, Case Number I</i>	55
10. Velocity Profile Comparison for Air/Air Shear Layer — <i>Table 6, Case Number II</i>	56
11. ρu Profile Comparison for He/N ₂ Shear Layer — <i>Table 6, Case Number V</i>	58
12. Velocity Profile Comparison for He/N ₂ Shear Layer — <i>Table 6, Case Number III</i>	60
13. Density Profile Comparison for He/N ₂ Shear Layer — <i>Table 6, Case Number III</i>	61

ILLUSTRATIONS (Continued)

Figure	Page
14. Velocity Profile Comparison for He/N ₂ Shear Layer — <i>Table 6, Case Number IV</i>	62
15. Density Profile Comparison for He/N ₂ Shear Layer — <i>Table 6, Case Number IV</i>	63
16. Velocity Profile Comparison for He/N ₂ Shear Layer — <i>Table 6, Case Number V</i>	65
17. Density Profile Comparison for He/N ₂ Shear Layer — <i>Table 6, Case Number V</i>	66
18. Comparison of Calculated and Measured Effect of Density Ratio on Spreading Rate (k _ε 2 Turbulence Model)	67
19. Comparison of Calculated and Measured Effect of Density Ratio on Spreading Rate (Saffman k _ω ' Turbulence Model)	68
20. M _j = 2.2 Air Jet into Still Air. Comparison of k _ε 2 and k _ω ' Turbulence Models without Compressibility Centerline Velocity Profile	71
21. M _j = 2.2 Air Jet into Still Air. Comparison of k _ε 2 and k _ω ' Turbulence Models with Compressibility Centerline Velocity Profile	72
22. M _j = 2.2 Air Jet into Still Air. Comparison of k _ε 2 and k _ω ' Turbulence Models with Compressibility Radial Velocity Profile at x/r _j = 22.9	74
23. M _j = 2.2 Air Jet into Still Air. Comparison of k _ε 2 and k _ω ' Turbulence Models with Compressibility Radial Velocity Profile at x/r _j = 43.9	75
24. M _j = 2.2 Air Jet into Still Air. Comparison of k _ε 2 and k _ω ' Turbulence Models with Compressibility Radial Velocity Profile at x/r _j = 61.7	76

ILLUSTRATIONS (Continued)

Figure	Page
25. $M_j = 0.89$ H ₂ Jet Into $M_\infty = 1.32$ Air. Comparison of $k\epsilon 2$ and $k\omega'$ Turbulence Models with Compressibility Centerline Velocity Profile	77
26. $M_j = 0.89$ H ₂ Jet Into $M_\infty = 1.32$ Air. Comparison of $k\epsilon 2$ and $k\omega'$ Turbulence Models with Compressibility Radial Velocity Profile at $x/r_j = 11.02$	78
27. $M_j = 0.89$ H ₂ Jet Into $M_\infty = 1.32$ Air. Comparison of $k\epsilon 2$ and $k\omega'$ Turbulence Models with Compressibility Radial Velocity Profile at $x/r_j = 19.16$	79
28. $M_j = 0.89$ H ₂ Jet Into $M_\infty = 1.32$ Air. Comparison of $k\epsilon 2$ and $k\omega'$ Turbulence Models with Compressibility Radial Velocity Profile at $x/r_j = 30.88$	81
29. Two-Dimensional Reacting Shear Flow Schematic	82
30. Velocity Profile Comparison for Reacting Shear Layer — <i>Table 8, Case Number I</i>	85
31. Temperature Profile Comparison of Reacting Shear Layer — <i>Table 8, Case Number I</i>	86
32. Temperature Profile Comparison for Reacting Shear Layer — <i>Table 8, Case Number II</i>	87
33. Velocity Profile Comparison for Reacting Shear Layer — <i>Table 8, Case Number III</i>	88
34. Temperature Profile Comparison for Reacting Shear Layer — <i>Table 8, Case Number III</i>	90
35. Measured and Predicted Temperature Distribution for Reacting Shear Layer Resulting from Nitric Oxide and Ozone Combustion	91
36. Temperature Profile Prediction for Reacting Shear Layer Using Laminar Viscosity Model — <i>Table 8, Case Number III</i>	92

ILLUSTRATIONS (Concluded)

Figure	Page
37. Temperature Profile Prediction for Reacting Shear Layer Using Prandtl Mixing Length Turbulence Model -- <i>Table 8, Case Number III</i>	93
38. Temperature Profile Prediction for Reacting Shear Layer Using Donaldson Gray Eddy Viscosity, Turbulence Model — <i>Table 8, Case Number III</i>	94
A1. Plane Mixing Layer	99
A2. Plane Mixing Layer Fluid Element (Top Half)	99
A3. Plane Mixing Layer Fluid Element (Bottom Half)	101
A4. Checkout Program Listing for Dividing Streamline Location	104
A5. Checkout Program Listing for Dividing Streamline Location Plus Entrainment Integrals	109
B1. Program Listing for the Laminar Mixing Option Addition to the Shear Layer Program BOAT	118

TABLES

Table	Page
1. Experimental Turbulence Kinetic Energy Profile	21
2. Calculation of Turbulence Kinetic Energy Across Jet and External Boundaries Using Experimental Data From <i>Table 1</i>	24
3. Shear Layer Input Profile Data for Brown and Roshko He/N ₂ Experimental Run (<i>Figure 13a</i>)	25
4. Initial Profile for Brown and Roshko He/N ₂ Shear Layer (<i>Figure 13a</i>) — Boundary Layer Initialization	27
5. Initial Profile for Brown and Roshko He/N ₂ Shear Layer (<i>Figure 13a</i>) Specified Profile Initialization	29
6. Initial Conditions for Shear Layer Comparison Cases	57
7. Initial Conditions for Jet Mixing Comparison Cases	69
8. Initial Conditions for Reactive Shear Layer Comparisons	83

I. INTRODUCTION

In the development of a predictive tool for the fluid flow field due to the interaction of the rocket exhaust plume with its environment, the mixing region analysis is critical. The manner in which these streams interact and the accurate prediction of this interaction is paramount to several missile systems applications. Missile signature and vehicle design are two of the most important of these applications. In order to properly simulate the mixing region, the numerical calculational procedure must be accurate and the turbulence model must be physically correct. Having a physically correct turbulence model is certainly the most demanding of these two requirements.

Turbulence has been investigated for many years now and is usually characterized by its randomness and disorderliness. Despite the randomness and disorderliness however, statistically distinct average values are obtainable for the velocity, temperature, and density for example. The randomness and disorderliness is characterized by scale size. Not only is the fine scale characterized by vortex interactions but likewise for the large scale. This large scale motion has been studied intensively over the last several years by scientists at the California Institute of Technology and offers a better understanding of the physical phenomenology of turbulence.

II. MATHEMATICAL FLOW MODEL

The mathematical flow model utilized in this investigation consists of the axisymmetric jet mixing equations for a reacting gas mixture. This set of coupled partial differential equations is solved utilizing a mixed implicit/explicit finite difference procedure. The governing equations are parabolic and are solved in streamline coordinates using a marching scheme. This technology was essentially developed by the Joint Army, Navy, NASA and Air Force (JANNAF) Plume Technology Working Group in 1972 with the development of the Low-Altitude Plume Program (LAPP). Technology developments since that time have occurred and are being incorporated in the JANNAF Standardized Plume Flowfield (SPF) Program. The improvements to the mixing portion of this program include the employment of a discretized shear layer which grows due to the mixing of the jet and the external streams. This allows a more optimum placement of the grid points in the flowfield. Hence, this procedure of retaining the (x, ψ) computational grid and discretizing the shear layer has led to a much more efficient handling of the numerical procedures used to solve the problem. Other improvements such as the formulation of the energy equation in terms of total enthalpy rather than temperature leads to more accurate solutions in higher energy rocket propellants. In addition a mass flow check has been added to insure that mass flow is truly being conserved. This

model has been formulated by Aeronautical Research Associates of Princeton (ARAP) and constitutes a vital working portion of the SPI program being developed by them for the JANNAF Plume Technology Subcommittee. This code has been called BOAT in previous references in the literature [9]. Detailed derivations of the governing fluid dynamic equations utilized in this investigation can be found in the literature [9 - 12] and will only briefly be presented here. The governing equations are

Global Continuity

$$\frac{\partial}{\partial x} (\rho u) + \frac{1}{r} \frac{\partial}{\partial r} (\rho v r) = 0 \quad (1)$$

Species Diffusion

$$\rho u \frac{\partial F_i}{\partial x} + \rho v \frac{\partial F_i}{\partial r} = \frac{1}{r} \frac{\partial}{\partial r} \left(\frac{Le}{Pr} \mu r \frac{\partial F_i}{\partial r} \right) + \dot{w}_i \quad (2)$$

Axial Momentum

$$\rho u \frac{\partial u}{\partial x} + \rho v \frac{\partial u}{\partial r} = - \frac{\partial p}{\partial x} + \frac{1}{r} \frac{\partial}{\partial r} \left(\mu r \frac{\partial u}{\partial r} \right) \quad (3)$$

Energy

$$\begin{aligned} \rho u \frac{\partial H}{\partial x} + \rho v \frac{\partial H}{\partial r} &= \frac{1}{r} \frac{\partial}{\partial r} \left(\frac{\mu r}{Pr} \frac{\partial H}{\partial r} \right) + \\ \frac{1}{r} \frac{\partial}{\partial r} \left\{ \mu \left[1 - \frac{1}{Pr} \right] r u \frac{\partial u}{\partial r} \right\} &+ \frac{1}{r} \frac{\partial}{\partial r} \left\{ \frac{\mu}{Pr} (Le - 1) \right. \\ \left. \sum_i (h_i - h_i^0) r \frac{\partial F_i}{\partial r} \right\} \end{aligned} \quad (4)$$

State

$$\rho = \frac{P_{MW}}{RT} \quad (5)$$

These equations are then transformed from the (x,r) to the (x, ψ) coordinate system with the transformation

$$\psi \frac{\partial \psi}{\partial x} = \rho u x \quad (6)$$

$$\psi \frac{\partial \psi}{\partial x} = - \rho v r$$

Utilizing the transformation in (6), the governing equations become

Axial Momentum

$$\frac{\partial u}{\partial x} = - \frac{1}{\rho u} \frac{\partial p}{\partial x} + \frac{1}{\psi} \frac{\partial}{\partial \psi} \left(A \frac{\partial u}{\partial \psi} \right) \quad (7)$$

$$\text{where } A \equiv \mu_t \frac{\rho u r^2}{\psi}$$

Energy

$$\begin{aligned} \frac{\partial H}{\partial x} &= \frac{1}{\psi} \frac{\partial}{\partial \psi} \left\{ \frac{A}{Pr} \frac{\partial H}{\partial \psi} \right\} + \frac{1}{\psi} \frac{\partial}{\partial \psi} \left[A \left\{ 1 - \frac{1}{Pr} \right\} u - \frac{\partial u}{\partial \psi} \right] \\ &+ \frac{1}{\psi} \frac{\partial}{\partial \psi} \left\{ \frac{A}{Pr} (Le - 1) \sum_i (h_i - h_i^0) \frac{\partial F_i}{\partial \psi} \right\} \end{aligned} \quad (8)$$

Species Continuity

$$\frac{\partial F_i}{\partial x} = \frac{1}{\psi} \frac{\partial}{\partial \psi} \left(\frac{Le}{Pr} A \frac{\partial F_i}{\partial \psi} \right) + \frac{\dot{w}_i}{\rho u} \quad (9)$$

Two turbulence kinetic energy (TKE) models were used to determine the turbulent viscosity that appears in the governing equations. The first was the $K\epsilon 2$ model developed by Spalding and co-workers, and the second was the $k\omega'$ model developed by Saffman and co-workers. A detailed derivation of the latter model development for this investigation is given in Section IV of this report. Details of the $K\epsilon 2$ model can be found in other references [12].

The governing turbulence equations for the $k\epsilon$ 2 model are given by

$$\rho \frac{Dk}{Dt} = \frac{1}{r} \frac{\partial}{\partial r} \left\{ \frac{r\mu_t}{\sigma_k} \frac{\partial k}{\partial r} \right\} + \mu_t \left\{ \frac{\partial u}{\partial r} \right\}^2 - \rho \epsilon \quad \text{TKE} \quad (10)$$

$$\rho \frac{D\epsilon}{Dt} = \frac{1}{r} \frac{\partial}{\partial r} \left\{ \frac{r\mu_t}{\sigma_\epsilon} \frac{\partial \epsilon}{\partial r} \right\} + C_{\epsilon 1} \frac{\epsilon}{k} \mu_t \left(\frac{\partial u}{\partial r} \right)^2 - C_{\epsilon 2} \rho \frac{\epsilon^2}{k} \quad (11)$$

ENERGY
DISSIPATION
RATE

where

$$\mu_t = \frac{C_\mu \rho k^2}{\epsilon} \quad (12)$$

Note that this model utilizes five empirical constants — C_μ , $C_{\epsilon 1}$, $C_{\epsilon 2}$, σ_k , σ_ϵ .

For axisymmetric flows --

$$C_\mu = C_\mu \left\{ \frac{du}{dx} \Big|_{\frac{r}{k}}, \Delta u, \delta \right\} \quad (13)$$

$$C_{\epsilon 2} = C_{\epsilon 2} \left\{ \frac{du}{dx} \Big|_{\frac{r}{k}}, \Delta u, \delta \right\} \quad (14)$$

When these corrections are made to the constants, the model is known in the literature as the $k\epsilon 1$ turbulence model.

It was determined by exercising the model that the $k\epsilon 1$ model could not accurately predict weak shear flow, i.e., flow in which the two streams interacted at nearly the same velocities. Therefore a correction was made for weak shear flows by altering the constant C_μ as follows

For weak shear flows --

$$C_\mu = 0.09 G (\overline{P/\epsilon}) - 0.0534 F \quad (15)$$

where

$$F = F \left(\frac{du}{dx} \Big|_{\frac{1}{2}}, \Delta u, \delta \right)$$

$$\overline{P/\epsilon} = f n(k)$$

The resulting changes in the $k\epsilon$ 1 model were then known as the $k\epsilon$ 2 turbulence model and is utilized as such in this investigation.

In addition, the $k\epsilon$ 2 model does not contain any terms to handle compressibility effects. Hence, a compressibility correction was introduced into the model when large velocity differences between the mixing streams became important. The compressibility correction that was used resulted from an empirical formulation due to Dash [11]. The compressibility correction factor \bar{k} is multiplied by the constant C_μ and (12) becomes

$$\mu_t = \bar{k} \frac{C_\mu \rho k^2}{\epsilon} \quad (16)$$

where \bar{k} is a function of the maximum turbulence Mach number

$$M_{\tau \max} = \frac{\bar{k}_{\max}^{\frac{1}{2}}}{a} \quad (17)$$

The functional form of \bar{k} is shown in *Figure 1*.

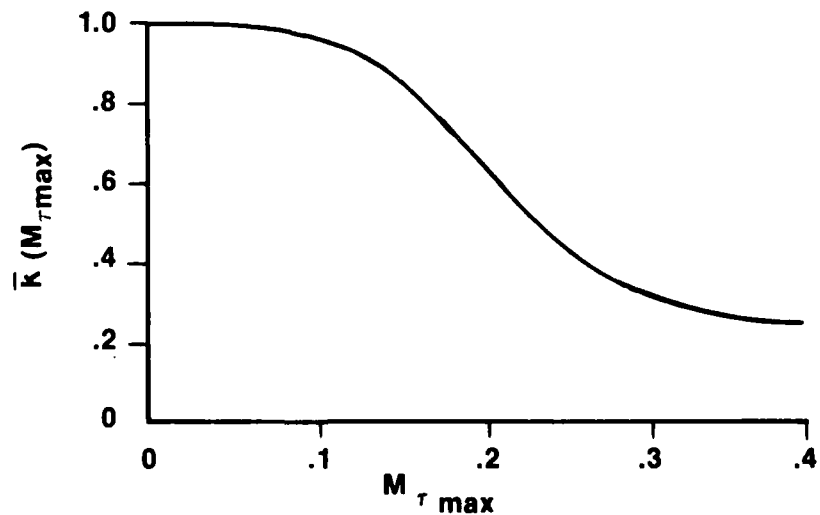


Figure 1. Compressibility correction factor for $k\epsilon$ 2 turbulence model.

The $k\omega'$ turbulence model was also utilized in this investigation. The governing equations for this model are developed in detail in Section IV, and are as follows

$$\rho \frac{Dk}{Dt} = \frac{1}{2r} \frac{\partial}{\partial r} \left\{ r \mu_t \frac{\partial k}{\partial r} \right\} + C_{k1} \omega \mu_t \left| \frac{\partial u}{\partial r} \right| - \rho k \omega \quad \text{TKE} \quad (18)$$

$$\begin{aligned} \rho \frac{D\omega}{Dt}^2 &= \frac{1}{2r} \frac{\partial}{\partial r} \left\{ r \mu_t \frac{\partial \omega}{\partial r}^2 \right\} + C_{\omega 2} \rho \omega^2 \left| \frac{\partial u}{\partial r} \right| \\ &+ C_{\omega 3} \frac{\omega}{\rho} \left(\frac{\partial \rho}{\partial r} \right) \frac{\partial}{\partial r} (\rho k) + C_{\omega 4} \rho \omega^3 \quad \text{PSEUDO-VORTICITY} \quad (19) \end{aligned}$$

where

$$\mu_t = \frac{C_{\omega 5} \rho k}{\omega} \quad (20)$$

This model also uses five constants, C_{k1} , $C_{\omega 2}$, $C_{\omega 3}$, $C_{\omega 4}$, $C_{\omega 5}$, and when compressibility effects are important, an additional term is included in the turbulence kinetic energy equation

$$\frac{C_{k6} \rho}{M_w e C_{pe} p_e} k \mu_t \left(\frac{\partial u}{\partial r} \right)^2 \quad (21)$$

These equations were transformed to the (x, ψ) coordinate system utilizing (6) and the following equations result from the transformation of (10) and (11).

For the $k\epsilon 2$ model

Turbulence Kinetic Energy (TKE)

$$\frac{\partial k}{\partial x} = \frac{1}{\psi} \frac{\partial}{\partial \psi} \left(\frac{A}{\sigma_k} \frac{\partial k}{\partial \psi} \right) + \frac{1}{u} (P - \epsilon) \quad (22)$$

Turbulence Dissipation

$$\frac{\partial \epsilon}{\partial x} = \frac{1}{\psi} \frac{\partial}{\partial \psi} \left(\frac{A}{\psi} - \frac{\partial u}{\partial \psi} \right) + \frac{\epsilon}{u k} \left(C_1 P - C_2 \epsilon \right) \quad (23)$$

where

$$A = \mu_t \frac{\rho u r^2}{\psi} \quad (24)$$

$$P = \frac{A u}{\psi} \left(\frac{\partial u}{\partial \psi} \right)^2 \quad (25)$$

Similarly for the $k\omega$ model (18) and (19) we transformed to the (x, ψ) coordinate system with the result that

Turbulence Kinetic Energy (TKE)

$$\begin{aligned} \frac{\partial k}{\partial x} &= \frac{1}{2\psi} \frac{\partial}{\partial \psi} \left\{ A \frac{\partial k}{\partial \psi} \right\} + C_1 \mu_t \omega \left| \frac{r}{\psi} \frac{\partial u}{\partial \psi} \right| \\ &- \frac{k \omega}{u} - \frac{C_{k6} \rho k A}{M_w C_p e^{\frac{p}{T_e}}} \left(\frac{\partial u}{\partial \psi} \right)^2 \end{aligned} \quad (26)$$

Turbulence Pseudo Vorticity

$$\begin{aligned} \frac{\partial \omega}{\partial x}^2 &= \frac{1}{2\psi} \left\{ A \frac{\partial \omega}{\partial \psi}^2 \right\} + \frac{C_{\omega2}^2}{u} \left| \frac{\rho u r}{\psi} \frac{\partial u}{\partial \psi} \right|^2 \\ &+ C_{\omega3} \frac{u r^2}{\psi} \left(\frac{\partial u}{\partial \psi} \right) \frac{\partial}{\partial \psi} (u k) + C_{\omega4} \frac{\omega^3}{u} \end{aligned} \quad (27)$$

where A is defined in (24).

When compressibility effects are not important, $C_{\omega3}$ is taken equal to zero. Hence, the compressibility term is built into the TKE equation.

III. STARTLINE CONDITIONS

Three methods were utilized to define the startline conditions which are used to initiate the finite difference calculational procedure. The three methods are:

- Boundary Layer Initial Profile
- Shear Layer Initial Profile
- Generalized Specific Profile

The first two methods employ calculational procedures to generate the initial profile. The third simply specifies the value of all the variables at some initial downstream location. Each of these methods was utilized to calculate the shear layer flowfield for the two dimensional He-N₂ case run experimentally by Brown and Roshko [1] for a density ratio of 1.1 and a velocity ratio of 7. This corresponds to the experimental data given in *Figure 13a* of reference [1].

A. Boundary Layer Initial Profile Description

The displacement effect of the jet and external boundary layers is calculated by utilizing a velocity profile that is derived from the combination of the "Law of the Wall" and the "Law of the Wake." *Figure 2* shows the applicable geometric configuration.

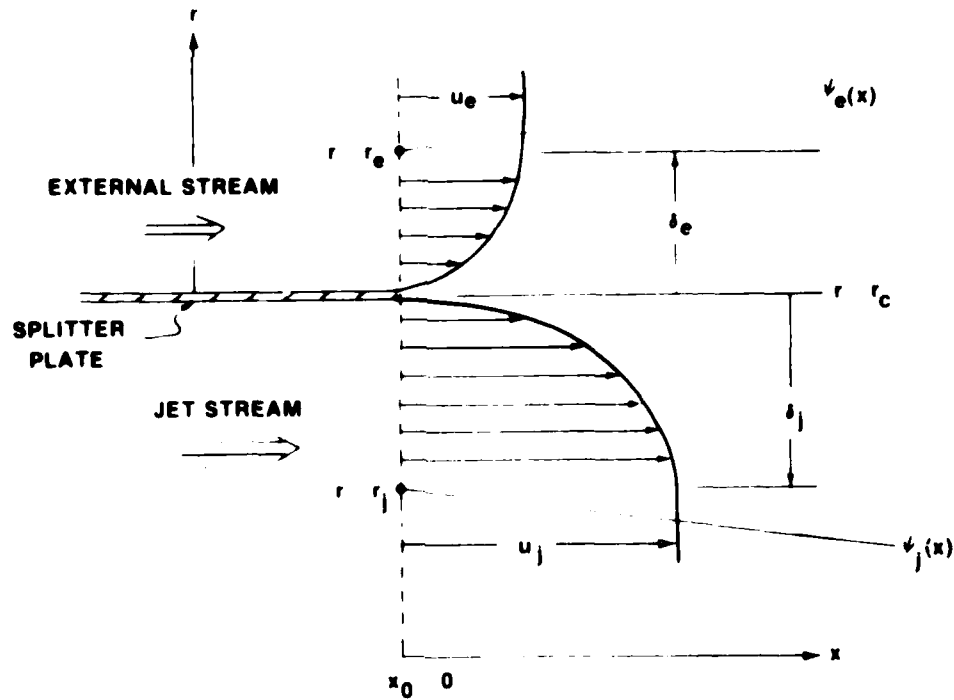


Figure 2. Boundary layer initial profile.

Note that the shear layer starts growing at $x = 0$ from $r_e = r_c + \delta_e$ on the external stream side and $r_j = r_c - \delta_j$ on the jet stream side. The profiles utilized to calculate these initial radii are computed from the velocity profiles

$$\frac{u_j - u}{u_{\tau_j}} = - 2.5 \ln \xi - 1.38 [2 - w(\xi)] \quad (28)$$

and

$$\frac{u_e - u}{u_{\tau_e}} = - 2.5 \ln \xi - 1.38 [2 - w(\xi)]$$

where $w(\xi)$ is Cole's universal wave function

$$w(\xi) = 1 + \sin \left\{ \frac{2\xi - 1}{2} \right\} \pi \quad (29)$$

and ξ is the non-dimensional radius

$$\xi = \frac{|r - r_c|}{\delta_j} \quad (30)$$

or

$$\xi = \frac{|r - r_c|}{\delta_e}$$

In addition, the frictional velocities

$$u_{\tau_e} = \sqrt{\frac{\tau_{w_e}}{\rho_e}} \quad (31)$$

or

$$u_{\tau_j} = \sqrt{\frac{\tau_{w_j}}{\rho_j}}$$

Now if the displacement thickness is known, then the definition of this quantity

$$\delta_j^* = \frac{1}{r_j} \int_{r_j}^{r_j + \delta_j} \left\{ 1 - \frac{(u_j) (MW_j) (T_j)}{(u_j) (MW_j) (T)} \right\} r dr \quad (32)$$

can be inverted to find δ_i provided U_i is also known. Similarly δ_e can be found and then r_i and r_e can be evaluated. Knowing these values, the initial distribution is determined

B. Shear Layer Initial Profile Description

For this method, a fully developed shear layer profile is assumed to exist at the initial streamwise location. The initial shear layer width is calculated from the incompressible relation [12]

$$r_e - r_j = 0.27 \left\{ \frac{u_j - u_e}{u_j + u_e} \right\} x_0 \quad (33)$$

Figure 3 illustrates this notation

Upon establishment of the shear layer upper and lower boundaries utilizing (33), the properties are distributed across the shear layer according to the simple cubic relations

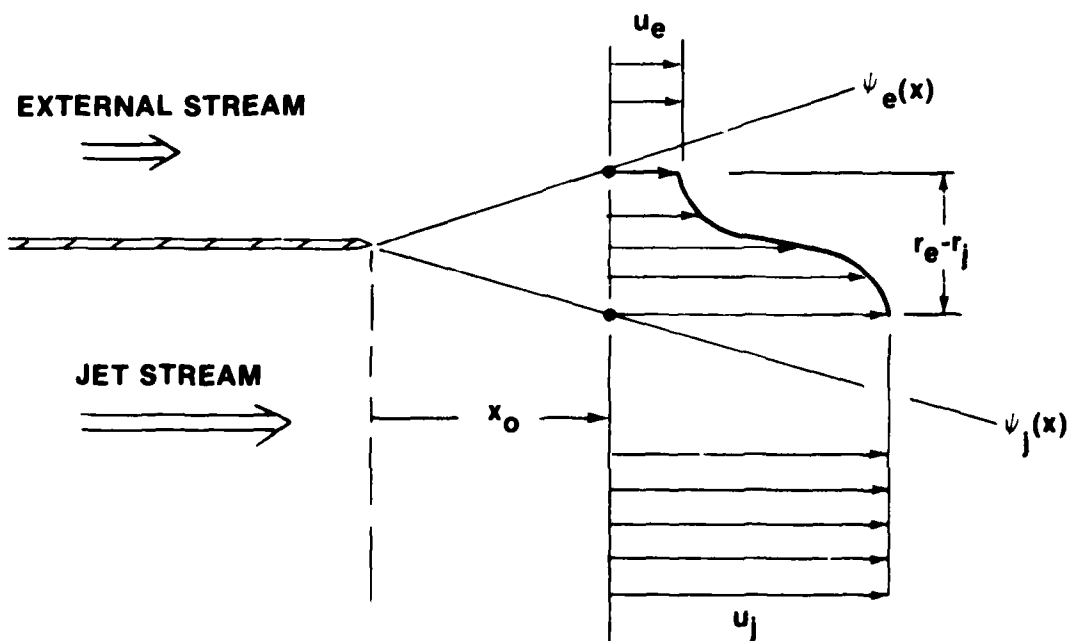


Figure 3. Shear layer initial profile.

$$\frac{u_i - u_j}{u_e - u_j} = \frac{T_i - T_j}{T_e - T_j} = \frac{F_{i_e} - F_{i_j}}{F_{i_e} - F_{i_j}} = 3\eta^2 \left\{ 1 - \frac{2\eta}{3} \right\} \quad (34)$$

where

$$\eta = \frac{r_i - r_j}{r_e - r_j}$$

The shear layer grid points are spaced evenly across it in increments of $\Delta\psi = \frac{\psi_e - \psi_j}{N - 1}$

C. Generalized Specific Profile Description

This method of inputting startline conditions does not rely on any calculations but merely uses the specified profile. *Figure 4* illustrates this case where $u(r), T(r)$, and $x(r)$ are input directly at the startline location $x = x_0$. This method can only be used in rare cases when a significant amount of experimental data is available.

In addition to these fluid dynamic initial conditions, an initial turbulence level must be supplied at the initial axial station x_0 . In the absence of known profiles for k and ϵ or ω' , the Prandtl mixing length model is used to define the turbulent shear stress in terms of the local velocity gradient utilizing the following relation

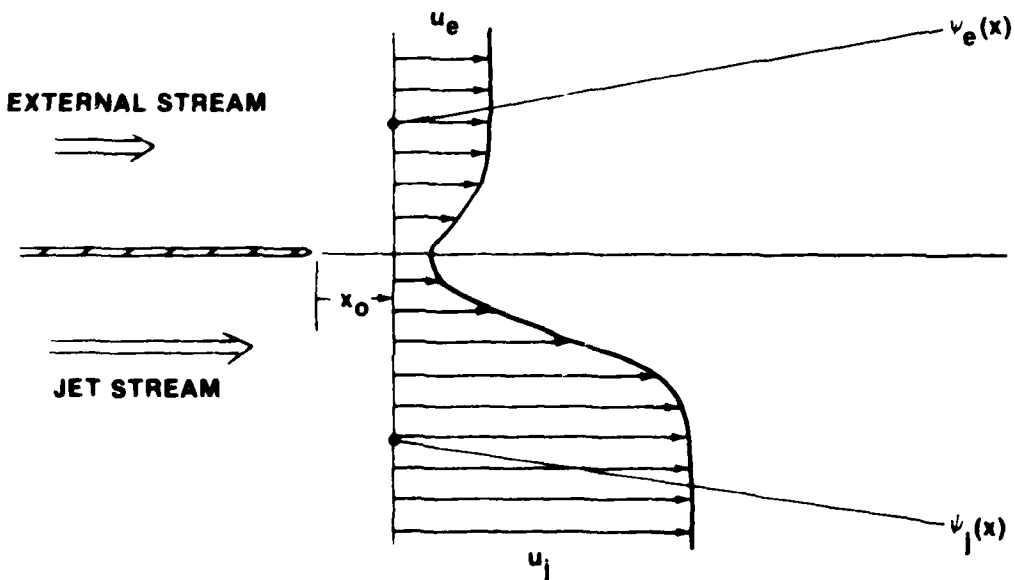


Figure 4. Generalized specific profile.

$$\rho \overline{u'v'} = \rho \ell^2 \left(\frac{\partial u}{\partial r} \right) \left| \frac{\partial u}{\partial r} \right| \quad (35)$$

and the relation between the shear stress and the turbulent energy [7]

$$k = \frac{\overline{u'v'}}{0.3} \quad (36)$$

D. Boundary Layer Initial Profile Results

For the He/N₂ shear layer of Brown & Roshko, the initial conditions should not affect the resulting similar profile far downstream of the initial station. This was examined by looking at the different methods of specifying the initial profile.

The use of the boundary layer initial profile was examined for the He/N₂ shear layer of Brown and Roshko for which the experimental velocity and density profiles are shown in Figures 16 and 17.

δ^* was determined from θ calculated by Brown and Roshko and the relation between these quantities for a flat plate, i.e.

$$\frac{\delta^*}{\theta} = \frac{1.7208 \text{ Re}^{\frac{1}{2}}}{0.664 \text{ Re}^{\frac{1}{2}}} = 2.592$$

Since the momentum thickness was found to be 0.001 inches and the splitter plate thickness was 0.002 inches, the displacement thickness utilized for this option was

$$\delta^* = \frac{(0.002)(2.592)}{12} = 4.318 \times 10^{-4} \text{ ft.}$$

The Re difference between the He and N₂ was not accounted for and the boundary layer displacement thickness was taken as the same for both the jet and the external stream, i.e.

$$\delta_j^* = \delta_e^* = 4.32 \times 10^{-4} \text{ ft.}$$

The resulting mixing profiles of the density and the velocity for the two dimensional shear layer are shown in Figure 6. These results are given at a distance downstream of x = 1.69 inches.

WJWDK BC
29 JAN 79

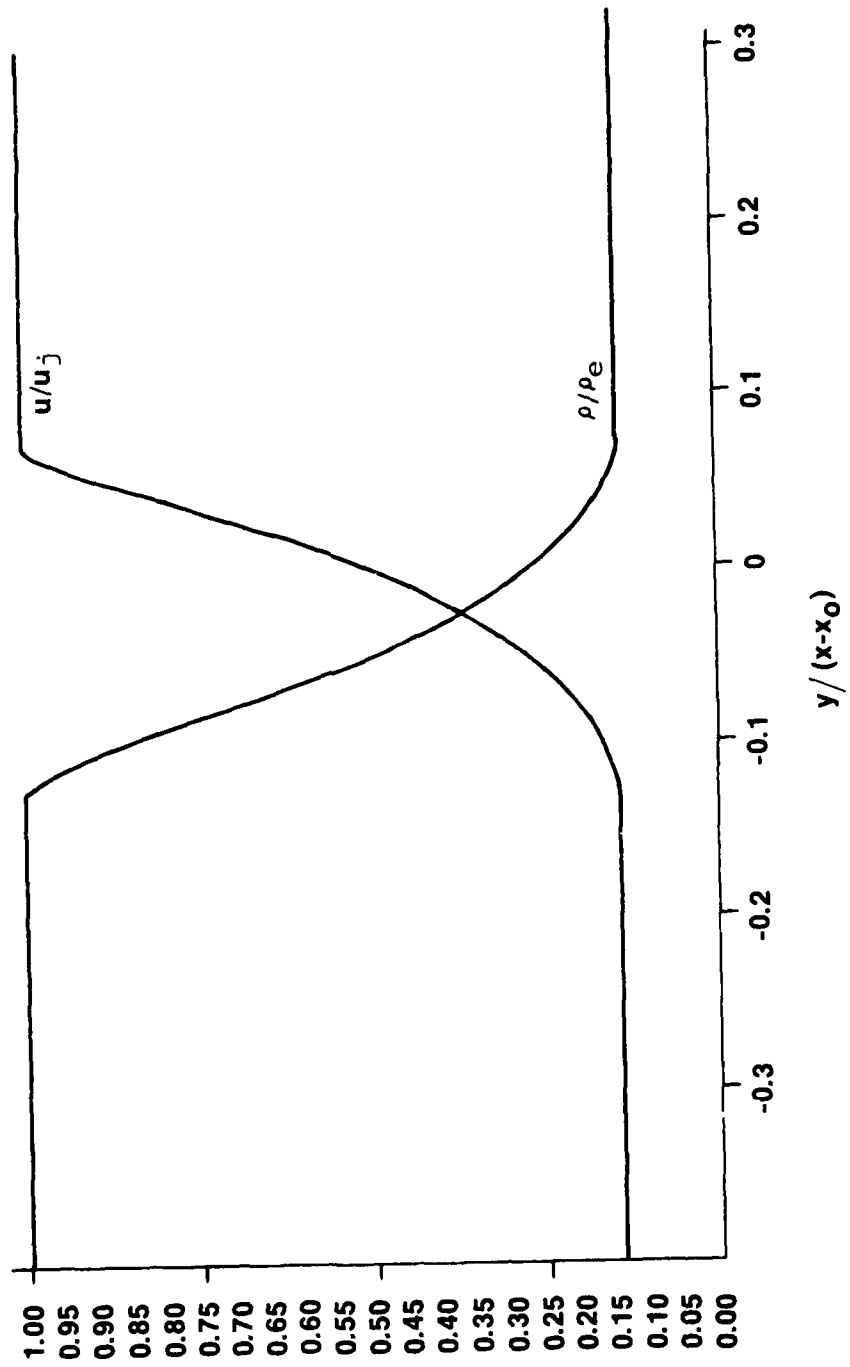


Figure 5. Results for boundary layer initial profile.

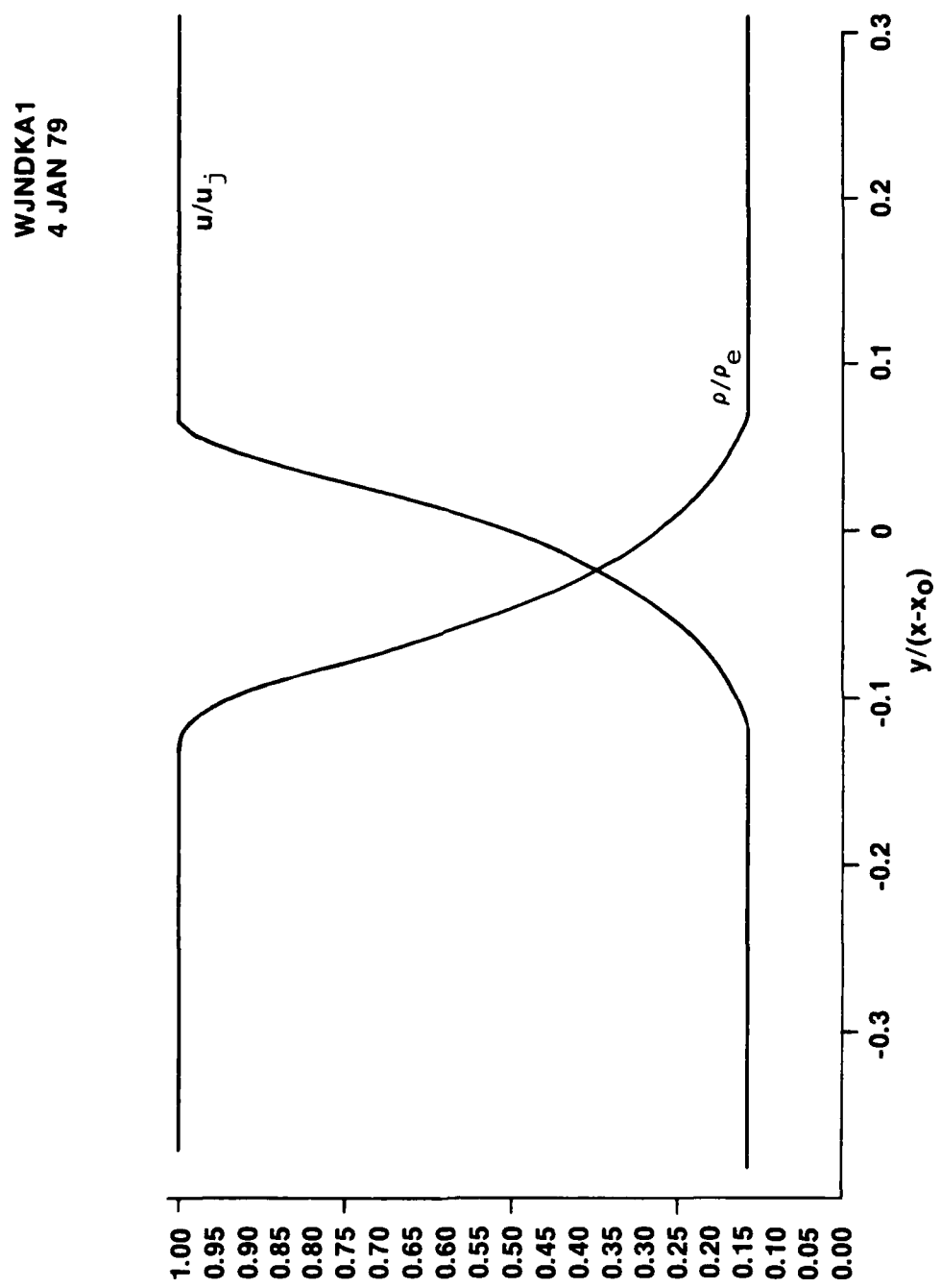


Figure 6. Results for shear layer initial profile.

E. Shear Layer Initial Profiles Results

This method was used to calculate the initial profile from which the finite difference solution was started and the results from this method are shown in *Figure 7*. The initial shear layer based on the cubic profile was calculated at $x = .01$ feet (8.33×10^{-4} inches) and calculations were started from that point. The $k\epsilon$ turbulence model was used in this calculation just as it was on the boundary layer initialization results given in Section D above. Note that these results are given for a position slightly further downstream $x = 1.81$ inches. This makes very little difference however, since the profiles have already achieved self-similarity.

F. Generalized Specific Profile Results

This method was also used to specify the initial profile to determine what differences in results occurred because of differences in the initial startline. For this option, the mean profile for the density and velocity were taken at $x = 0$ directly from the boundary layer initialization scheme described above. However, the turbulence kinetic energy profile at $x = 0$ was taken from experimental data rather than being calculated using the mixing length turbulence option described above.

The turbulence kinetic energy profile was taken from experimental data for flow over a flat plate. This data was taken from *Figure 5* of Klebanoff [3] and has been tabularized in *Table 1* as a function of y/δ where δ is the shear layer width.

TABLE 1. EXPERIMENTAL TURBULENT KINETIC ENERGY PROFILE

y/δ	u'/U_∞	v'/U_∞	w'/U_∞	$\frac{u'^2+v'^2+w'^2}{U_\infty^2}$	$\frac{1}{2} \left\{ \frac{u'^2+v'^2+w'^2}{U_\infty^2} \right\}$
0	.087	.032	.065	1.2818×10^{-2}	6.409×10^{-3}
0.1	.071	.040	.052	9.345×10^{-3}	4.673×10^{-3}
0.2	.066	.040	.050	8.456×10^{-3}	4.228×10^{-3}
0.3	.060	.038	.048	7.348×10^{-3}	3.674×10^{-3}
0.4	.056	.036	.046	6.548×10^{-3}	3.274×10^{-3}
0.5	.051	.033	.041	5.371×10^{-3}	2.686×10^{-3}
0.6	.042	.029	.035	3.830×10^{-3}	1.915×10^{-3}
0.7	.034	.022	.029	2.481×10^{-3}	1.241×10^{-3}
0.8	.021	.018	.021	1.206×10^{-3}	6.030×10^{-4}
0.9	.012	.012	.012	4.320×10^{-4}	2.160×10^{-4}
1.0	.007	.007	.007	1.470×10^{-4}	7.350×10^{-5}

WJWDK77
5 FEB 79

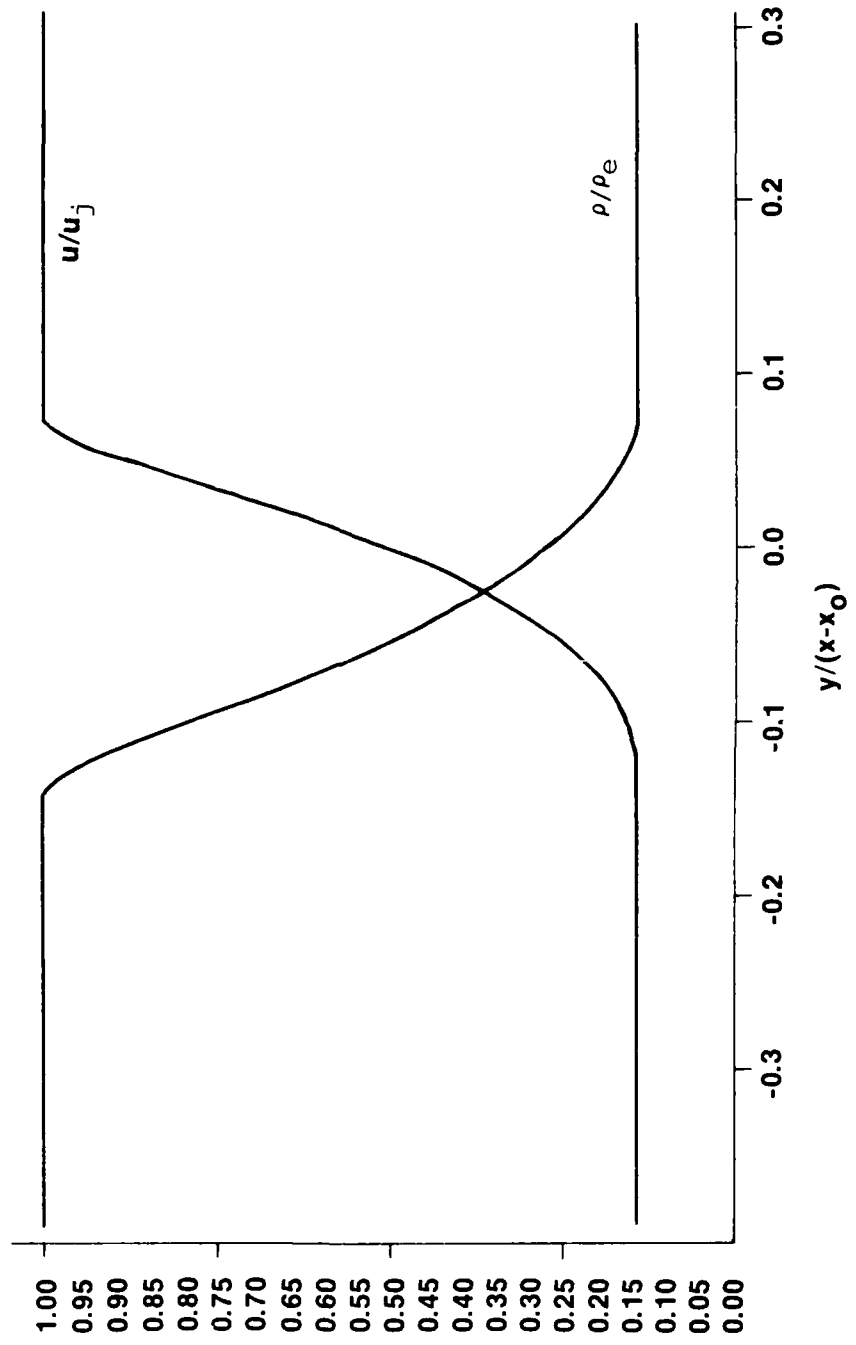


Figure 7. Results for generalized specific profile.

Next, the velocity profile that was generated at $x = 0$ using the boundary layer initialization scheme above is interpolated to obtain velocities at each y/δ location. This was done for both the jet boundary and the external boundary. These results are shown in *Table 2*. Also note that the initial shear layer thickness δ is taken from the boundary layer initialization scheme. The combination of the data for both the external and jet streams provide the specific shear layer profile data used to calculate the mixing layer. This is given in *Table 3*.

This is compared with the initial turbulence data which was calculated utilizing the mixing length model as described above. This initial profile expanded to 50 points across the shear layer is shown for the boundary layer initialization method in *Table 4* and for the specific profile method in *Table 5*.

Comparing *Table 4* with *Table 5* shows large differences in the turbulence kinetic energies for the calculated and input initialization schemes. Note that for the calculated scheme of *Table 4*, $0 \leq k \leq 792.6$ while the data based on experiment is in the range $0.079 \leq k \leq 5.657$. Hence, the turbulent intensity is down two orders of magnitude. Similarly, there are large changes noted in length scale parameter ϵ . However, when these shear layers have been calculated out to a distance of 1.69 inches, *Figure (7)* shows that the initial profile differences have washed out and the density and velocity profiles are virtually the same. *Figure (8)* was obtained from *Figures (5-7)*.

Therefore it has been shown that this calculational scheme is not sensitive to initial conditions when the behavior of the shear layer is examined far enough downstream where the flow becomes self similar. Hence, any of the initial profile methods may be used with confidence.

IV. $k\omega'$ TURBULENCE MODEL FORMULATION

In order to make meaningful comparisons of various turbulence models for use in rocket exhaust plumes, an investigation of several models was made. The following turbulence models were investigated:

- Prandtl mixing length
- Donaldson-Gray eddy viscosity

TABLE 2. CALCULATION OF TURBULENCE KINETIC ENERGY
ACROSS JET AND EXTERNAL BOUNDARIES USING
EXPERIMENTAL DATA FROM TABLE 1

JET BOUNDARY

y/δ	k/U_∞^2	U_∞	y^\dagger	k	u^\dagger	T
0.0	6.409×10^{-3}	32.81	10.00000	6.8992	0.0	300
0.1	4.673×10^{-3}	32.81	9.999847	5.0305	25.84	300
0.2	4.228×10^{-3}	32.81	9.999694	4.5514	27.462	300
0.3	3.674×10^{-3}	32.81	9.999541	3.9550	28.541	300
0.4	3.274×10^{-3}	32.81	9.999388	3.5244	29.449	300
0.5	2.686×10^{-3}	32.81	9.999235	2.8914	30.255	300
0.6	1.915×10^{-3}	32.81	9.999082	2.0615	30.980	300
0.7	1.241×10^{-3}	32.81	9.998929	1.3359	31.610	300
0.8	6.030×10^{-4}	32.81	9.998776	0.6491	32.136	300
0.9	2.160×10^{-4}	32.81	9.998623	0.2325	32.536	300
1.0	7.350×10^{-5}	32.81	9.99847	0.0791	32.810	300

EXTERNAL BOUNDARY

y/δ	k/U_∞^2	U_∞	y	k	u^\dagger	T
0.0	6.409×10^{-3}	4.69	10.00000	0.14097	0.0	300
0.1	4.673×10^{-3}	4.69	10.00015	0.10279	3.6915	300
0.2	4.228×10^{-3}	4.69	10.00030	0.09300	3.9241	300
0.3	3.674×10^{-3}	4.69	10.00045	0.08081	4.0800	300
0.4	3.274×10^{-3}	4.69	10.00060	0.07202	4.2094	300
0.5	2.686×10^{-3}	4.69	10.00075	0.05908	4.3247	300
0.6	1.915×10^{-3}	4.69	10.00090	0.04212	4.4283	300
0.7	1.241×10^{-3}	4.69	10.00105	0.02730	4.5186	300
0.8	6.030×10^{-4}	4.69	10.00120	0.01326	4.5933	300
0.9	2.160×10^{-4}	4.69	10.00135	0.00475	4.6508	300
1.0	7.350×10^{-5}	4.69	10.00150	0.00162	4.6900	300

[†]From the He/N₂ B.L. initialization output-

$$\delta_{JET} = 10.0000 - 9.9985 = 1.5 \times 10^{-3} \text{ ft (0.018 inches)}$$

$$\delta_{EXT} = 10.0020 - 10.0000 = 2.0 \times 10^{-3} \text{ ft (0.024 inches)}$$

UNITS: y - in.; U - ft/sec; k - ft^2/sec^2 ; T - °K.

TABLE 3. SHEAR LAYER INPUT PROFILE DATA FOR BROWN
AND ROSHKO He/N₂ EXPERIMENTAL RUN (FIGURE 16)

PT.	y	u	T	k	α He	α N ₂
1	9.998470	32.810	300.00	0.0791	1.0	0.0
2	9.998623	32.536	300.00	0.2325	1.0	0.0
3	9.993776	32.136	300.00	0.6491	1.0	0.0
4	9.993929	31.610	300.00	1.3359	1.0	0.0
5	9.999082	30.980	300.00	2.0615	1.0	0.0
6	9.999235	30.255	300.00	2.8914	1.0	0.0
7	9.999388	29.449	300.00	3.5244	1.0	0.0
8	9.999541	28.541	300.00	3.9550	1.0	0.0
9	9.999694	27.462	300.00	4.5514	1.0	0.0
10	9.999847	25.840	300.00	5.0305	1.0	0.0
11	10.000000	0.000	300.00	6.8992	0.5	0.5
12	10.000150	4.6900	300.00	0.10279	0.0	1.0
13	10.000300	4.6508	300.00	0.09300	0.0	1.0
14	10.000450	4.5933	300.00	0.08081	0.0	1.0
15	10.000600	4.5186	300.00	0.07020	0.0	1.0
16	10.000750	4.4283	300.00	0.05908	0.0	1.0
17	10.000900	4.3247	300.00	0.04212	0.0	1.0
18	10.001050	4.2094	300.00	0.02730	0.0	1.0
19	10.001200	4.0800	300.00	0.01326	0.0	1.0
20	10.001350	3.9241	300.00	0.00475	0.0	1.0
21	10.001500	3.6915	300.00	0.00162	0.0	1.0

UNITS: y - in.; U - ft/sec; k - ft²/sec²; T - °K.

TABLE 4. INITIAL PROFILE FOR BROWN AND ROSHKO He/N₂ SHEAR LAYER (FIGURE 16) — BOUNDARY LAYER INITIALIZATION

$$\lambda = -1.0$$

T R I P

6. 8/11

REFERENCES

• **REVERSE (A[1])**
• **END OF STATE + 01**

T R A N

11

68

४८८

FFNLT

1141.

۲۶۱

• 110

ט' ל

SPRUE
- 166858 -

107419

He/N₂
LAYER

SEARCH PLEX DATA - [SEARCH](#) [CREATE](#) [EDIT](#) [DELETE](#) [REFRESH](#)

WJWDKBC
29 JAN 74

TABLE 5. INITIAL PROFILE FOR BROWN AND ROSHKO He/N₂
SHEAR LAYER (FIGURE 16) — SPECIFIED PROFILE
INITIALIZATION

AE = 0.

VEL

INITIAL AND SUBSEQUENT HEAT FLUX DATA-FILE NAME + THE PROFILE

X/R
0.

VEL(X) + FFL

PRESS(A74)

PT	Y/R	VEL(X)Y	TEMPERATURE	LENSITY	MACH NO.	ENTH-TKE	FLNCT
		VEL(Y)T		GM/CC		10^6-(r/s)^0.2	LBS/FT^2
1	0.444848E+00	0.361100E+00	0.310000E+00	0.113601E-02	0.701091E-02	0.741000E-01	0.
2	0.444853E+00	0.361133E+00	0.300000E+00	0.113601E-02	0.701091E-02	0.153612E+00	1536
3	0.444854E+00	0.361135E+00	0.300000E+00	0.113601E-02	0.701091E-02	0.157330E+00	2100
4	0.444864E+00	0.361164E+00	0.300000E+00	0.113601E-02	0.701091E-02	0.257040E+00	2600
5	0.444870E+00	0.361175E+00	0.300000E+00	0.113601E-02	0.701091E-02	0.405544E+00	3300
6	0.444875E+00	0.361178E+00	0.300000E+00	0.113601E-02	0.701091E-02	0.554041E+00	4270
7	0.444880E+00	0.361180E+00	0.300000E+00	0.113601E-02	0.701091E-02	0.7048475E+00	4940
8	0.444880E+00	0.361178E+00	0.300000E+00	0.113601E-02	0.701091E-02	0.8684840E+00	6110
9	0.444882E+00	0.361171E+00	0.300000E+00	0.113601E-02	0.701091E-02	0.913521E+00	7230
10	0.444891E+00	0.361167E+00	0.300000E+00	0.113601E-02	0.701091E-02	0.144474E+01	7980
11	0.444905E+00	0.361160E+00	0.300000E+00	0.113601E-02	0.701091E-02	0.176204E+01	9130
12	0.444908E+00	0.361160E+00	0.300000E+00	0.113601E-02	0.701091E-02	0.204820E+01	9840
13	0.444914E+00	0.361167E+00	0.300000E+00	0.113601E-02	0.701091E-02	0.235625E+01	1050
14	0.444920E+00	0.361170E+00	0.300000E+00	0.113601E-02	0.701091E-02	0.264867E+01	1170
15	0.444926E+00	0.361175E+00	0.300000E+00	0.113601E-02	0.701091E-02	0.294522E+01	1230
16	0.444932E+00	0.361174E+00	0.300000E+00	0.113601E-02	0.701091E-02	0.319053E+01	1290
17	0.444937E+00	0.361173E+00	0.300000E+00	0.113601E-02	0.701091E-02	0.343473E+01	1330
18	0.444943E+00	0.361172E+00	0.300000E+00	0.113601E-02	0.701091E-02	0.363277E+01	1320
19	0.444950E+00	0.361170E+00	0.300000E+00	0.113601E-02	0.701091E-02	0.380334E+01	1390
20	0.444956E+00	0.361168E+00	0.300000E+00	0.113601E-02	0.701091E-02	0.398305E+01	1420
21	0.444962E+00	0.361165E+00	0.300000E+00	0.113601E-02	0.701091E-02	0.422493E+01	1470
22	0.444968E+00	0.361162E+00	0.300000E+00	0.113601E-02	0.701091E-02	0.447452E+01	1510
23	0.444975E+00	0.361160E+00	0.300000E+00	0.113601E-02	0.701091E-02	0.466338E+01	1580
24	0.444981E+00	0.361158E+00	0.300000E+00	0.113601E-02	0.701091E-02	0.490118E+01	1640
25	0.444987E+00	0.361155E+00	0.300000E+00	0.113601E-02	0.701091E-02	0.515700E+01	1700
26	0.444994E+00	0.361152E+00	0.300000E+00	0.113601E-02	0.701091E-02	0.532102E+01	1760
27	0.445001E+00	0.361149E+00	0.300000E+00	0.113601E-02	0.701091E-02	0.550054E+01	1820
28	0.445008E+00	0.361146E+00	0.300000E+00	0.113601E-02	0.701091E-02	0.567452E+01	1880
29	0.445015E+00	0.361143E+00	0.300000E+00	0.113601E-02	0.701091E-02	0.584740E+01	1940
30	0.445022E+00	0.361140E+00	0.300000E+00	0.113601E-02	0.701091E-02	0.602027E+01	2000
31	0.445030E+00	0.361137E+00	0.300000E+00	0.113601E-02	0.701091E-02	0.619318E+01	2060
32	0.445038E+00	0.361134E+00	0.300000E+00	0.113601E-02	0.701091E-02	0.636410E+01	2120
33	0.445046E+00	0.361131E+00	0.300000E+00	0.113601E-02	0.701091E-02	0.653132E+01	2180
34	0.445053E+00	0.361128E+00	0.300000E+00	0.113601E-02	0.701091E-02	0.669735E+01	2240
35	0.445060E+00	0.361125E+00	0.300000E+00	0.113601E-02	0.701091E-02	0.686273E+01	2300
36	0.445067E+00	0.361122E+00	0.300000E+00	0.113601E-02	0.701091E-02	0.70142413E+01	2360
37	0.445074E+00	0.361119E+00	0.300000E+00	0.113601E-02	0.701091E-02	0.717807E+01	2420
38	0.445081E+00	0.361116E+00	0.300000E+00	0.113601E-02	0.701091E-02	0.734313E+01	2480
39	0.445088E+00	0.361113E+00	0.300000E+00	0.113601E-02	0.701091E-02	0.750793E+01	2540
40	0.445095E+00	0.361110E+00	0.300000E+00	0.113601E-02	0.701091E-02	0.767170E+01	2600
41	0.445102E+00	0.361107E+00	0.300000E+00	0.113601E-02	0.701091E-02	0.783450E+01	2660
42	0.445109E+00	0.361104E+00	0.300000E+00	0.113601E-02	0.701091E-02	0.800034E+01	2720
43	0.445116E+00	0.361101E+00	0.300000E+00	0.113601E-02	0.701091E-02	0.816594E+01	2780
44	0.445123E+00	0.361098E+00	0.300000E+00	0.113601E-02	0.701091E-02	0.832870E+01	2840
45	0.445130E+00	0.361095E+00	0.300000E+00	0.113601E-02	0.701091E-02	0.849146E+01	2900
46	0.445137E+00	0.361092E+00	0.300000E+00	0.113601E-02	0.701091E-02	0.865264E+01	2960
47	0.445144E+00	0.361089E+00	0.300000E+00	0.113601E-02	0.701091E-02	0.881344E+01	3020
48	0.445151E+00	0.361086E+00	0.300000E+00	0.113601E-02	0.701091E-02	0.897270E+01	3080
49	0.445158E+00	0.361083E+00	0.300000E+00	0.113601E-02	0.701091E-02	0.913463E+01	3140
50	0.445165E+00	0.361080E+00	0.300000E+00	0.113601E-02	0.701091E-02	0.102000E-02	0.

110 210 310 410 510 610 710 810 910 1010 1110 1210 1310 1410 1510 1610 1710 1810 1910 2010 2110 2210 2310 2410 2510 2610 2710 2810 2910 3010 3110 3210 3310 3410 3510 3610 3710 3810 3910 4010 4110 4210 4310 4410 4510 4610 4710 4810 4910 5010 5110 5210 5310 5410 5510 5610 5710 5810 5910 6010 6110 6210 6310 6410 6510 6610 6710 6810 6910 7010 7110 7210 7310 7410 7510 7610 7710 7810 7910 8010 8110 8210 8310 8410 8510 8610 8710 8810 8910 9010 9110 9210 9310 9410 9510 9610 9710 9810 9910 10010 10110 10210 10310 10410 10510 10610 10710 10810 10910 11010 11110 11210 11310 11410 11510 11610 11710 11810 11910 12010 12110 12210 12310 12410 12510 12610 12710 12810 12910 13010 13110 13210 13310 13410 13510 13610 13710 13810 13910 14010 14110 14210 14310 14410 14510 14610 14710 14810 14910 15010 15110 15210 15310 15410 15510 15610 15710 15810 15910 16010 16110 16210 16310 16410 16510 16610 16710 16810 16910 17010 17110 17210 17310 17410 17510 17610 17710 17810 17910 18010 18110 18210 18310 18410 18510 18610 18710 18810 18910 19010 19110 19210 19310 19410 19510 19610 19710 19810 19910 20010 20110 20210 20310 20410 20510 20610 20710 20810 20910 21010 21110 21210 21310 21410 21510 21610 21710 21810 21910 22010 22110 22210 22310 22410 22510 22610 22710 22810 22910 22000 22100 22200 22300 22400 22500 22600 22700 22800 22900 23000 23100 23200 23300 23400 23500 23600 23700 23800 23900 24000 24100 24200 24300 24400 24500 24600 24700 24800 24900 25000 25100 25200 25300 25400 25500 25600 25700 25800 25900 25000 25100 25200 25300 25400 25500 25600 25700 25800 25900 26000 26100 26200 26300 26400 26500 26600 26700 26800 26900 27000 27100 27200 27300 27400 27500 27600 27700 27800 27900 28000 28100 28200 28300 28400 28500 28600 28700 28800 28900 29000 29100 29200 29300 29400 29500 29600 29700 29800 29900 29000 29100 29200 29300 29400 29500 29600 29700 29800 29900 30000 30100 30200 30300 30400 30500 30600 30700 30800 30900 31000 31100 31200 31300 31400 31500 31600 31700 31800 31900 32000 32100 32200 32300 32400 32500 32600 32700 32800 32900 33000 33100 33200 33300 33400 33500 33600 33700 33800 33900 34000 34100 34200 34300 34400 34500 34600 34700 34800 34900 35000 35100 35200 35300 35400 35500 35600 35700 35800 35900 36000 36100 36200 36300 36400 36500 36600 36700 36800 36900 37000 37100 37200 37300 37400 37500 37600 37700 37800 37900 38000 38100 38200 38300 38400 38500 38600 38700 38800 38900 39000 39100 39200 39300 39400 39500 39600 39700 39800 39900 39000 39100 39200 39300 39400 39500 39600 39700 39800 39900 40000 40100 40200 40300 40400 40500 40600 40700 40800 40900 41000 41100 41200 41300 41400 41500 41600 41700 41800 41900 42000 42100 42200 42300 42400 42500 42600 42700 42800 42900 43000 43100 43200 43300 43400 43500 43600 43700 43800 43900 44000 44100 44200 44300 44400 44500 44600 44700 44800 44900 45000 45100 45200 45300 45400 45500 45600 45700 45800 45900 46000 46100 46200 46300 46400 46500 46600 46700 46800 46900 47000 47100 47200 47300 47400 47500 47600 47700 47800 47900 48000 48100 48200 48300 48400 48500 48600 48700 48800 48900 49000 49100 49200 49300 49400 49500 49600 49700 49800 49900 49000 49100 49200 49300 49400 49500 49600 49700 49800 49900 50000 50100 50200 50300 50400 50500 50600 50700 50800 50900 51000 51100 51200 51300 51400 51500 51600 51700 51800 51900 52000 52100 52200 52300 52400 52500 52600 52700 52800 52900 53000 53100 53200 53300 53400 53500 53600 53700 53800 53900 54000 54100 54200 54300 54400 54500 54600 54700 54800 54900 55000 55100 55200 55300 55400 55500 55600 55700 55800 55900 56000 56100 56200 56300 56400 56500 56600 56700 56800 56900 57000 57100 57200 57300 57400 57500 57600 57700 57800 57900 58000 58100 58200 58300 58400 58500 58600 58700 58800 58900 59000 59100 59200 59300 59400 59500 59600 59700 59800 59900 59000 59100 59200 59300 59400 59500 59600 59700 59800 59900 60000 60100 60200 60300 60400 60500 60600 60700 60800 60900 61000 61100 61200 61300 61400 61500 61600 61700 61800 61900 62000 62100 62200 62300 62400 62500 62600 62700 62800 62900 63000 63100 63200 63300 63400 63500 63600 63700 63800 63900 64000 64100 64200 64300 64400 64500 64600 64700 64800 64900 65000 65100 65200 65300 65400 65500 65600 65700 65800 65900 66000 66100 66200 66300 66400 66500 66600 66700 66800 66900 67000 67100 67200 67300 67400 67500 67600 67700 67800 67900 68000 68100 68200 68300 68400 68500 68600 68700 68800 68900 69000 6

E+01	OPNLT L/V-17/17/002	PFNLT L/V-17/17/002	VISCOSITY LB/FT/SEC	PSI	PR-XE	UNORM
347/E-0C	0.791000E-01	0.	0.269169E+01	0.716588E+02	1.000	.997
350/E-0C	0.159315E+00	0.158402E-05	0.269170E+01	0.104416E+03	.993	
3615/E-0C	0.187330E+00	0.214608E-05	0.269172E+01	0.175460E+03	.989	
3646/E-0C	0.257640E+00	0.260865E-05	0.269173E+01	0.318407E+03	.984	
3653/E-0C	0.405554E+00	0.330383E-05	0.269175E+01	0.459115E+03	.979	
3667/E-0C	0.254041E+00	0.427647E-05	0.269176E+01	0.704808E+03	.974	
3684/E-0C	0.158475E+00	0.494686E-05	0.269177E+01	0.101794E+04	.967	
3695/E-0C	0.968840E+00	0.611921E-05	0.269179E+01	0.134930E+04	.960	
3701/E-0C	0.123552E+01	0.723557E-05	0.269180E+01	0.178911E+04	.952	
3737/E-0C	0.144474E+01	0.798610E-05	0.269182E+01	0.217281E+04	.944	
3743/E-0C	0.116204E+01	0.913964E-05	0.269183E+01	0.267620E+04	.936	
3746/E-0C	0.226420E+01	0.984187E-05	0.269185E+01	0.330430E+04	.926	
3748/E-0C	0.253625E+01	0.105653E-04	0.269186E+01	0.380536E+04	.917	
3751/E-0C	0.214807E+01	0.117914E-04	0.269188E+01	0.448281E+04	.907	
3789/E-0C	0.244572E+01	0.123827E-04	0.269189E+01	0.504574E+04	.896	
3790/E-0C	0.319033E+01	0.129023E-04	0.269190E+01	0.564772E+04	.885	
3791/E-0C	0.343473E+01	0.133604E-04	0.269192E+01	0.635326E+04	.872	
3792/E-0C	0.363277E+01	0.132862E-04	0.269193E+01	0.683216E+04	.860	
3793/E-0C	0.300394E+01	0.135467E-04	0.269195E+01	0.786849E+04	.846	
3794/E-0C	0.348363E+01	0.129047E-04	0.269196E+01	0.896174E+04	.831	
3795/E-0C	0.422743E+01	0.127600E-04	0.269198E+01	0.111920E+05	.815	
3797/E-0C	0.447483E+01	0.114437E-04	0.269199E+01	0.142480E+05	.793	
3799/E-0C	0.465398E+01	0.989120E-05	0.269201E+01	0.107397E+06	.768	
3801/E-0C	0.490118E+01	0.143064E-05	0.269202E+01	0.418880E+06	.444	
3804/E-0C	0.565708E+01	0.979803E-06	0.269204E+01	0.286113E+05	-.131	
3805/E-0C	0.532162E+01	0.297123E-04	0.269205E+01	0.633017E+03	-.035	
3807/E-0C	0.162113E+00	0.736953E-06	0.269206E+01	0.455215E+02	-.031	
3809/E-0C	0.571715E+01	0.939898E-05	0.269208E+01	0.374695E+02	-.028	
3810/E-0C	0.934703E+01	0.104319E-04	0.269209E+01	0.282878E+02	-.025	
3811/E-0C	0.564378E+01	0.123701E-04	0.269211E+01	0.249458E+02	-.023	
3812/E-0C	0.833164E+01	0.124503E-04	0.269212E+01	0.213828E+02	-.021	
3813/E-0C	0.766150E+01	0.129315E-04	0.269214E+01	0.192424E+02	-.019	
3814/E-0C	0.743135E+01	0.126840E-04	0.269215E+01	0.171166E+02	-.017	
3815/E-0C	0.100073E+01	0.128104E-04	0.269217E+01	0.150972E+02	-.015	
3816/E-0C	0.656273E+01	0.127635E-04	0.269218E+01	0.137941E+02	-.014	
3817/E-0C	0.612473E+01	0.121668E-04	0.269219E+01	0.118775E+02	-.012	
3818/E-0C	0.557787E+01	0.117241E-04	0.269221E+01	0.102284E+02	-.011	
3819/E-0C	0.442765E+01	0.106206E-04	0.269222E+01	0.836297E+01	-.009	
3820/E-0C	0.426263E+01	0.978313E-05	0.269224E+01	0.673564E+01	-.008	
3821/E-0C	0.371102E+01	0.914340E-05	0.269225E+01	0.559048E+01	-.007	
3822/E-0C	0.315340E+01	0.795728E-05	0.269227E+01	0.420672E+01	-.006	
3823/E-0C	0.260590E+01	0.722214E-05	0.269228E+01	0.311720E+01	-.005	
3824/E-0C	0.260870E+01	0.629714E-05	0.269230E+01	0.220768E+01	-.004	
3825/E-0C	0.157002E+01	0.499537E-05	0.269231E+01	0.143130E+01	-.003	
3826/E-0C	0.116234E+01	0.422310E-05	0.269232E+01	0.981500E+00	-.002	
3827/E-0C	0.853752E+01	0.331584E-05	0.269234E+01	0.548633E+00	-.002	
3828/E-0C	0.543444E+01	0.240837E-05	0.269235E+01	0.319222E+00	-.001	
3829/E-0C	0.327270E+01	0.210205E-05	0.269237E+01	0.215567E+00	0.000	
3830/E-0C	0.274630E+02	0.156543E-05	0.269238E+01	0.000		
3831/E-0C	0.162000E+02	0.162000E+01	0.269240E+01	0.000		

5PFD
V3E+00 -0.0335502E-04 -0.156685E-03 0.376045E-01 -0.174668E+06 26

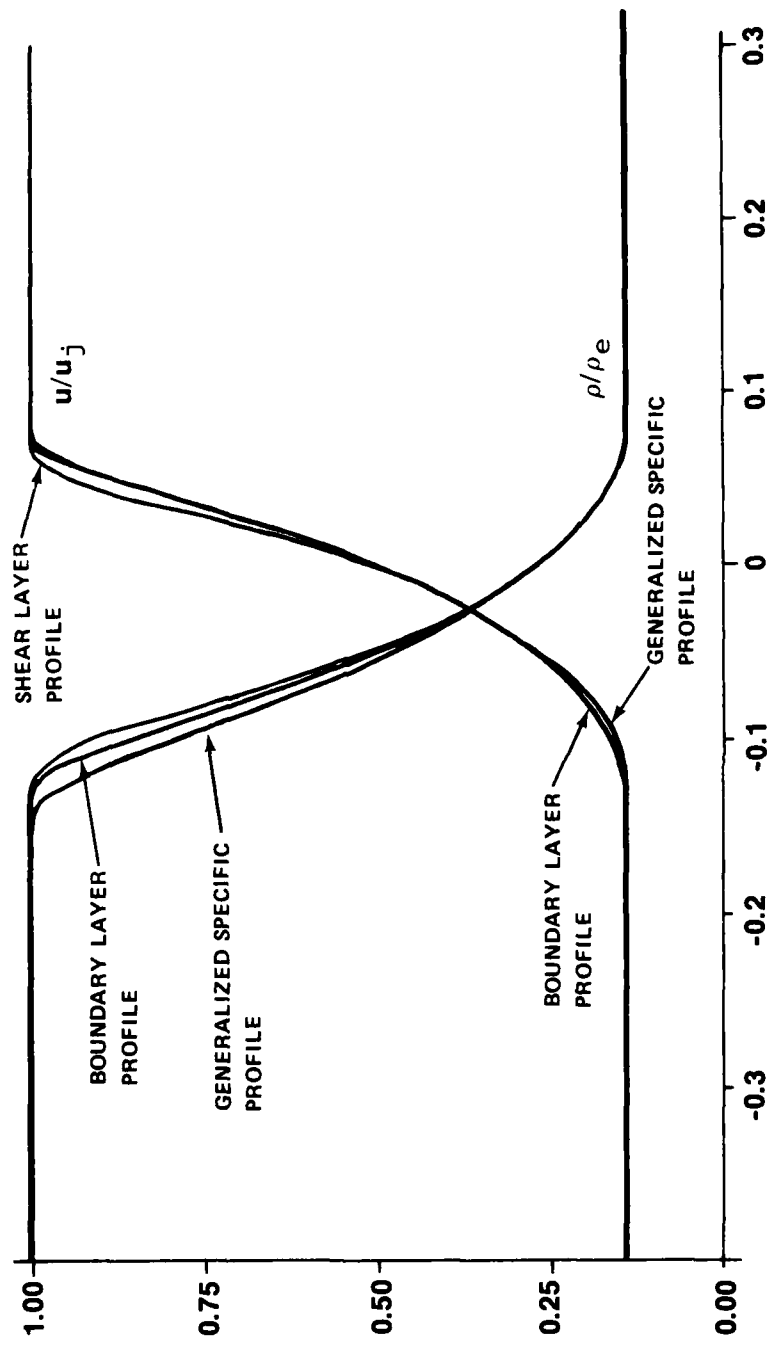


Figure 8. Comparison of results utilizing the three (3) input methods for determining the initial profile.

- Launder-Spalding $k\epsilon 2$ turbulence kinetic energy model
- Saffman $k\omega$ turbulence kinetic energy model.

The Saffman model was chosen because this model has been formulated to account for a specific physical phenomena which is not explicitly modeled in the other three. This model was formulated, primarily on empirical arguments, to account for shear flows which do not have a constant density. These density differences arise either due to differences in molecular weights of the shear layer fluids (heterogeneous fluids) or due to compressibility effects (Mach Number) in homogeneous fluids. Both of these effects are modeled in the turbulence equations formulation.

Compressibility effects are accounted for in the $k\epsilon 2$ turbulence model, but in an ad hoc manner. The turbulent viscosity contains an empirical correction term $k(M_{\infty})$ which was formulated using only a very limited set of experimental data. There are no additional terms in the model that account for this effect.

In order to use the Saffman model to make comparisons with data it was necessary to extend this model to a cylindrical geometry and to formulate it using a finite differencing scheme common to the other three models investigated. Only in this way can differences in results be solely due to the turbulence modeling and not due to the numerics. In addition, the equations are formulated in a stream function coordinate system.

Consider the Saffman formulation

$$\bar{\rho}U \frac{\partial e}{\partial x} + \bar{\rho}V \frac{\partial e}{\partial y} = \alpha'' \bar{\rho}e \left| \frac{\partial U}{\partial y} \right| - \bar{\rho}e\omega + \frac{1}{2} A \frac{\partial}{\partial y} \left(\frac{\bar{\rho}e}{\omega} \frac{\partial e}{\partial y} \right) \quad k\text{-EQUATION}$$

$$\begin{aligned} \bar{\rho}U \frac{\partial(\omega^2)}{\partial x} + \bar{\rho}V \frac{\partial \omega^2}{\partial y} &= \alpha' \bar{\rho}\omega^2 \left| \frac{\partial U}{\partial y} \right| - \beta' \bar{\rho}\omega^3 \\ &+ \frac{1}{2} A \frac{\partial}{\partial y} \left(\frac{\bar{\rho}e}{\omega} \frac{\partial(\omega^2)}{\partial y} \right) \quad \text{VORTICITY EQUATION} \\ &- AY \frac{\omega}{\bar{\rho}} \frac{\gamma_1}{\partial y} \frac{\partial}{\partial y} \left(\bar{\rho}e \right) \end{aligned}$$

where

$$A = 0.09 \quad \alpha'' = A^{\frac{1}{2}} \quad \beta' = 5/3 \quad \alpha' = \beta' \alpha'' - 2k^2$$

These equations can be generalized for either 2-D or axisymmetric flow to be

$$\begin{aligned} \frac{De}{Dt} &= \frac{A}{2} \frac{1}{y^j} \frac{\partial}{\partial y} \left(y^j \frac{\rho e}{\omega} \frac{\partial e}{\partial y} \right) + \alpha'' \rho e \left| \left(\frac{\partial u}{\partial y} \right) \right| - \rho e \omega \\ \frac{D\omega}{Dt}^2 &= \frac{A}{2} \frac{1}{y^j} \frac{\partial}{\partial y} \left(y^j \frac{\rho e}{\omega} \frac{\partial \omega^2}{\partial y} \right) + \alpha' \rho \omega^2 \left| \frac{\partial u}{\partial y} \right| - \beta' \rho \omega^3 \\ &- A \gamma \frac{\omega}{\rho} \frac{\partial \rho}{\partial y} \frac{\partial}{\partial y} \left(\rho e \right) \end{aligned}$$

In order to apply these equations to an axisymmetric rocket exhaust plume, choose $j = 1$; $y = r$. Utilizing different notations for the turbulence kinetic energy ($k^2 = \frac{u^2 + v^2}{2}$), these equations become

$$\begin{aligned} \rho \frac{Dk}{Dt} &= \frac{1}{2} \frac{1}{r} \frac{\partial}{\partial r} \left(r u_t \frac{\partial k}{\partial r} \right) + \frac{\alpha''}{A} \omega u_t \left| \frac{\partial u}{\partial r} \right| - \rho k \omega \\ \rho \frac{D\omega}{Dt}^2 &= \frac{1}{2} \frac{1}{r} \frac{\partial}{\partial r} \left(r u_t \frac{\partial \omega^2}{\partial r} \right) + \alpha' \rho \omega^2 \left| \frac{\partial u}{\partial r} \right| - \frac{A \gamma \omega}{\rho} \frac{\partial \rho}{\partial r} \frac{\partial}{\partial r} \rho k \\ &- \beta' \omega^3 \end{aligned}$$

where $e = k$ & $u_t = \frac{A \rho e}{\omega}$

so rewriting these equations.

$$\begin{aligned} \rho \frac{Dk}{Dt} &= \frac{1}{2r} \frac{\partial}{\partial r} \left(r u_t \frac{\partial k}{\partial r} \right) + C_1 \omega u_t \left| \frac{\partial u}{\partial r} \right| - \rho k \omega \\ \rho \frac{D\omega}{Dt}^2 &= \frac{1}{2r} \frac{\partial}{\partial r} \left(r u_t \frac{\partial \omega^2}{\partial r} \right) + C_2 \omega^2 \left| \frac{\partial u}{\partial r} \right| + \frac{C_3 \omega}{r} \left(\frac{\partial r}{\partial r} \right) \frac{\partial}{\partial r} \left(\rho k \right) \\ &+ C_4 \omega^3 \end{aligned}$$

where:

$$C_1 = \frac{\alpha''}{A} \quad C_2 = \alpha' \quad C_3 = -A\gamma \quad C_4 = -\beta' \quad \gamma = 1$$

$$C_1 = \frac{A^{\frac{1}{2}}}{A} \quad C_2 = \beta' \alpha'' - 2k^2 \quad C_3 = - (0.09)^{\frac{1}{2}}(1) \quad C_4 = - 5/3$$

$$C_1 = A^{-\frac{1}{2}} \quad C_2 = \frac{5}{3}(0.9)^{\frac{1}{2}} - 2(.41)^2$$

$$C_1 = (.09)^{-\frac{1}{2}} \quad C_2 = 0.1638 \quad C_3 = -0.3 \quad C_4 = -1.6667$$

$$C_1 = 3.33333 \quad C_2 = 0.1638 \quad C_3 = -0.3 \quad C_4 = 1.66667$$

Now define

$$z = \omega^2$$

$$\rho \frac{Dk}{Dt} = \frac{1}{2r} \frac{\partial}{\partial r} \left(r \mu_t \frac{\partial k}{\partial r} \right) + C_1 z^{\frac{1}{2}} \mu_t \left| \frac{\partial u}{\partial r} \right| - \rho k z^{\frac{1}{2}} \quad (37)$$

$$\rho \frac{Dz}{Dt} = \frac{1}{2r} \frac{\partial}{\partial r} \left(r \mu_t \frac{\partial z}{\partial r} \right) + C_2 \rho z \left| \frac{\partial u}{\partial r} \right| + \frac{C_3 z^{\frac{1}{2}}}{\rho} \left(\frac{\partial \rho}{\partial r} \right) \frac{\partial}{\partial r} (\rho k) \\ + C_4 \rho z^{\frac{3}{2}} \quad (38)$$

where $\mu_t = \frac{C_5 \rho k}{z^{\frac{1}{2}}}$

and

$$C_5 = 0.09$$

Expanding (1) for a steady flow gives —

$$\rho u \frac{\partial k}{\partial x} + \rho v \frac{\partial k}{\partial r} = \frac{1}{2r} \frac{\partial}{\partial r} \left(r \mu_t \frac{\partial k}{\partial r} \right) + C_1 z^{\frac{1}{2}} \mu_t \left| \frac{\partial u}{\partial r} \right| - \rho k z^{\frac{1}{2}} \quad (39)$$

This equation can be transformed from $(x, r) \rightarrow (x, \psi)$ utilizing a transformation of dependent variables.

$$\psi \frac{\partial \psi}{\partial r} = \rho u r \quad (40)$$

$$\psi \frac{\partial \psi}{\partial x} = \rho v r \quad (41)$$

$$\left(\frac{\partial}{\partial r} \right)_x = \frac{\rho u r}{\psi} \left(\frac{\partial}{\partial \psi} \right)_x \quad (42)$$

$$\left(\frac{\partial}{\partial x} \right)_r = \left(\frac{\partial}{\partial x} \right)_\psi - \frac{\rho v r}{\psi} \left(\frac{\partial}{\partial \psi} \right)_x \quad (43)$$

utilizing (42) and (43) in (39)

$$\begin{aligned} \rho u \left\{ \frac{\partial k}{\partial x} - \cancel{\frac{\rho v r}{\psi} \frac{\partial k}{\partial \psi}} \right\} + \rho v \left\{ \cancel{\frac{\rho u r}{\psi} \frac{\partial k}{\partial \psi}} \right\} &= \frac{1}{2r} \frac{\rho u r}{\psi} \frac{\partial}{\partial \psi} \left\{ r \mu_t \left[\frac{\rho u r}{\psi} \frac{\partial k}{\partial \psi} \right] \right\} \\ &+ C_1 z^{\frac{1}{2}} \mu_t \left| \frac{\rho u r}{\psi} \frac{\partial u}{\partial \psi} \right| - \rho k z^{\frac{1}{2}} \end{aligned}$$

$$\begin{aligned} \rho u \frac{\partial k}{\partial x} &= \frac{\rho u}{2\psi} \frac{\partial}{\partial \psi} \left\{ \frac{\rho u r^2}{\psi} \mu_t \frac{\partial k}{\partial \psi} \right\} + C_1 \mu_t z^{\frac{1}{2}} \left| \frac{\rho u r}{\psi} \frac{\partial u}{\partial \psi} \right| - \rho k z^{\frac{1}{2}} \\ \frac{\partial k}{\partial x} &= \frac{1}{2\psi} \frac{\partial}{\partial \psi} \left\{ \frac{\rho u r^2}{\psi} \mu_t \frac{\partial k}{\partial \psi} \right\} + C_1 \mu_t z^{\frac{1}{2}} \left| \frac{r}{\psi} \frac{\partial u}{\partial \psi} \right| - \frac{k z^{\frac{1}{2}}}{u} \quad (44) \end{aligned}$$

Expanding (38) for steady flow gives —

$$\begin{aligned} \rho u \frac{\partial z}{\partial x} + \rho v \frac{\partial z}{\partial r} &= \frac{1}{2r} \frac{\partial}{\partial r} \left(r \mu_t \frac{\partial z}{\partial r} \right) \quad (45) \\ &+ C_2 \rho z \left| \frac{\partial u}{\partial r} \right| + \frac{C_3 z^{\frac{1}{2}}}{\rho} \left(\frac{\partial \rho}{\partial r} \right) \frac{\partial}{\partial r} (\rho k) + C_4 \rho z^{\frac{3}{2}} \end{aligned}$$

utilizing (42) and (43) in (45) gives ---

$$\rho u \left\{ \frac{\partial z}{\partial x} - \frac{\rho v r}{\psi} \frac{\partial z}{\partial \psi} \right\} + \rho v \left\{ \frac{\rho u r}{\psi} \frac{\partial z}{\partial \psi} \right\} = \frac{1}{2r} \frac{\rho u r}{\psi} \frac{\partial}{\partial \psi} \left\{ r \mu_t \left[\frac{\rho u r}{\psi} \frac{\partial z}{\partial \psi} \right] \right\} \\ + C_2 \rho z \left| \frac{\rho u r}{\psi} \frac{\partial u}{\partial \psi} \right| + \frac{C_3 z^{\frac{1}{2}}}{\rho} \frac{\rho u r}{\psi} \frac{\partial \rho}{\partial \psi} \frac{\rho u r}{\psi} \frac{\partial}{\partial \psi} (\rho k) + C_4 \rho z^{\frac{3}{2}}$$

$$\rho u \frac{\partial z}{\partial x} = \frac{\rho u}{2\psi} \frac{\partial}{\partial \psi} \left\{ \frac{\rho u r^2}{\psi} \mu_t \frac{\partial z}{\partial \psi} \right\} + C_2 z \left| \frac{\rho^2 u r}{\psi} \frac{\partial u}{\partial \psi} \right| \\ + C_3 z^{\frac{1}{2}} \frac{\rho u^2 r^2}{\psi^2} \left(\frac{\partial \rho}{\partial \psi} \right) \frac{\partial}{\partial \psi} (\rho k) + C_4 \rho z^{\frac{3}{2}}$$

since ρ is always positive. Dividing by ρu gives

$$\frac{\partial z}{\partial x} = \frac{1}{2\psi} \frac{\partial}{\partial \psi} \left\{ \frac{\rho u r^2 \mu_t}{\psi} \frac{\partial z}{\partial \psi} \right\} + \frac{C_2 z}{u} \left| \frac{\rho u r}{\psi} \frac{\partial u}{\partial \psi} \right| \\ + C_3 z^{\frac{1}{2}} \frac{u r^2}{\psi^2} \left(\frac{\partial \rho}{\partial \psi} \right) \frac{\partial}{\partial \psi} (\rho k) + \frac{C_4 z^{\frac{3}{2}}}{u} \quad (46)$$

Hence, the turbulence model equations in the transformed plane are (44) and (46)

$$\frac{\partial k}{\partial x} = \frac{1}{2\psi} \frac{\partial}{\partial \psi} \left\{ \frac{\rho u r^2 \mu_t}{\psi} \frac{\partial k}{\partial \psi} \right\} + C_1 \mu_t z^{\frac{1}{2}} \left| \frac{r}{\psi} \frac{\partial u}{\partial \psi} \right| - \frac{k z^{\frac{1}{2}}}{u} \quad (44)$$

$$\frac{\partial z}{\partial x} = \frac{1}{2\psi} \frac{\partial}{\partial \psi} \left\{ \frac{\rho u r^2 \mu_t}{\psi} \frac{\partial z}{\partial \psi} \right\} + \frac{C_2 z}{u} \left| \frac{\rho u r}{\psi} \frac{\partial u}{\partial \psi} \right| \\ + C_3 z^{\frac{1}{2}} \frac{u r^2}{\psi^2} \left(\frac{\partial \rho}{\partial \psi} \right) \frac{\partial}{\partial \psi} (\rho k) + \frac{C_4 z^{\frac{3}{2}}}{u} \quad (46)$$

where:

$$\mu_t = \frac{C_5 \rho k}{z^2}$$

$$z = \omega^2$$

$$C_5 = 0.09$$

and the other constants are as they appear on page 34. To account for the effects of compressibility, Saffman introduces an additional term into the k -equation. This is the last term in his equation given below

$$\bar{\rho}U \frac{\partial e}{\partial x} + \bar{\rho}V \frac{\partial e}{\partial y} = \alpha'' \bar{\rho}e \left| \frac{\partial U}{\partial y} \right| + \frac{1}{2} A \frac{\partial}{\partial y} \left(\frac{\bar{\rho}e}{\omega} \frac{\partial e}{\partial y} \right) - \bar{\rho}e \omega - A \xi \frac{\gamma - 1}{2} \frac{\bar{\rho}^2 e^2}{\omega} \left(\frac{\partial U}{\partial y} \right)^2$$

where the subscript "1" in the last term refers to properties of the external stream. Rewriting this equation

$$\bar{\rho}U \frac{\partial e}{\partial x} + \bar{\rho}V \frac{\partial e}{\partial y} = \alpha'' \bar{\rho}e \left| \frac{\partial U}{\partial y} \right| + \frac{1}{2} \frac{\partial}{\partial y} \left(\frac{A \bar{\rho}e}{\omega} \frac{\partial e}{\partial y} \right) - \xi \frac{(\gamma - 1)}{2} \frac{\bar{\rho}e}{\rho_1 a_1} \left\{ \frac{A \bar{\rho}e}{\omega} \right\} \left(\frac{\partial U}{\partial y} \right)^2 - \bar{\rho}e \omega \quad (47)$$

The turbulent eddy viscosity has been given previously by

$$\mu_t = A \frac{\bar{\rho}e}{\omega}$$

Substituting this into the previous equation gives

$$\bar{\rho}U \frac{\partial e}{\partial k} + \bar{\rho}V \frac{\partial e}{\partial y} = \alpha'' \bar{\rho}e \left| \frac{\partial U}{\partial y} \right| + \frac{1}{2} \frac{\partial}{\partial y} \left(\mu_t \frac{\partial e}{\partial y} \right) - \xi \left(\frac{\gamma - 1}{2} \right) \left(\bar{\rho}e \right) \mu_t \left(\frac{\partial U}{\partial y} \right)^2 - \bar{\rho}e \omega \quad (48)$$

Now if we utilize the notation that the turbulent kinetic energy is given by k , Equation (48) becomes

$$\begin{aligned} \bar{\rho}U \frac{\partial k}{\partial x} + \bar{\rho}V \frac{\partial k}{\partial y} &= \frac{1}{2} \frac{\partial}{\partial y} \left(\mu_t \frac{\partial k}{\partial y} \right) + \alpha'' \bar{\rho}k \left| \frac{\partial U}{\partial y} \right| \\ &- \bar{\rho}k\omega - \xi \left(\frac{\gamma - 1}{2} \right) \left(\bar{\rho}k \right) \mu_t \left(\frac{\partial U}{\partial y} \right)^2 \end{aligned} \quad (49)$$

where as before $k \equiv e$

writing this equation in terms of the substantial derivative

$$\begin{aligned} \bar{\rho} \frac{Dk}{Dt} &= \frac{1}{2} \frac{\partial}{\partial y} \left(\mu_t \frac{\partial k}{\partial y} \right) + \alpha'' \bar{\rho}k \left| \frac{\partial U}{\partial y} \right| \\ &- \bar{\rho}k\omega - \xi \left(\frac{\gamma - 1}{2} \right) \left(\bar{\rho}k\mu_t \right) \left(\frac{\partial U}{\partial y} \right)^2 \end{aligned} \quad (50)$$

Now for a perfect gas, the sonic velocity of the external stream, a_1 is given by

$$a_1^2 = \gamma RT_1 = \frac{\gamma p_1}{\rho_1}$$

Also for a perfect gas

$$C_p - C_v = R$$

and

$$1 - \frac{1}{\gamma} = \frac{R}{C_p}$$

$$\frac{\gamma - 1}{\gamma} = \frac{R}{C_p}$$

Utilizing these two relations

$$\begin{aligned}
 \frac{\gamma - 1}{\rho_1 a_1} &= \left(\frac{\gamma - 1}{\gamma} \right) \left(\frac{1}{a_1} \right) \left(\frac{\gamma}{\rho_1} \right) \\
 &= \frac{R_1}{C_{p_1}} - \frac{\rho_1}{\gamma p_1} - \frac{\gamma}{\rho_1} \\
 &= \frac{R_1}{C_{p_1} p_1} \\
 \frac{\gamma - 1}{\rho_1 a_1} &= \frac{\bar{R}}{M_w C_{p_1} p_1} \quad (51)
 \end{aligned}$$

Where the subscript 1 refers to the external stream. Utilizing this relation (51) in (50) above leads to

$$\begin{aligned}
 \bar{\rho} \frac{Dk}{Dt} &= \frac{1}{2} \frac{\partial}{\partial y} \left(u_t \frac{\partial k}{\partial y} \right) + \alpha'' \bar{\rho} k \left| \frac{\partial U}{\partial y} \right| - \bar{\rho} k \omega \\
 &\quad - \xi \left\{ \frac{\bar{R}}{M_w C_{p_{ex}} p_{ex}} \right\} \bar{\rho} k u_t \left(\frac{\partial U}{\partial y} \right)^2 \quad (52)
 \end{aligned}$$

Transforming this equation to cylindrical coordinates

$$\begin{aligned}
 \bar{\rho} \frac{Dk}{Dt} &= \frac{1}{2r} \frac{\partial}{\partial r} \left(r u_t \frac{\partial k}{\partial r} \right) + \alpha'' \bar{\rho} k \left| \frac{\partial U}{\partial r} \right| - \bar{\rho} k \omega \\
 &\quad - \xi \left\{ \frac{\bar{R}}{M_w C_{p_{ex}} p_{ex}} \right\} \bar{\rho} k u_t \left(\frac{\partial U}{\partial r} \right)^2 \quad (53)
 \end{aligned}$$

Now if we define

$$z \equiv \omega^2 \quad (54)$$

and drop the mean value notation (53) becomes --

$$\rho \frac{Dk}{Dt} = \frac{1}{2r} \frac{\partial}{\partial r} \left(r \mu_t \frac{\partial k}{\partial r} \right) + \alpha'' \rho k \left| \frac{\partial u}{\partial r} \right| - \rho k z^{\frac{1}{2}} \\ - \xi \left\{ \frac{\bar{R}}{MW_{ex} C_{pex} P_{ex}} \right\} \rho k \mu_t \left(\frac{\partial u}{\partial r} \right)^2 \quad (55)$$

where

$$\mu_t = \frac{A \rho k}{\omega} = \frac{A \rho k}{z^{\frac{1}{2}}} \quad (56)$$

Utilizing (56) the second term on the right hand side (RHS) of (55) becomes

$$\alpha'' \rho k \left| \frac{\partial u}{\partial r} \right| = \alpha'' \left| \frac{\partial u}{\partial r} \right| \frac{\mu_t z^{\frac{1}{2}}}{A} \quad (57)$$

$$\alpha'' \rho k \left| \frac{\partial u}{\partial r} \right| = \frac{\alpha''}{A} z^{\frac{1}{2}} \mu_t \left| \frac{\partial u}{\partial r} \right|$$

Substituting (57) back into (56)

$$\rho \frac{Dk}{Dt} = \frac{1}{2r} \frac{\partial}{\partial r} \left(r \mu_t \frac{\partial k}{\partial r} \right) + \frac{\alpha''}{A} z^{\frac{1}{2}} \mu_t \left| \frac{\partial u}{\partial r} \right| \quad (58)$$

$$- \rho k z^{\frac{1}{2}} - \xi \left\{ \frac{\bar{R}}{MW_{ex} C_{pex} P_{ex}} \right\} \rho k \mu_t \left(\frac{\partial u}{\partial r} \right)^2$$

Hence, if we let

$$C_1 \equiv \frac{\alpha''}{A} = \frac{A^{\frac{1}{2}}}{A} = A^{-\frac{1}{2}} = 0.09^{-\frac{1}{2}} = 3.33333$$

$$C_6 \equiv \xi = 2.5$$

Equation (58) becomes

$$\boxed{\begin{aligned} \rho \frac{Dk}{Dt} &= \frac{1}{2r} \frac{\partial}{\partial r} \left(r u_t \frac{\partial k}{\partial r} \right) + C_1 z^{\frac{1}{2}} u_t \left| \frac{\partial u}{\partial r} \right| \\ &\quad - \rho k z^{\frac{1}{2}} - \frac{C_6 \bar{R} \rho k u_t}{MW_{ex} C_{pex} P_{ex}} \left(\frac{\partial u}{\partial r} \right)^2 \end{aligned}} \quad (59)$$

Where (59) differs from (47) in the previous formulation only by the last term.

Expanding (59) for a steady flow gives

$$\begin{aligned} \rho u \frac{\partial k}{\partial x} + \rho v \frac{\partial k}{\partial r} &= \frac{1}{2r} \frac{\partial}{\partial r} \left(r u_t \frac{\partial k}{\partial r} \right) + C_1 z^{\frac{1}{2}} u_t \left| \frac{\partial u}{\partial r} \right| \\ &\quad - \rho k z^{\frac{1}{2}} - \frac{C_6 \bar{R} \rho k u_t}{MW_e C_{pe} P_e} \left(\frac{\partial u}{\partial r} \right)^2 \end{aligned} \quad (60)$$

Now (60) can be transformed from $(x, r) \rightarrow (x, \psi)$ using the transformation of dependent variable

$$\left(\frac{\partial}{\partial r} \right)_x = \frac{\rho u r}{\psi} \left(\frac{\partial}{\partial \psi} \right)_x \quad (61)$$

$$\left(\frac{\partial}{\partial x} \right)_r = \left(\frac{\partial}{\partial x} \right)_\psi - \frac{\rho v r}{\psi} \left(\frac{\partial}{\partial \psi} \right)_x \quad (62)$$

Utilizing (61) and (62) in (60)

$$\begin{aligned} \rho u &\left\{ \frac{\partial k}{\partial x} - \cancel{\frac{\rho v r}{\psi} \frac{\partial k}{\partial \psi}} \right\} + \rho v \left\{ \cancel{\frac{\rho u r}{\psi} \frac{\partial k}{\partial \psi}} \right\} \\ &= \frac{1}{2r} \frac{\rho u r}{\psi} \frac{\partial}{\partial \psi} \left(r u_t \frac{\rho u r}{\psi} \frac{\partial k}{\partial \psi} \right) + C_1 z^{\frac{1}{2}} u_t \left| \frac{\rho u r}{\psi} \frac{\partial u}{\partial \psi} \right| \\ &\quad - \rho k z^{\frac{1}{2}} - \frac{C_6 \bar{R} \rho k u_t}{MW_e C_{pe} P_e} \frac{\rho^2 u^2 r^2}{\psi^2} \left(\frac{\partial u}{\partial \psi} \right)^2 \end{aligned} \quad (63)$$

$$\begin{aligned}
 \rho u \frac{\partial k}{\partial x} &= \frac{\rho u}{2\psi} \frac{\partial}{\partial \psi} \left(\frac{\rho u r^2}{\psi} \mu_t \frac{\partial k}{\partial \psi} \right) + c_1 z^{\frac{1}{2}} \mu_t \left| \frac{\rho u r}{\psi} \left(\frac{\partial u}{\partial \psi} \right) \right| \\
 &- \rho k z^{\frac{1}{2}} - \frac{c_6 \bar{R} \rho^3 k \mu_t u^2 r^2}{M w_e C_{p_e} P_e \psi^2} \left(\frac{\partial u}{\partial \psi} \right)^2
 \end{aligned} \tag{64}$$

Since ρu always > 0 for the shear flows considered here

$$\begin{aligned}
 \frac{\partial k}{\partial x} &= \frac{1}{2\psi} \frac{\partial}{\partial \psi} \left(\frac{\rho u r^2}{\psi} \mu_t \frac{\partial k}{\partial \psi} \right) + c_1 z^{\frac{1}{2}} \mu_t \left| \frac{r}{\psi} \left(\frac{\partial u}{\partial \psi} \right) \right| \\
 &- \frac{k z^{\frac{1}{2}}}{u} - \frac{c_6 \bar{R} \rho^2 k \mu_t u r^2}{M w_e C_{p_e} P_e \psi^2} \left(\frac{\partial u}{\partial \psi} \right)^2
 \end{aligned} \tag{65}$$

Where it will be noted that (65) differs from (54) only in the addition of the last term

From Equations (65) and (56) —

$$\begin{aligned}
 \frac{\partial k}{\partial x} &= \frac{1}{2\psi} \frac{\partial}{\partial \psi} \left\{ \frac{\rho u r^2 \mu_t}{\psi} \frac{\partial k}{\partial \psi} \right\} + c_1 \mu_t z^{\frac{1}{2}} \left| \frac{r}{\psi} \frac{\partial u}{\partial \psi} \right| - k \frac{z^{\frac{1}{2}}}{u} \\
 &- \frac{c_6 \bar{R} \rho^2 k u r^2 \mu_t}{C_{p_2} M w_2 P_2 \psi^2} \left(\frac{\partial u}{\partial \psi} \right)^2
 \end{aligned} \tag{66}$$

$$\begin{aligned}
 \frac{\partial z}{\partial x} &= \frac{1}{2\psi} \frac{\partial}{\partial \psi} \left\{ \frac{\rho u r^2 \mu_t}{\psi} \frac{\partial z}{\partial \psi} \right\} + \frac{c_2 z}{u} \left| \frac{\rho u r}{\psi} \frac{\partial u}{\partial \psi} \right| + c_3 z^{\frac{1}{2}} \frac{u r^2}{\psi^2} \left(\frac{\partial \rho}{\partial \psi} \right) \\
 &\frac{\partial}{\partial \psi} (ok) + \frac{c_4 z^{\frac{3}{2}}}{u}
 \end{aligned} \tag{67}$$

where the subscripts "2" and "ex" are synonymous. Now let $A \equiv (\mu_t + \rho u r^2)/\psi$ and utilize the following finite difference formulation

$$\frac{\partial}{\partial \psi} \left(a \frac{\partial f}{\partial \psi} \right) = a_{n,m} + \frac{1}{2} \frac{(f_{n,m+1} - f_{n,m})}{(\Delta \psi)^2} - a_{n,m} - \frac{1}{2} \frac{(f_{n,m} - f_{n,m-1})}{(\Delta \psi)^2}$$

Where:

$$a_{n,m} + \frac{1}{2} = \frac{a_{n,m} + a_{n,m+1}}{2}$$

$$a_{n,m} - \frac{1}{2} = \frac{a_{n,m} + a_{n,m-1}}{2}$$

$$\left(\frac{\partial f}{\partial \psi} \right)_{n,m} = \frac{f_{n,m+1} - f_{n,m-1}}{2 \Delta \psi} \quad (68)$$

Utilizing these formulas in (66)

$$\Delta k_{n,m} =$$

$$\frac{\Delta x}{2 \psi_{n,m}} \left[\frac{A_{n,m} + \frac{1}{2} \{ k_{n,m+1} - k_{n,m} \} - A_{n,m-\frac{1}{2}} \{ k_{n,m} - k_{n,m-1} \}}{(\Delta \psi)^2} \right]$$

$$+ C_1 \mu_t z_{n,m}^{\frac{1}{2}} \Delta x \left| \frac{r}{\psi_{n,m}} \frac{u_{n,m+1} - u_{n,m-1}}{2 \Delta \psi} \right|$$

$$- \frac{k_{n,m} z_{n,m}^{\frac{1}{2}}}{u_{n,m}} \Delta x - \frac{C_6 \bar{R}_p^2 k_{n,m} u_{n,m} r^2 \mu_t}{C_p^2 M_w^2 p_2 \psi_{n,m}^2} \Delta x$$

$$\left\{ \frac{u_{n,m+1} - u_{n,m-1}}{2 \Delta \psi} \right\}^2$$

and

$$\begin{aligned}
 k_{n+1, m} &= k_{n, m} + \frac{\Delta x}{2\psi_{n, m}(\Delta\psi)^2} \\
 &\left\{ A_{n, m} + \frac{1}{2} \left[k_{n, m+1} - k_{n, m} \right] - A_{n, m} - \frac{1}{2} \left[k_{n, m} - k_{n, m-1} \right] \right\} \\
 &+ C_1 \mu_t \Delta x z_{n, m}^{\frac{1}{2}} \left| \frac{r}{2\psi_{n, m} \Delta\psi} \left\{ u_{n, m+1} - u_{n, m-1} \right\} \right| - \frac{k_{n, m} z_{n, m}^{\frac{1}{2}} \Delta x}{u_{n, m}} \\
 &- \frac{C_6 \bar{R}_p^2 k_{n, m} u_{n, m} r^2 \mu_t \Delta x}{4 C_p^2 M_w^2 p_2 \psi_{n, m}^2 (\Delta\psi)^2} \left\{ u_{n, m+1} - u_{n, m-1} \right\}^2
 \end{aligned} \tag{69}$$

Utilizing the same difference formulas for equation (67)

$$\begin{aligned}
 \Delta z_{n, m} &= \frac{\Delta x}{2\psi_{n, m} \Delta\psi} \left\{ A_{n, m} + \frac{1}{2} \left\{ z_{n, m+1} - z_{n, m} \right\} \right. \\
 &- A_{n, m} - \frac{1}{2} \left\{ z_{n, m} - z_{n-1, m} \right\} \\
 &+ \frac{C_2 z_{n, m} \Delta x}{u_{n, m}} \left| \frac{\rho u_{n, m} r}{\psi_{n, m}} \left(\frac{u_{n, m+1} - u_{n, m-1}}{2\Delta\psi} \right) \right| \\
 &+ \frac{C_3 z_{n, m}^{\frac{1}{2}} u_{n, m} r^2 \Delta x}{\psi_{n, m}^2} \left\{ \frac{\rho_{n, m+1} - \rho_{n, m-1}}{2\Delta\psi} \right\} \\
 &\left. \left[k_{n, m} \left\{ \frac{k_{n, m+1} - k_{n, m-1}}{2\Delta\psi} \right\} \right. \right. \\
 &+ k_{n, m} \left\{ \frac{\rho_{n, m+1} - \rho_{n, m-1}}{2\Delta\psi} \right\} \left. \right] + \frac{C_4 z_{n, m}^{\frac{3}{2}} \Delta x}{u_{n, m}}
 \end{aligned} \tag{70}$$

and

$$\begin{aligned}
 z_{n+1,m} = z_{n,m} + & \frac{\Delta x}{2\psi_{n,m}(\Delta\psi)^2} \left\{ A_{n,m} + \frac{1}{2} [z_{n,m+1} - z_{n,m}] \right. \\
 & - A_{n,m} - \frac{1}{2} [z_{n,m} - z_{n,m-1}] \left. \right\} + \frac{C_2 z_{n,m} \Delta x}{u_{n,m}} \left| \frac{\rho u_{n,m} r}{\psi_{n,m}} \right. \\
 & \left[\frac{u_{n,m+1} - u_{n,m-1}}{2(\Delta\psi)} \right] \left. \right\} + \frac{C_3 z_{n,m}^{1/2} u_{n,m} r^2 \Delta x}{4\psi_{n,m}^2 (\Delta\psi)^2} \left\{ \rho_{n,m+1} \right. \\
 & - \rho_{n,m} - 1 \left. \right\} \left[\rho_{n,m} \left\{ k_{n,m+1} - k_{n,m-1} \right\} \right. \\
 & + k_{n,m} \left\{ \rho_{n,m+1} - \rho_{n,m-1} \right\} \left. \right] + \frac{C_4 z_{n,m}^{3/2} \Delta x}{u_{n,m}} \quad (71)
 \end{aligned}$$

and finally

$$\begin{aligned}
 z_{n+1,m} = z_{n,m} + & \frac{\Delta x}{2\psi_{n,m}(\Delta\psi)^2} \left\{ A_{n,m} + \frac{1}{2} [z_{n,m+1} \right. \\
 & - z_{n,m}] - A_{n,m} - \frac{1}{2} [z_{n,m} - z_{n,m-1}] \left. \right\} \\
 & + \frac{C_2 z_{n,m} \Delta x}{u_{n,m}} \left| \frac{\rho u_{n,m} r}{2\psi_{n,m}(\Delta\psi)} \right\{ u_{n,m+1} - u_{n,m-1} \right\} \left. \right\} \\
 & + \frac{C_3 z_{n,m}^{1/2} u_{n,m} r^2 \Delta x}{4\psi_{n,m}^2 (\Delta\psi)^2} \left\{ \rho_{n,m+1} - \rho_{n,m-1} \right\} \\
 & \left[\rho_{n,m} \left\{ k_{n,m+1} - k_{n,m-1} \right\} + k_{n,m} \left\{ \rho_{n,m+1} \right. \right. \\
 & \left. \left. - \rho_{n,m-1} \right\} \right] + \frac{C_4 z_{n,m}^{3/2} \Delta x}{u_{n,m}} \quad (72)
 \end{aligned}$$

Hence equations (69) and (72) are utilized to calculate the changes in k and z along the marching direction at mesh points inside the calculational field. However, special treatment of these equations is necessary along the axis of the flow as shown below.

The turbulent kinetic energy equation is given by (73)

$$\frac{\partial k}{\partial x} = \frac{1}{2\psi} \frac{\partial}{\partial \psi} \left\{ \frac{\rho u r^2 \mu t}{\psi} \frac{\partial k}{\partial \psi} \right\} + C_1 \mu t z^{\frac{1}{2}} \left| \frac{r}{\xi} - \frac{u}{\psi} \right| - \frac{k z^{\frac{1}{2}}}{u} \quad (73)$$

Now along the axis $r = \psi = 0$

$$\frac{\partial k}{\partial \psi} = \frac{\partial u}{\partial \psi} = 0$$

Hence, the first and second terms on the RHS of (73) must be evaluated along the axis since these terms are indefinite.

The first term is

$$\frac{1}{2\psi} \frac{\partial}{\partial \psi} \left\{ \frac{\rho u r^2 \mu t}{\psi} \frac{\partial k}{\partial \psi} \right\} \quad (76)$$

Define

$$\xi \equiv \frac{\psi^2}{2} \quad R \equiv \frac{r^2}{2}$$

Then $d\xi = \psi d\psi$ $dR = r dr$

From (69)

$$\psi \frac{\partial \psi}{\partial r} = \rho u r$$

and

$$\psi \partial \psi = \rho u r \partial r$$

$$d\xi = \rho u dR$$

and

$$\frac{dR}{d\xi} = \frac{1}{\rho u}$$

Hence, (76) becomes

$$\begin{aligned}
 \frac{1}{2} \frac{\partial}{\partial r} \left(\frac{\rho}{r} \right) &= \left\{ \frac{ur^2}{2} \mu_t - \frac{\partial k}{\partial r} \frac{\rho}{r} \right\} \frac{\partial^2}{\partial r^2} \\
 &= \frac{1}{2} \frac{\partial}{\partial r} \left\{ \frac{ur^2}{2} \mu_t - \frac{\partial k}{\partial r} \frac{\rho}{r} \right\} , \\
 &= \frac{1}{2} \frac{\partial}{\partial r} \left\{ \frac{ur^2}{2} \mu_t - \frac{\partial k}{\partial r} \frac{\rho}{r} \right\} \\
 &= \frac{1}{3r} \left\{ \rho u R \mu_t - \frac{\partial k}{\partial r} \right\}
 \end{aligned}$$

Differentiating

$$R = \frac{1}{3r} \left\{ \rho u \mu_t \frac{\partial k}{\partial r} \right\} + \left\{ \rho u \mu_t \frac{\partial k}{\partial r} \right\} \frac{\partial R}{\partial r}$$

Taking the limit as $r \rightarrow 0$

$$\begin{aligned}
 &= R \frac{\partial}{\partial r} \left\{ \rho u \mu_t \frac{\partial k}{\partial r} \right\} + \left\{ \rho u \mu_t \frac{\partial k}{\partial r} \right\} \frac{1}{3r} \\
 &= \mu_t \frac{\partial k}{\partial r} = \mu_t \frac{\partial k}{\partial \psi} \frac{\partial \psi}{\partial r} = \frac{\mu_t}{\psi} \frac{\partial k}{\partial \psi}
 \end{aligned}$$

now using L'Hospital's rule

$$\begin{aligned}
 h(\psi) &= \frac{f(\psi)}{g(\psi)} = \frac{\mu_t \frac{\partial k}{\partial \psi}}{\psi} \\
 \frac{f'(\psi)}{g'(\psi)} &= \frac{\frac{\partial}{\partial \psi} \left(\mu_t \frac{\partial k}{\partial \psi} \right)}{1} = \mu_t \frac{\frac{\partial^2 k}{\partial \psi^2}}{1} + \frac{\partial k}{\partial \psi} \frac{\partial \mu_t}{\partial \psi}
 \end{aligned}$$

$$\lim_{\psi \rightarrow 0}$$

but

$$\lim_{\psi \rightarrow 0} \frac{\partial k}{\partial \psi} = 0$$

Therefore the first term becomes

$$\mu t \frac{\partial^2 k}{\partial \psi^2}$$

The second term is given by

$$c_1 \mu t z^{\frac{1}{2}} \left| \frac{r}{\psi} \frac{\partial u}{\partial \psi} \right|$$

Applying L'Hospital's rule to a portion of this term gives

$$h(\psi) = \frac{f(\psi)}{g(\psi)} = \frac{r \frac{\partial u}{\partial \psi}}{\psi}$$
$$\lim_{\psi \rightarrow 0} \frac{f'(\psi)}{g'(\psi)} = \frac{r \frac{\partial^2 u}{\partial \psi^2} + \frac{\partial u}{\partial \psi} \frac{\partial r}{\partial \psi}}{1}$$

Now taking the limit as $r \rightarrow \infty$: $\frac{\delta u}{\delta \psi} \rightarrow 0$ and hence the second term $\rightarrow 0$. The third term is unaffected by the limit process and we have

$$\boxed{\frac{\partial k}{\partial x} = \mu t \frac{\partial^2 k}{\partial \psi^2} - \frac{k z^{\frac{1}{2}}}{u}}$$

Along the axis (77)

The z equation is given by (75)

$$\begin{aligned}
 \frac{\partial z}{\partial x} &= \frac{1}{2\psi} \frac{\partial}{\partial \psi} \left\{ \frac{\rho u r^2}{\psi} \frac{\partial z}{\partial \psi} \right\} + \frac{c_2 z}{u} \left| \frac{\rho u r}{\psi} \frac{\partial u}{\partial \psi} \right| \\
 &+ c_3 z^{\frac{1}{2}} \frac{u r^2}{\psi^2} \left(\frac{\partial \rho}{\partial \psi} \right) \frac{\partial}{\partial \psi} (\rho k) + \frac{c_4 z^{\frac{3}{2}}}{u} \quad (75)
 \end{aligned}$$

The first two terms on the RHS of (75) are analogous to the first two terms on the RHS of (74), and are evaluated analogously. Hence looking at the third term

$$c_3 z^{\frac{1}{2}} \frac{u r^2}{\psi^2} \left(\frac{\partial \rho}{\partial \psi} \right) \frac{\partial}{\partial \psi} (\rho k) \quad (78)$$

$$\lim r = \psi \rightarrow 0$$

Making the same substitution as before, define

$$\xi = \frac{z^{\frac{1}{2}}}{2}$$

$$\text{then } \frac{d\xi}{d\psi} = \frac{1}{\psi}$$

and the third term (78) becomes

$$c_3 z^{\frac{1}{2}} \frac{u r^2}{\psi^2} \left(\frac{\partial \rho}{\partial \xi} \right) \frac{\partial \xi}{\partial \psi} \left[\frac{\partial}{\partial \xi} (\rho k) \frac{\partial \xi}{\partial \psi} \right]$$

$$c_3 z^{\frac{1}{2}} \frac{u r^2}{\psi^2} \left(\frac{\partial \rho}{\partial \xi} \right) \psi \left[\frac{\partial}{\partial \xi} (\rho k) \psi \right]$$

and taking the limit as $r \rightarrow 0$

$$\lim_{r \rightarrow 0} C_3 z^{\frac{1}{2}} u r^2 \left(\frac{\partial p}{\partial \xi} \right) \frac{\partial}{\partial \xi} (ok) = 0$$

The fourth term remains as is and the z-equation along the axis becomes --

$$\frac{\partial z}{\partial x} = \mu_t \frac{\partial^2 z}{\partial \psi^2} + C_4 \frac{z^{\frac{3}{2}}}{u}$$

Along the axis

(79)

Hence, evaluation of the turbulence model equations for the case when $r = 0$ along the axis becomes according to (77) and (78)

$$\frac{\partial k}{\partial x} = \mu_t \frac{\partial^2 k}{\partial \psi^2} - \frac{k z^{\frac{1}{2}}}{u}$$

$$\frac{\partial z}{\partial x} = \mu_t \frac{\partial^2 z}{\partial \psi^2} + C_4 \frac{z^{\frac{3}{2}}}{u}$$

Now when compressibility effects are important the last term in the k-equation must also be evaluated along the axis

$$\frac{C_6 \bar{R}_0^2 k u r^2 \mu_t}{M w_2 C_p p_2 \psi^2} \left(\frac{\partial u}{\partial \psi} \right)^2 \quad (80)$$

Investigate this term in the limit as

$$r \rightarrow 0 \quad \psi \rightarrow 0$$

$$\frac{\partial k}{\partial \psi} \rightarrow 0 \quad \frac{\partial u}{\partial \psi} \rightarrow 0$$

Rewrite (80) as

$$\frac{B}{\psi} \left(\frac{\partial u}{\partial \psi} \right)^2 \quad (81)$$

where

$$B = \frac{C_6 \bar{R}_D^2 k u r^2 \mu_t}{M w_2 C p_2 \psi}$$

Then using L'Hospital's rule to (81)

$$\begin{aligned} h(\psi) &= \frac{f(\psi)}{g(\psi)} = \frac{B \left(\frac{\partial u}{\partial \psi} \right)^2}{\psi} \\ \frac{f'(\psi)}{g'(\psi)} &= \frac{2B \left(\frac{\partial u}{\partial \psi} \right) \left(\frac{\partial^2 u}{\partial \psi^2} \right) + \left(\frac{\partial u}{\partial \psi} \right)^2 \left(\frac{\partial B}{\partial \psi} \right)}{1} \\ &= 0 \end{aligned}$$

Hence in the limit as $r \rightarrow 0$ this term adds nothing.

Therefore equations (69) and (72) for field mesh points and (84) and (85) for points along the axis determine the turbulence kinetic energy and the pseudo vorticity in the shear layer.

This formulation was coded and added to the BOAT portion of the SPE code now under development. These coding changes were input via an update to the main code and are detailed in Appendix B.

The IKE equations along the axis are

$$\frac{\partial k}{\partial x} = \mu_t \frac{\partial^2 k}{\partial \psi^2} - \frac{k z^{\frac{1}{2}}}{u} \quad (82)$$

$$\frac{\partial z}{\partial x} = \mu_t \frac{\partial^2 z}{\partial \psi^2} + C_4 \frac{z^{\frac{3}{2}}}{u} \quad (83)$$

$$\frac{\partial^2 f}{\partial \psi^2} = \frac{f_{n,m+1} - 2f_{n,m} + f_{n,m-1}}{(\Delta \psi)^2}$$

Since $f_{n-1, m}$ does not exist, assume

$$f_{n,m-1} = f_{n,m}$$

then

$$\frac{\partial^2 f}{\partial \psi^2} = \frac{f_{n,m+1} - f_{n,m}}{(\Delta \psi)^2}$$

and for the special case along the axis

$$\left. \frac{\partial^2 f}{\partial \psi^2} \right|_{r=0} = \frac{f_{n,2} - f_{n,1}}{(\Delta \psi)^2}$$

Therefore, equation (82) becomes

$$\Delta k_{n,m} = \frac{\mu_t \Delta x}{(\Delta \psi)^2} (k_{n,2} - k_{n,1}) - \frac{k_{n,1} z_{n,1}^{\frac{3}{2}} \Delta x}{u_{n,1}}$$

So that

$$k_{n+1,1} = k_{n,1} + \frac{\mu_t \Delta x}{(\Delta \psi)^2} (k_{n,2} - k_{n,1}) - \frac{\Delta x k_{n,1} z_{n,1}^{\frac{3}{2}}}{u_{n,1}} \quad (84)$$

Along the axis

and likewise

$$z_{n+1,1} = z_{n,1} + \frac{u_t \Delta x}{(\Delta y)^2} (z_{n,2} - z_{n,1}) - C_4 \frac{\Delta x z_{n,1}^3}{u_{n,1}} \quad (85)$$

Along the axis

V. NON-REACTING SHEAR LAYER COMPARISON

In order to evaluate the various turbulence mixing models, predictions were made corresponding to the careful experimental measurements made by Brown and Roshko [1] over an extended period of time. The experiments were made in a laboratory utilizing a splitter plate separating two 4 x 1-inch 2-D nozzles. The principal aim of this experimental work was to investigate the effect of density differences between the two mixing layers. This was accomplished experimentally by using various mixtures of He and N₂. Ar was also used in some rare instances. These two streams were turbulent with the Re number $\frac{U_\infty x}{\nu}$ in the range of $\approx 10^6$. The experimental device was run at low speeds in the range of ≈ 50 fps. Freestream velocity and density ratios on the order of ≈ 7 were run experimentally. This work showed that the large structure existed over all the density ranges tested.

Predictions were made for all the experimental runs made by Brown and Roshko and are presented subsequently. Velocity and density profiles were calculated as a function of y (x_v) where x_v is the virtual origin of the shear layer and y is the distance above or below the dividing streamline. The dividing streamline was located utilizing a numerical integration scheme. The details and limitations of this calculation is given in Appendix A.

In addition to the velocity and density profiles that were compared for the data of Brown and Roshko, the growth of the shear layer as a function of velocity ratio was compared. As a basis for this comparison, they used the velocity profile maximum slope thickness and its derivative

$$\delta_v = \frac{U_j - U_e}{\left(\frac{\partial U}{\partial Y}\right)_{\max}} \quad (86)$$

$$\delta'_\omega = \frac{d\delta\omega}{dx} = \frac{\delta\omega}{x - x_0}$$

or

$$\delta'_\omega = \frac{U_j - U_e}{\left(\frac{\partial U}{\partial y}\right)_{\max} (x - x_0)} \quad (87)$$

Equation (87) was used for the comparison.

Results comparing the shear layer flow utilizing the two turbulence kinetic energy models with experimental data are shown in *Figure 9*. This is a comparison of the constant density air-air case with a jet velocity of 32.8 feet/second and an external stream velocity of 4.7 feet/second. The flow was at a constant pressure of 102.9 psia.

Note that the agreement between theory and experiment is very good for both the $k\epsilon 2$ and the $k\omega'$ turbulence models. The shear width agreement is excellent and velocity profile slope is very good. The $k\epsilon 2$ model shows a little better agreement with the slope while the $k\omega'$ model shows a slightly better shear width agreement. Overall it can be said that the agreement with both is very good.

The next comparison made was another constant density air-air case for which the pressure was maintained constant at 102.9 psia. For this case, the jet velocity was held at 32.8 feet/second while the external stream velocity was increased to 12.5 feet/second. This comparison is shown in *Figure 10*.

Note that the agreement between theory and experiment is again pretty good for both turbulence models. The slope is reasonable for both and the width of the shear layer is approximately the same for both. The $k\omega'$ model falls closer to the actual data than does the $k\epsilon 2$ model.

Hence, for the constant density turbulent 2-D shear layer, the turbulence prediction models are doing reasonably well at predicting the growth and velocity profiles.

In order to evaluate shear layer flows, where multiple species are involved such as for the He-N_2 experiments, it is necessary to know the value of the turbulent Prandtl number. This

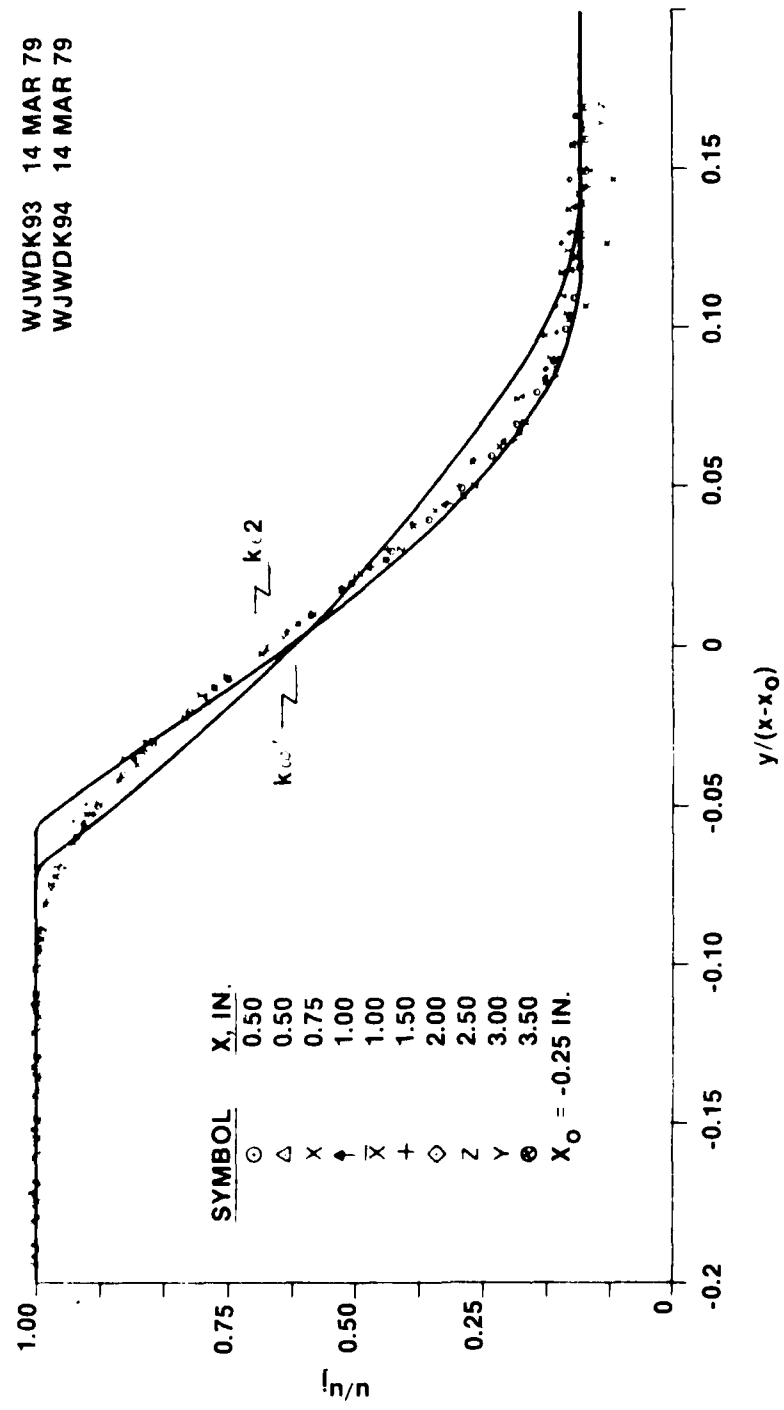


Figure 9. Velocity profile comparison for air/air shear layer -
Table 6, case number 1.

WJWDK3X 14 MAR 79
WJWDK97 12 MAR 79

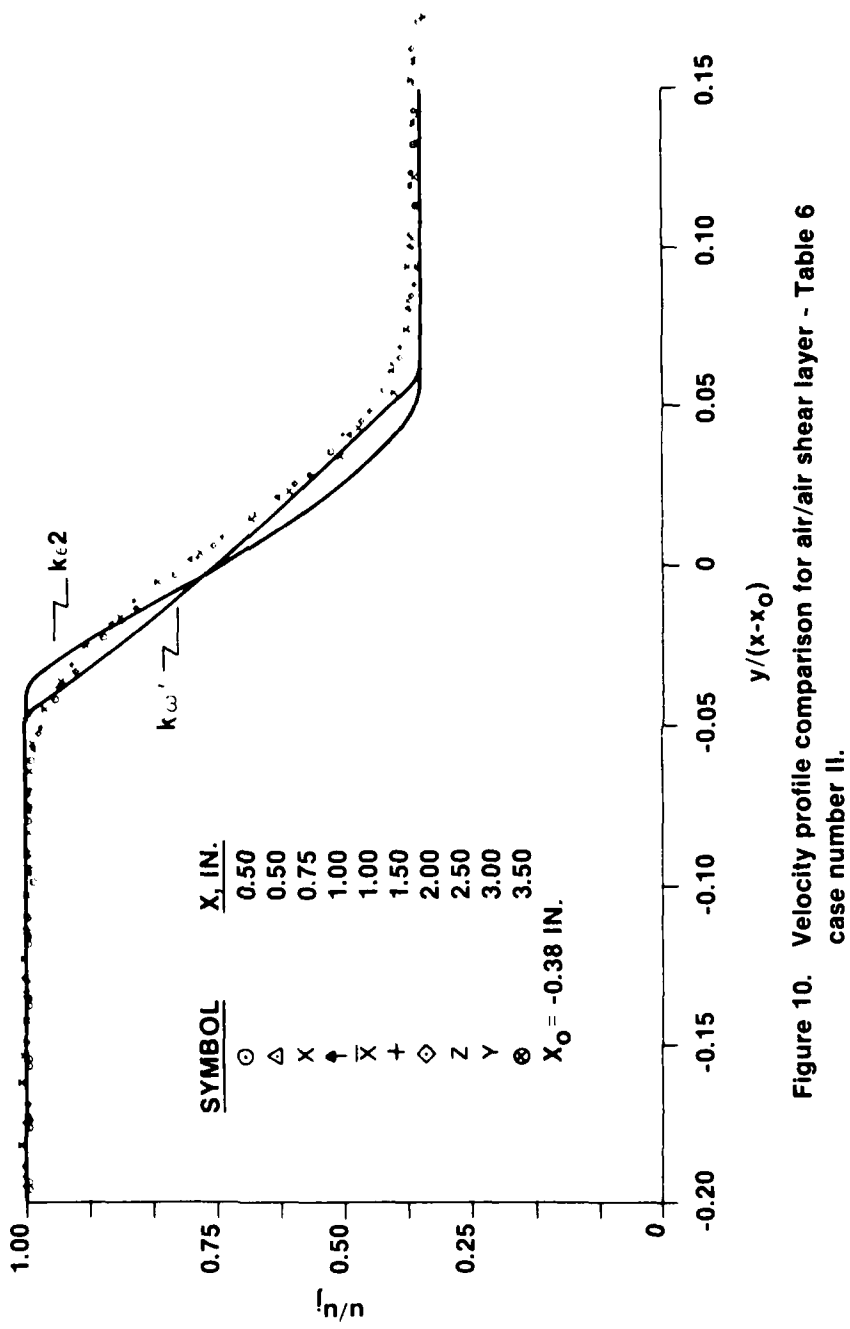


Figure 10. Velocity profile comparison for air/air shear layer - Table 6
case number II.

parameter arises in the governing differential equations to account for differences between the velocity profile and the specie profiles. This parameter is not known *a priori*. It can be determined however from the experimental data.

Brown and Roshio [1] found that for all cases of He/N₂ shear layers, the spreading angle of the density profile was greater than that for the velocity profile. In order to evaluate this, they constructed an eddy-viscosity model and deduced that the turbulent Prandtl number should be between 0.2 and 0.3.

Figure 11 compares the predicted ρu profile for the conditions of Case V shown in Table 6 utilizing the present $k\epsilon 2$ turbulence kinetic energy model. Note that there is qualitative agreement between the predictions and the experiment for a turbulent Prandtl number of 0.3. Had this been for the constant density case, the functional relationship would have been much different, approaching a constant value of 1.0. The trend toward matching the experimental data is to run at lower Pr_t numbers. However, this study did not investigate the quantitative differences as a lower Pr_t is utilized. One reason for this was the marked increase in computer runtime that would have been necessary. This is, however, a parameter that needs to be investigated in future investigations of turbulence modeling. Therefore, $Pr_t = 0.3$ was chosen for the corresponding calculation.

TABLE 6. INITIAL CONDITIONS FOR SHEAR LAYER COMPARISON CASES

CASE NO.	u_j/u_e	ρ_j/ρ_e	JET STREAM CONSTITUENT	EXTERNAL STREAM CONSTITUENT
I	7.00	1.00	AIR	AIR
II	2.62	1.00	AIR	AIR
III	2.65	7.00	N ₂	He
IV	2.65	0.143	He	N ₂
V	7.00	0.143	He	N ₂

EFFECT OF THE TURBULENT PRANDTL NO.
COMPARISON FOR FIGURE 16
 $Pr_l = 0.3$ RESULTS

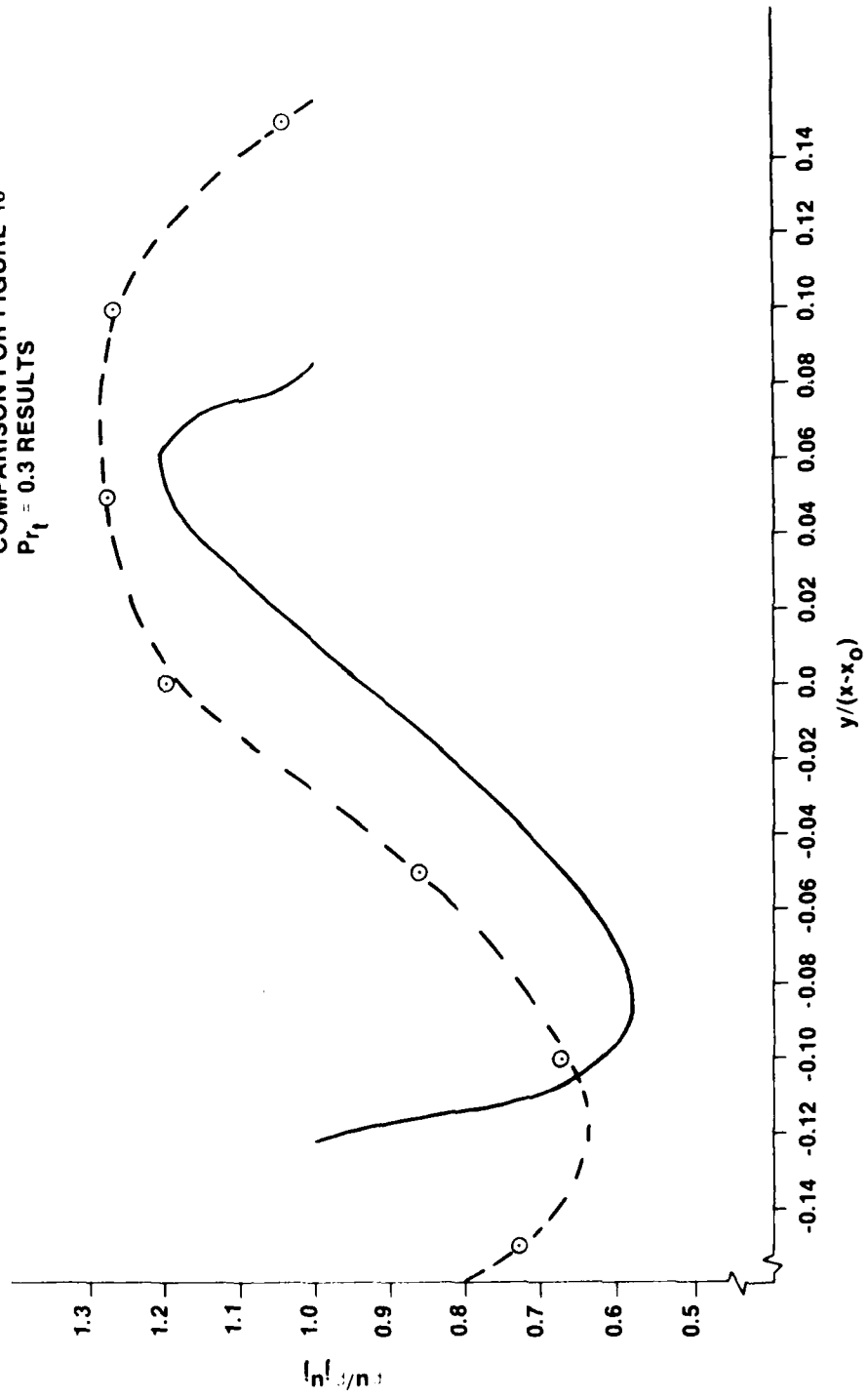


Figure 11. ρ_u Profile comparison for He/N₂ shear layer Table 6-
case number V.

A comparison of the two turbulent kinetic energy models with experiment is shown in terms of the velocity profile in *Figure 12* for case III (*Table 6*). For this case, the jet velocity was 32.8 feet/second while the external stream velocity was 12.4 feet/second. The jet fluid was N₂ while the external fluid was He giving a density ratio of 7. As before, the pressure was held constant at 102.9 psia.

Both models show reasonable agreement with the data. The velocity profile slope is more nearly constant for the $k\epsilon^2$ as opposed to the $k\omega'$ model. There is some disagreement with the width of the mixing layer between the models where the width is too great on the high velocity side on one and too narrow on the low velocity side on the other and vice versa.

The first density profile comparison is shown in *Figure 13*. (Case III) The most notable aspect of this comparison is the lack of agreement between theory and experiment. In particular the slope of density profile on the N₂ side is far too large; the $k\epsilon^2$ model demonstrating the worst agreement between the two. The width of the density layer is very close for the $k\omega'$ model and somewhat worse for the $k\epsilon^2$ model. The absolute agreement between experiment and theory is poor everywhere across the mixing layer and density errors of ≈ 100 percent can be seen. Had the disagreement occurred only in the edge regions of the shear layer, concern for this would have been lessened. Unfortunately, the agreement is uniformly poor.

The next comparison of the turbulent kinetic energy models with experiment is shown in terms of the velocity profile in *Figure 14* for case IV (*Table 6*). For this case, the jet velocity was 32.8 feet/second while the external stream velocity was 12.4 feet/second. The jet fluid was He while the external fluid was N₂ giving a density ratio of 0.143, the external stream being the more dense. Again the pressure was held constant at 102.9 psia. A turbulent Prandtl number of 0.7 was used in the predictions.

For this case, the velocity profile comparison begins to look poor, especially on the He side of the shear layer. Some of this poor agreement can be attributed to being in the edge region of the shear layer. However, it is clear that this is not the only reason for the disagreement. Notice that the shear layer width is predicted much more narrow than that observed experimentally. Further, the velocity profile slope on the He side is considerably in error. This velocity profile comparison is the worst that has occurred so far.

The density profile comparison for Case IV is shown in *Figure 15*. The same problems that were evident in the velocity profile comparison are magnified for the density profile. The predicted density width is too narrow and discrepancies are most notable in the slope of the

WJWDK1Z 20 MAR 79
WJWDK1Y 20 MAR 79

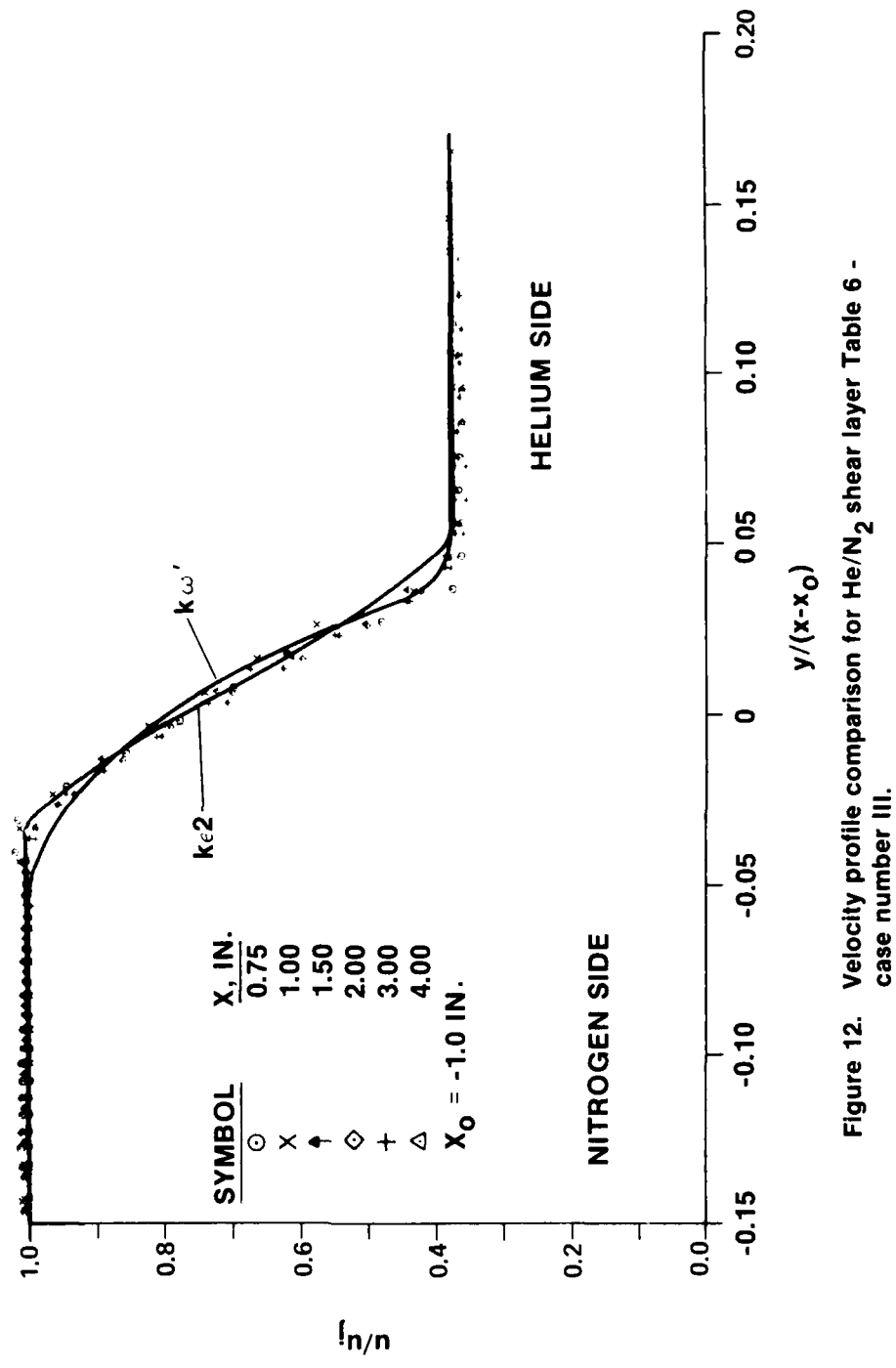


Figure 12. Velocity profile comparison for He/N₂ shear layer Table 6 - case number III.

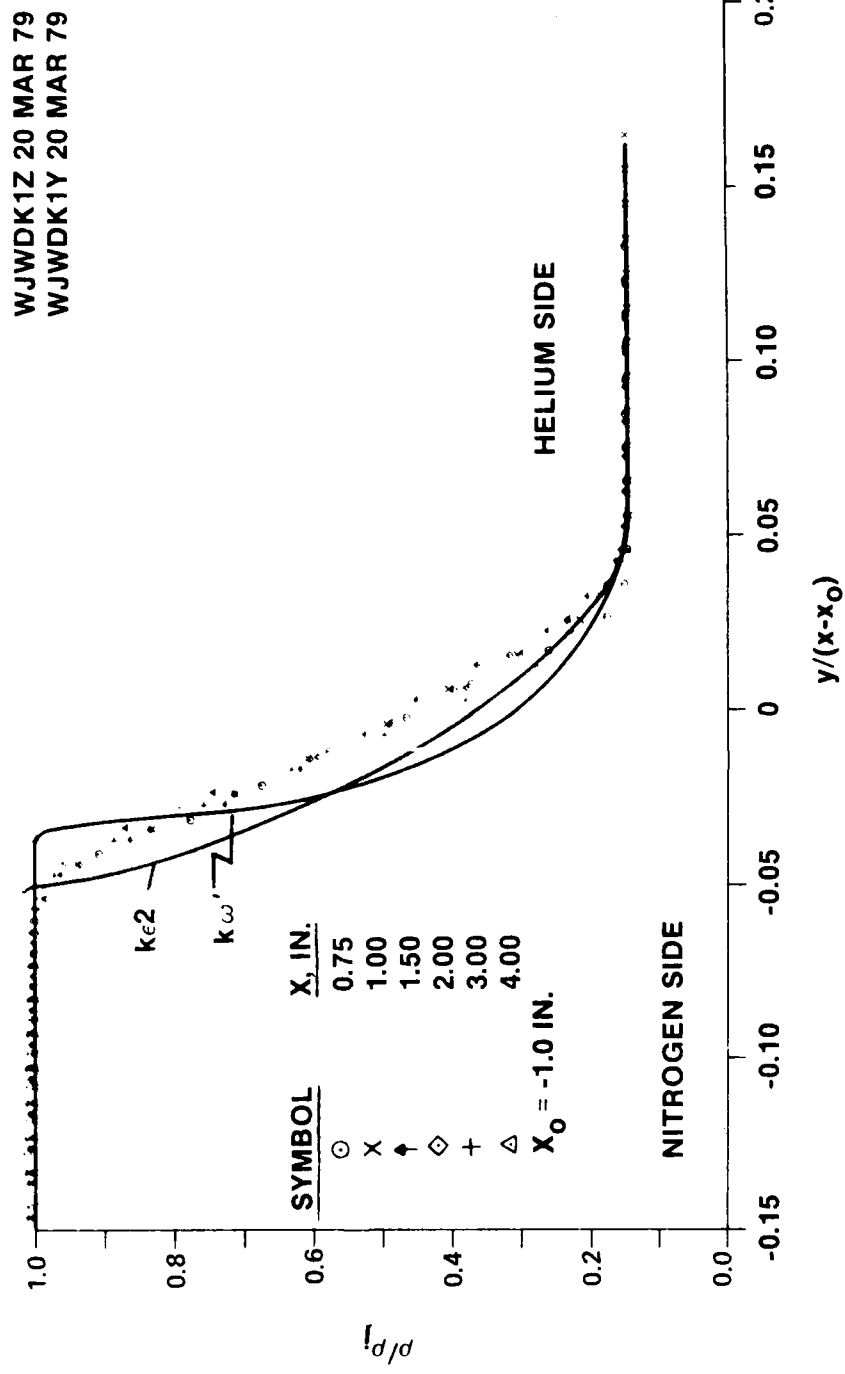


Figure 13. Density profile comparison for He/N_2 shear layer - Table 6,
case number III.

WJWDKAK - 15 MAR 79
WJWDKAI - 15 MAR 79

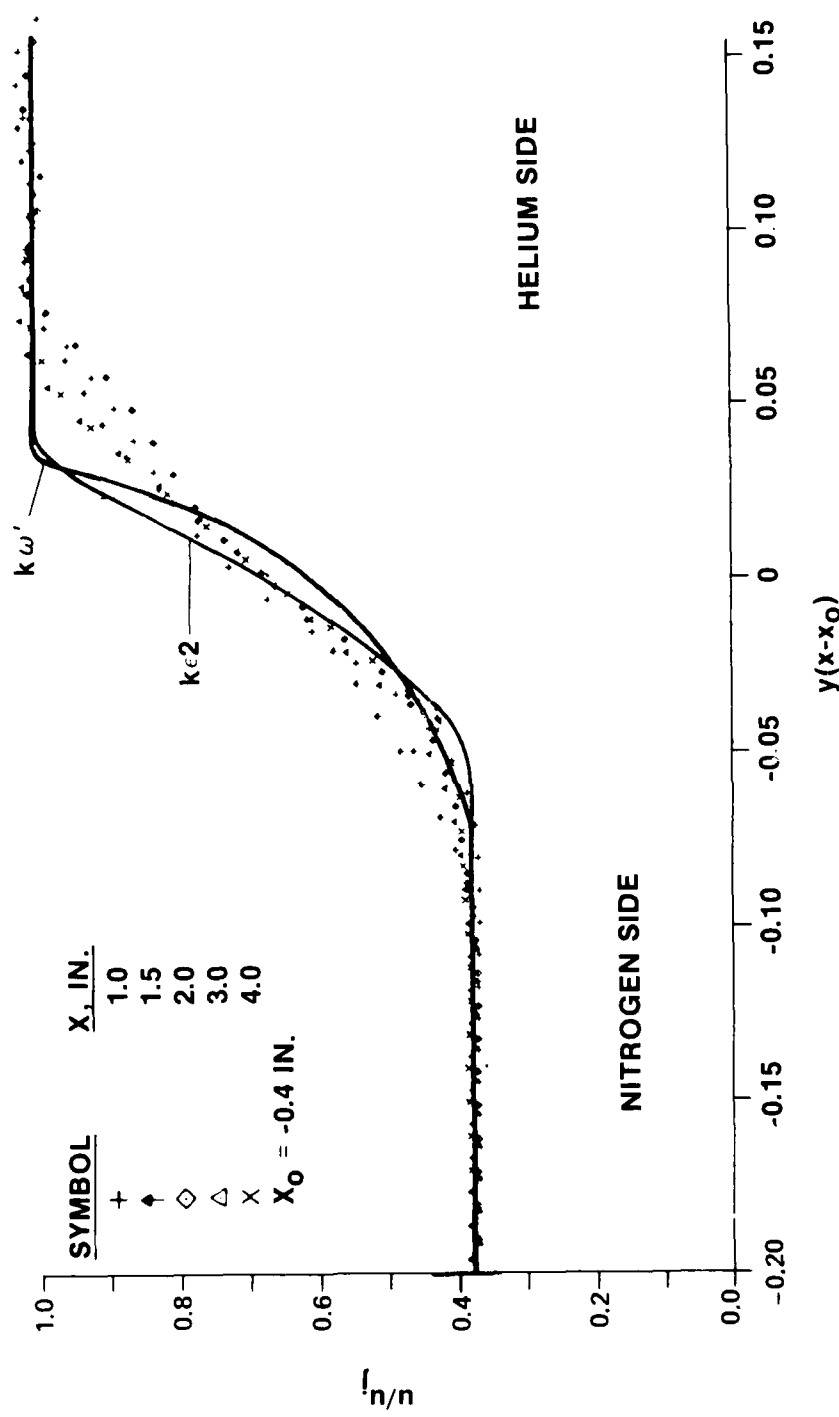


Figure 14. Velocity profile comparison for He/N₂ shear layer, Table 6 -
case number IV.

WJWDKAK - 15 MAR 79
WJWDKAI - 15 MAR 79

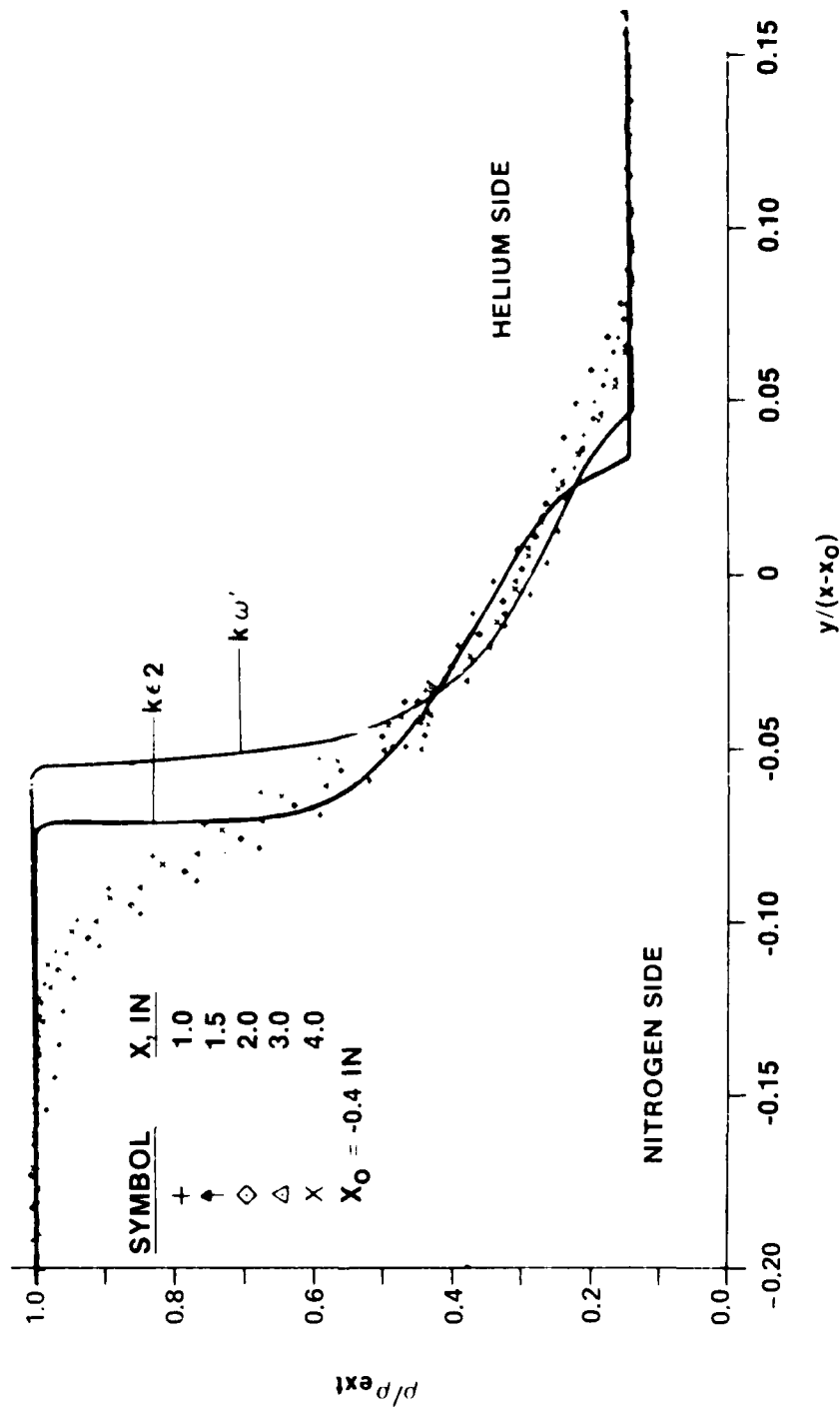


Figure 15. Density profile comparison for He/N₂ shear layer - Table 6,
case number IV.

density profile on the N_2 side. The differences in width between the velocity and density profiles was accounted for in the model by running the model at a turbulent Prandtl number, $Pr_t=0.3$ as described earlier. It is obvious that the resulting theoretical difference in width of the two layers is far less than the experimental width difference. Thus, it is obvious that there are some serious problems in the turbulence modeling for flows have a large density difference.

The next comparison of the turbulent kinetic energy models with experiment are the most interesting of the shear flows compared since the density ratio of 7 that was run is very nearly that seen in rocket exhaust plume firings. The velocity profile is shown in *Figure 16* for Case V (*Table 6*). For this case, the jet velocity was 32.8 feet second while the external stream velocity was 4.7 feet second. The jet fluid was He while the external fluid was N_2 giving a density ratio of 7, the jet stream being the less dense stream. The pressure was held constant at 102.9 psia.

The velocity profile comparison for this case is shown in *Figure 16*. As was the situation in Case IV, the velocity profile comparison looks poor, especially on the He side of the mixing layer. Note the substantial difference between the velocity profile slopes predicted by both models and measured. Again the shear layer width predicted is more narrow than that measured. The comparison is very similar to that of Case IV.

The density profile comparison for Case V is shown in *Figure 17*. Again as in Case IV, the predicted density width is too narrow and discrepancies are most notable in the slope of the density profile on the N_2 side. The differences in width between the velocity and density profiles were accounted for in the model by running at a $Pr_t=0.3$. Again the predicted width difference between the predicted density and velocity profiles are far less than between the measured profiles. The comparison between experiment and theory is the worst thus far seen and as mentioned earlier, this is the case of most interest since it more closely matches a real rocket plume in terms of density ratio.

The spreading rate for all the previous cases was calculated and compared with the experimental data. *Figure 18* shows the comparison for the $k\epsilon 2$ model and the comparison for the $k\omega$ model is shown in *Figure 19*. There is one difference between the velocity profile slope of the experimental data and the theoretical calculations Brown and Roshko used $\left(\frac{\delta u}{\delta y}\right)_{MAX}$

while $\left(\frac{\delta u}{\delta y}\right)_{AVG}$ was utilized for the theoretical calculations. In calculating the $\left(\frac{\delta u}{\delta y}\right)_{AVG}$, only the center 50 percent of the profile was utilized in determining the average slope to minimize edge gradient effects.

WJWDKC4 - 5 MAR 79
WJWDKBH - 6 MAR 79

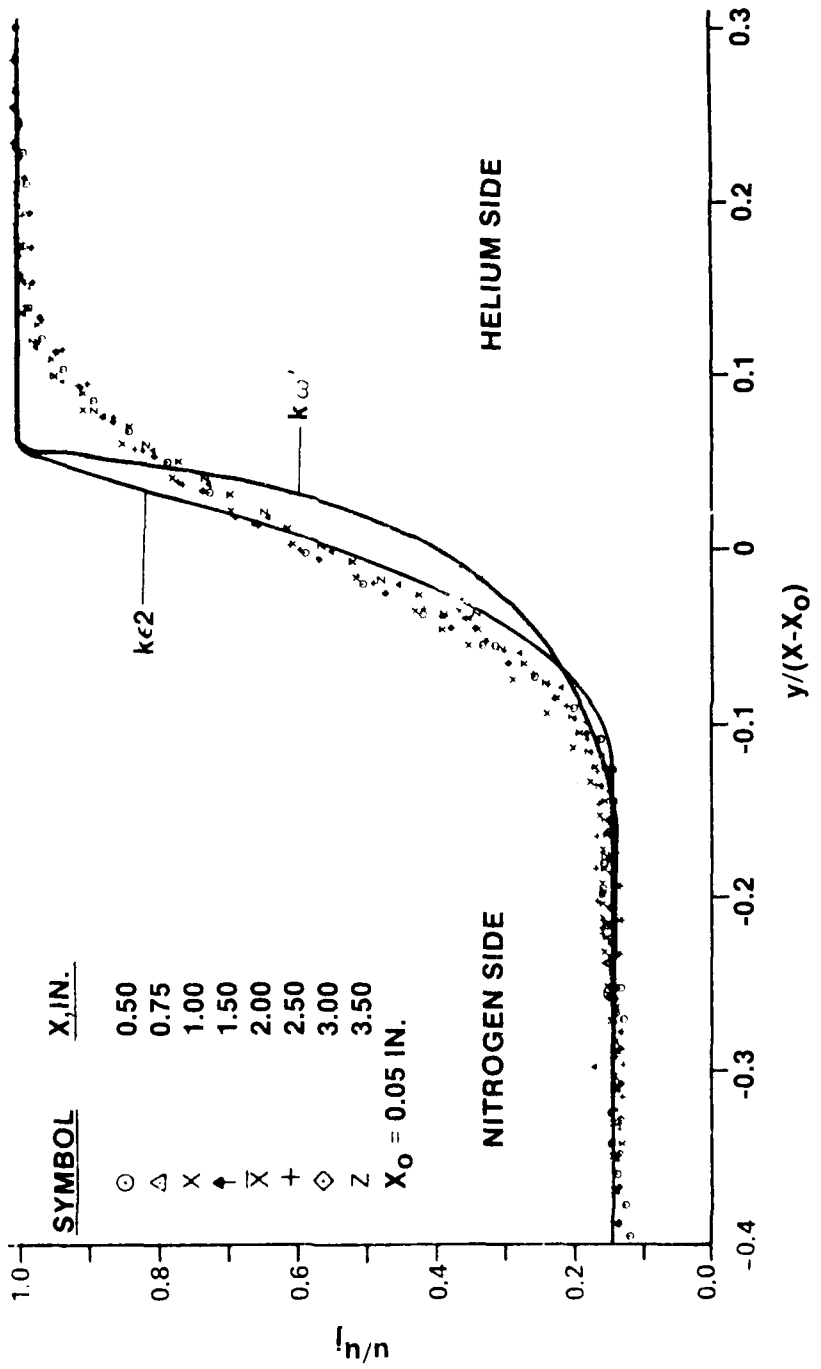


Figure 16. Velocity profile comparison for He/N₂ shear layer - Table 6 -
case number V.

WJWDKC4 - 5 MAR 79
WJWDKBA - 6 MAR 79

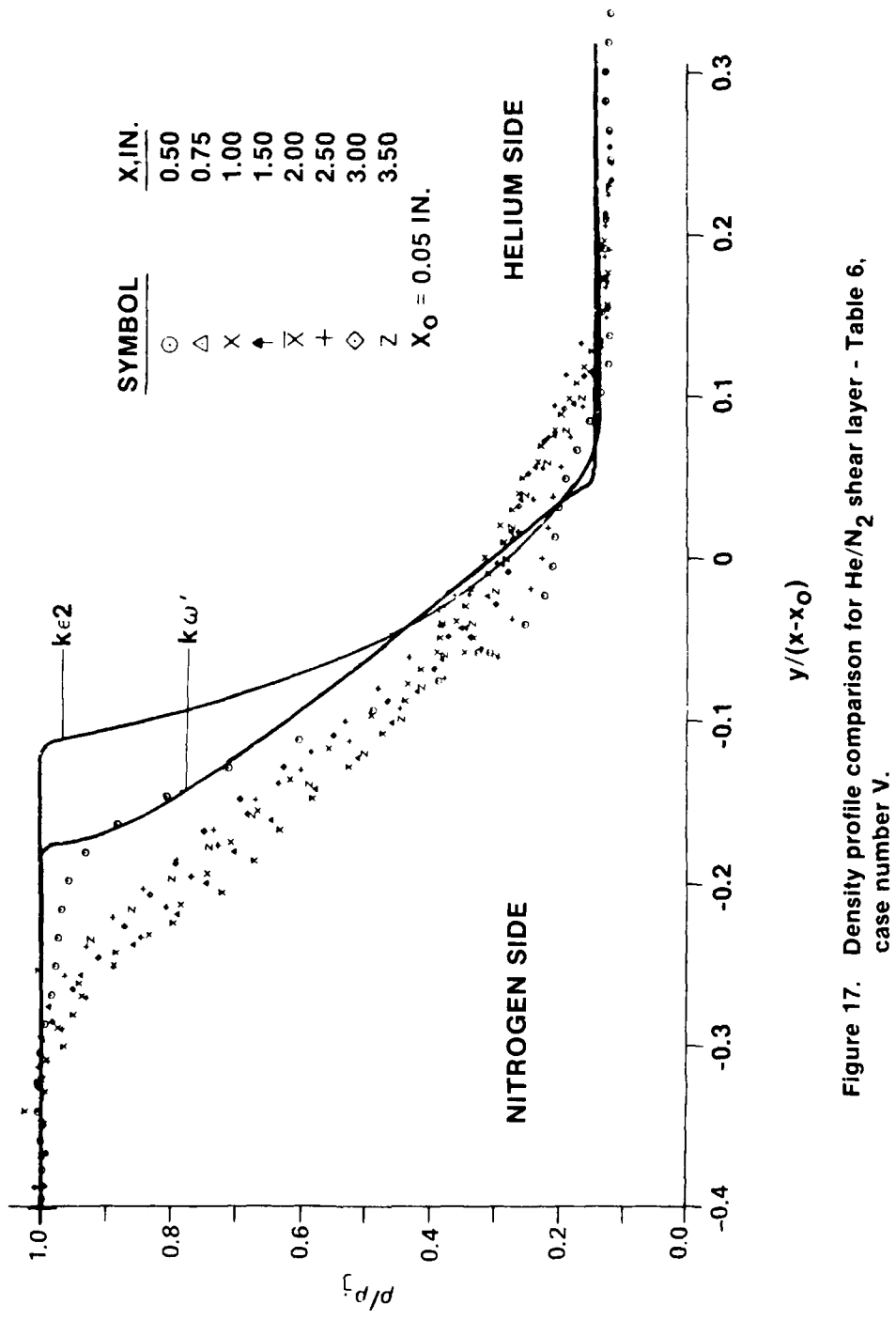


Figure 17. Density profile comparison for He/N_2 shear layer - Table 6, case number V.

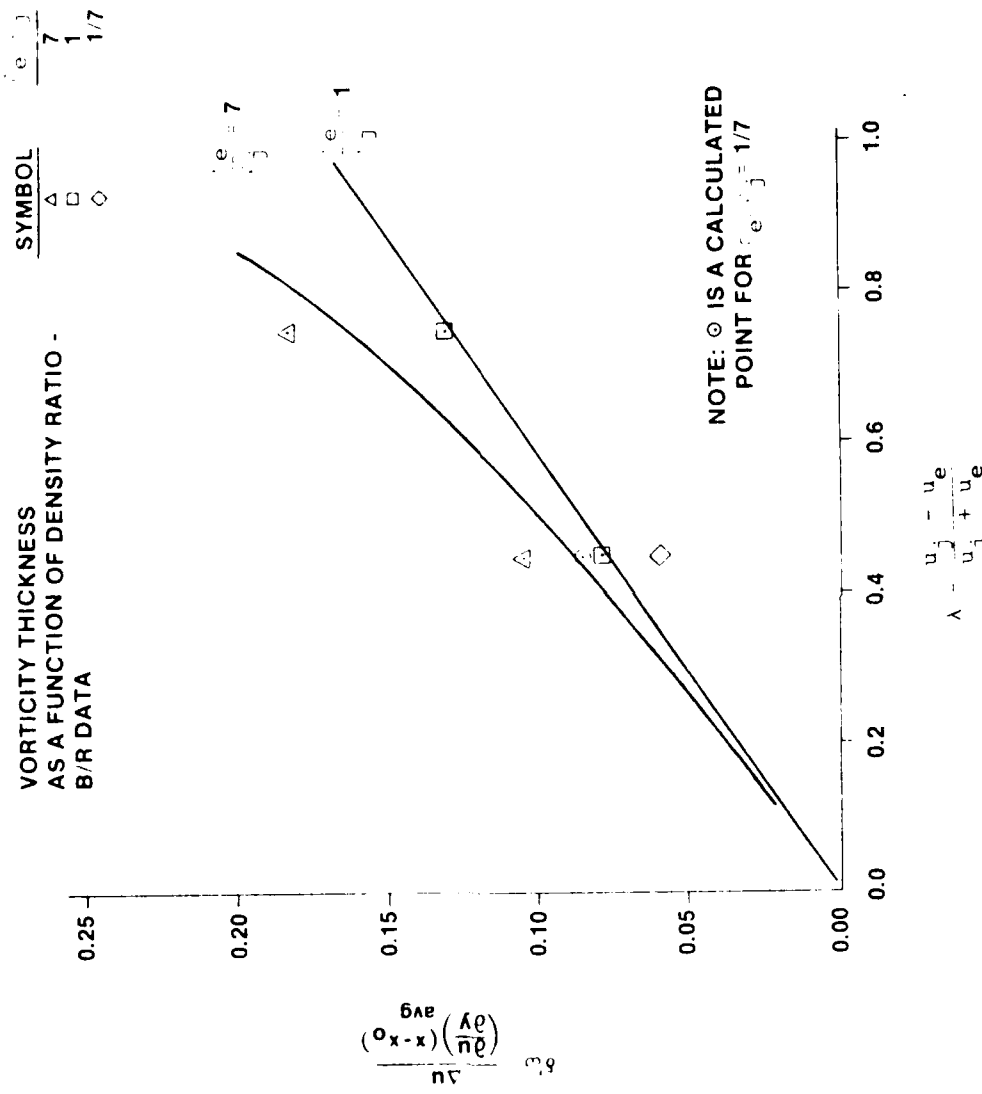


Figure 18. Comparison of calculated and measured effect of density ratio on spreading rate ($k_e = 2$ turbulence model).

$$\lambda = \frac{u_{ij} - u_e}{u_{ij} + u_e}$$

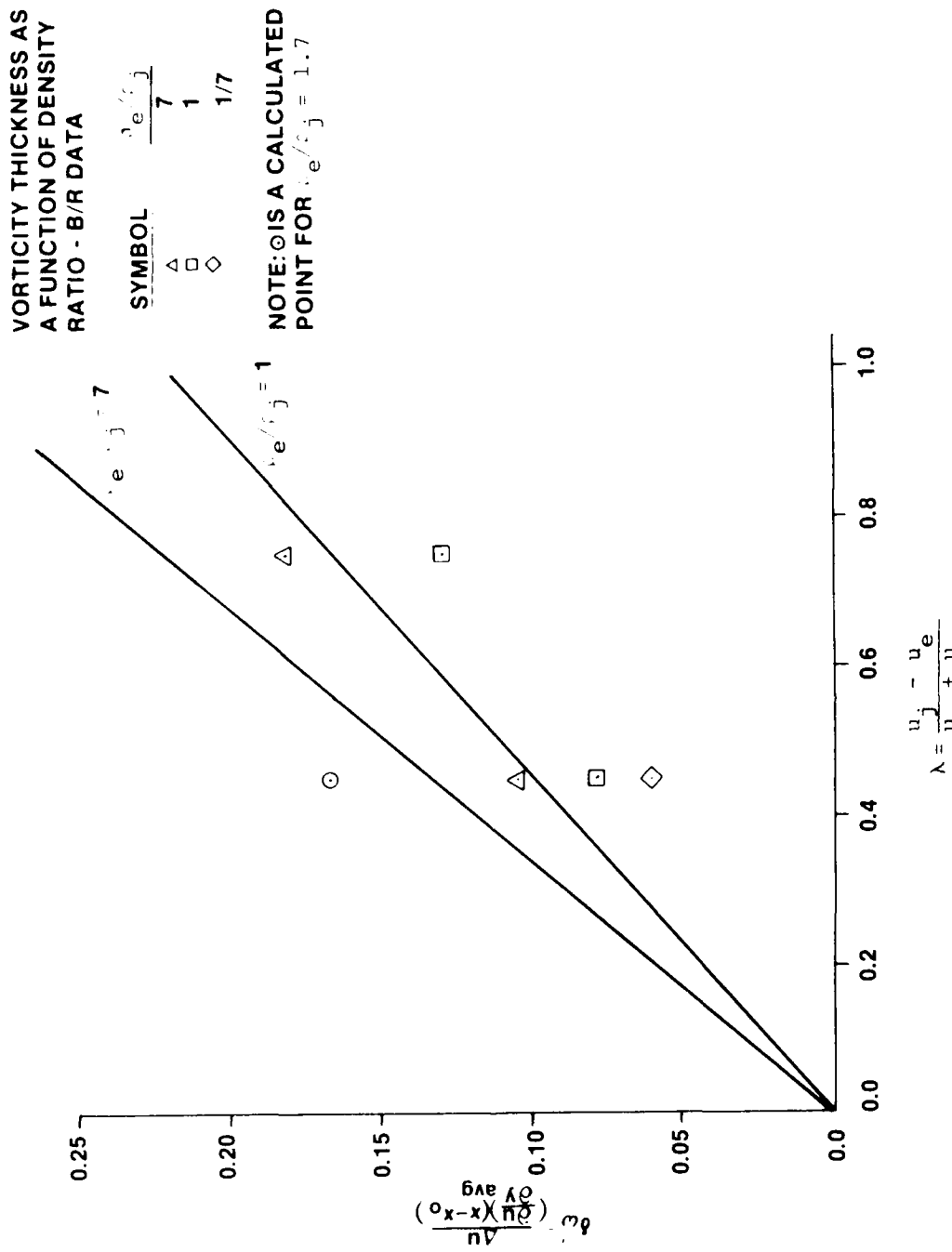


Figure 19. Comparison of calculated and measured effect of density ratio on spreading rate (Saffman k_ω turbulence model).

It should be noted that the $k\epsilon 2$ model gave the best agreement between theory and experiment. For the case with equal densities for both the jet and external streams, the data points fall exactly on the theoretical curve.

The agreement between theory and experiment is the worst for the case where $\rho_e / \rho = 1$ for both models.

The agreement or lack thereof between experiment and theory is almost totally governed by $\frac{\partial u}{\partial y}$. Since the spreading rate is so sensitive to this parameter, these comparisons are much less meaningful than the density profile for example.

VI. NON-REACTING JET COMPARISON

The previous comparisons of the turbulence mixing models were made utilizing the experimental data of Brown and Roshko which were for two dimensional shear layers at low velocities (30 feet second or less). Since the applications of interest for this work are all at much higher velocities and since the geometry is axisymmetric, it was felt that comparison with some of the NASA Shear Flow Conference Data [7] was in order. Hence comparisons were made for axisymmetric jet data in order to compare the turbulence models. Two sets of experimental data were chosen from the NASA Shear Flow Conference for comparison with the two turbulence kinetic energy models, the $k\epsilon 2$ and $k\omega'$. *Table 7* details the flow conditions that were run during the experiments.

These two cases cover the spectrum of expected velocity and density ratios that one might expect to see in a realistic rocket plume case. They are, however, not in the same experiment. For both of these cases only experimental velocity profiles were measured. This is

TABLE 7. INITIAL CONDITIONS FOR JET MIXING COMPARISON CASES

CASE NO.	u_j / u_e	ρ_j / ρ_e	JET STREAM CONSTITUENT	JET STREAM CONSTITUENT	M_j	M_e
I	∞	1.97	AIR	AIR	2.2	0
II	2.72	0.06	H_2	AIR	0.89	1.32

unfortunate since, as was seen in the preceding comparisons for the shear layer, the density profiles are a much more stringent test for the accuracy of the theoretical models. Furthermore, since species concentration is the one of the quantities used directly in rocket plume applications, it is a more important measure of the accuracy of the turbulence models.

Another important consideration for rocket exhaust plumes is the compressibility effects. The importance of this effect is addressed for Case 1 (*Table 7*) where there is an infinite velocity ratio between the jet and the external stream. Certainly Brown and Roshko have pointed out the importance of this effect and the accuracy with which this effect is accounted for is shown below.

The first comparison made was for an $M=2.2$ air jet exhausting into still air. The jet velocity was 1765 feet/second and the pressure was ambient. The density ratio was as shown in *Table 7* for Case 1.

This is the homogeneous case in which the density ratio is determined by the Mach number as opposed to molecular weight differences in the jet and the external stream. Hence, compressibility effects are important for this case. Since the $k\epsilon^2$ turbulence model does not account for compressibility effects, a compressibility correction factor originating from some empirical work at General Applied Science Laboratory (GASL) was utilized to account for this effect. The details of this correction were presented in an earlier section.

Figure 20 compares model predictions for the $k\epsilon^2$ and $k\omega'$ turbulence models without compressibility with the experimental data. It should be noted from the centerline velocity profile that the predicted core length of the jet is too short compared with experiment. The $k\omega'$ core length being much shorter than the $k\epsilon^2$ core length. This indicates that the entrainment of the ambient stream is much too large and the mixing distance much too short for the case of a high relative velocity between the two streams.

However, when the compressibility effects are accounted for by utilizing the GASL compressibility factor for the $k\epsilon^2$ turbulence model and via the addition of a term in the modeling equation for the $k\omega'$ model, the results show a marked improvement. In fact the agreement between prediction and experiment is excellent for the $k\omega'$ turbulence model with compressibility. This agreement is shown in *Figure 21*. Note that the core length prediction is correct and the centerline velocity agreement is excellent out to 60 jet nozzle radii. The agreement deteriorates from that point on downstream but is still quite reasonable. The $k\epsilon^2$ model with compressibility correction predicts a core length that is too long and centerline velocities that are too high until the centerline velocity has dropped to 30 percent of its original

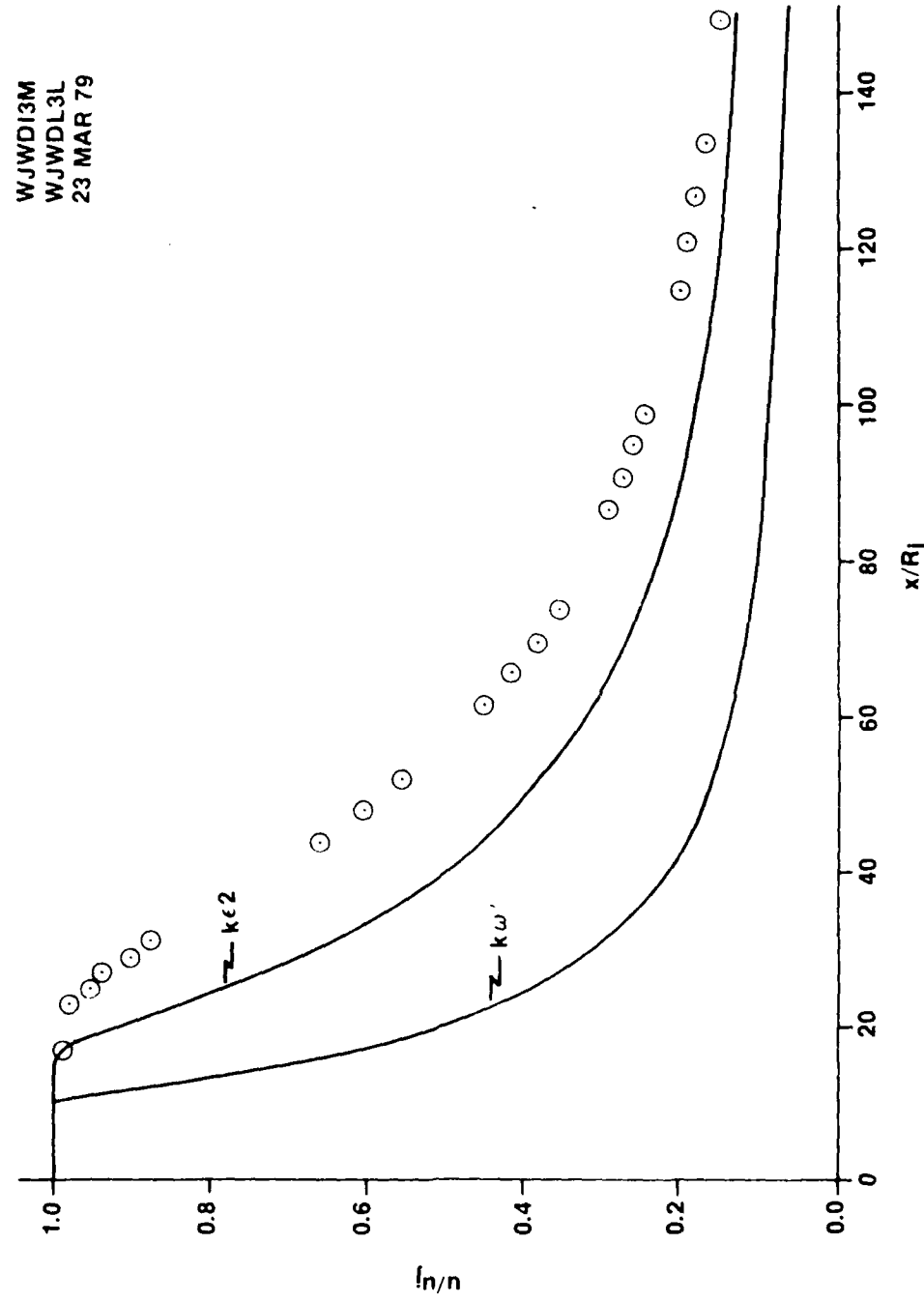


Figure 20. $M_j = 2.2$ air jet into still air. Comparison of $k_{\epsilon 2}$ and k_{ω} turbulence models without compressibility centerline velocity profile.

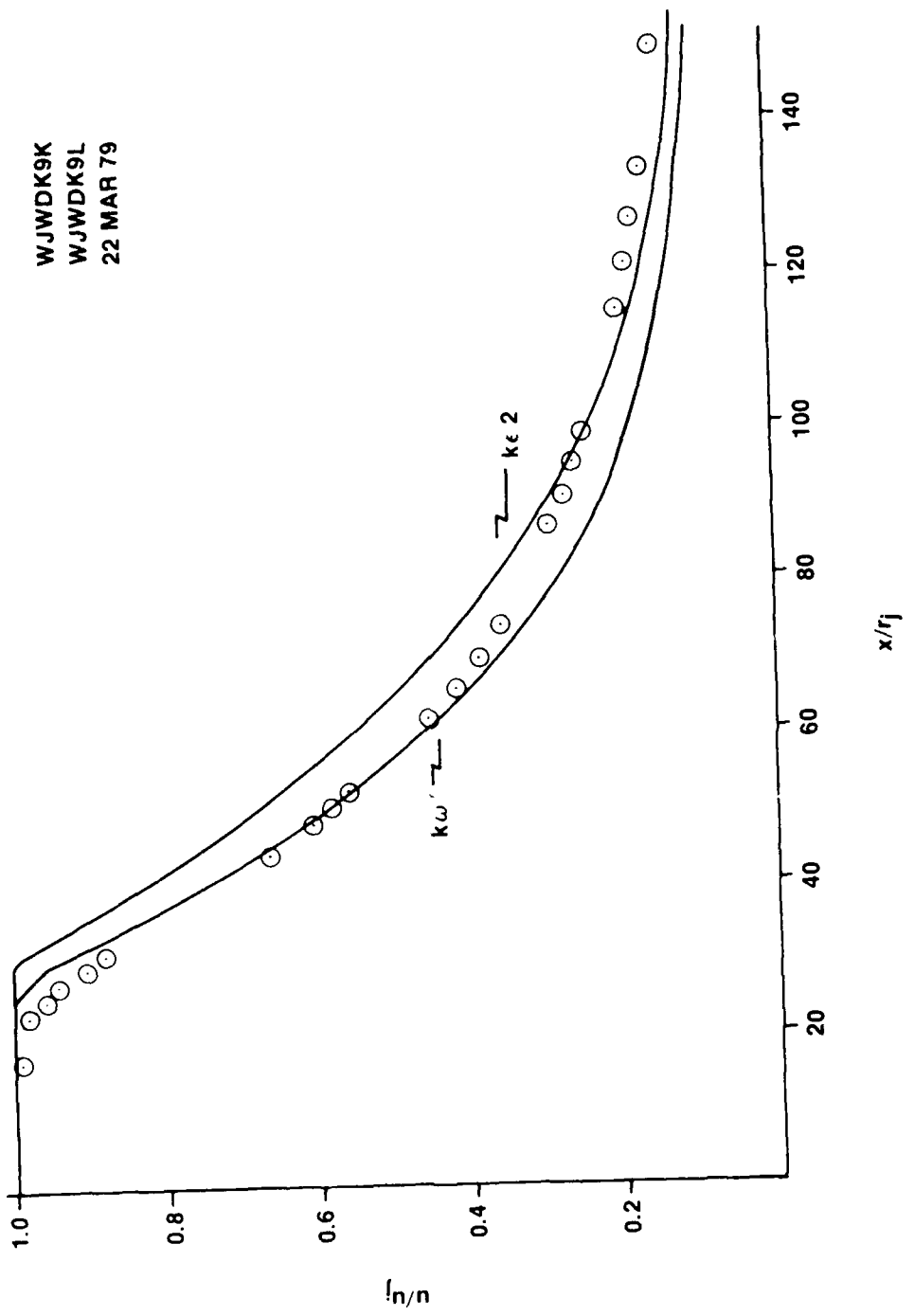


Figure 21. $M_j = 2.2$ air jet into still air. Comparison of $k_{\epsilon} 2$ and k_{ω} turbulence models with compressibility centerline velocity profile.

value. Hence, both models agree reasonably well with the experimental data with the $k\omega'$ model showing the better agreement of the two. Further, it has been established that the compressibility effects are important and will be retained for the remainder of the jet comparisons in this section.

The next test of the model predictive capability comes about by comparing the radial velocity profiles at downstream axial stations. The first station chosen was near the end of the jet potential core as shown in *Figure 20* at 22.9 jet radii downstream of the nozzle exit. Note that the velocity profile in *Figure 22* shows a small diameter potential core at this distance downstream and a gradual velocity reduction as the radial distance increases. Note that both turbulence models show excellent agreement with the experimental data with the $k\omega'$ model showing slightly better agreement.

The next point chosen for comparison was at 43.9 nozzle radii downstream. The radial profile at this axial station is shown in *Figure 23*. The agreement between the $k\omega'$ model and experiment is near perfect at this axial location. The $k\epsilon 2$ model prediction shows a reduced velocity compared with experiment indicating that mixing is occurring slightly too rapidly.

The last point chosen for comparison was at 61.7 nozzle radii downstream. The radial profile at this axial station is shown in *Figure 24*. The agreement between the $k\omega'$ model and experiment is very good at this axial location. The $k\epsilon 2$ model prediction again shows a reduced velocity compared with experiment.

It is thus concluded that compressibility effects are important for Case 1 (*Table 7*) and must be accounted for to achieve a reasonable agreement between theory and experiment. It is also concluded that the $k\omega'$ turbulence model shows improved agreement with the experimental data compared with the $k\epsilon 2$ model.

The second comparison made was for a $M_j = 0.89$ H_2 jet into a supersonic $M_\infty = 1.32$ air jet. The jet velocity was 3520 ft/sec and the external velocity was 1295 ft/sec. The pressure was ambient and the initial density ratio is shown in *Table VII*.

Figure 22 compares model predictions for the $k\epsilon 2$ and $k\omega'$ turbulence models with compressibility. It should be noted that the agreement between theory and experiment for the core length is reasonable. The $k\omega'$ model shows a slightly better agreement with the experimentally determined length.

The radial velocity profiles were first compared at an axial distance downstream of 11.02 nozzle radii. This can be seen from *Figure 25* to still be in the potential core region. Note in *Figure 26* that the predicted radial profile utilizing the $k\omega'$ model is reasonable but certainly does not agree as closely as it did in Case 1 above. Discrepancies between experiment and theory became apparent when the velocity difference ratio has dropped to approximately 60

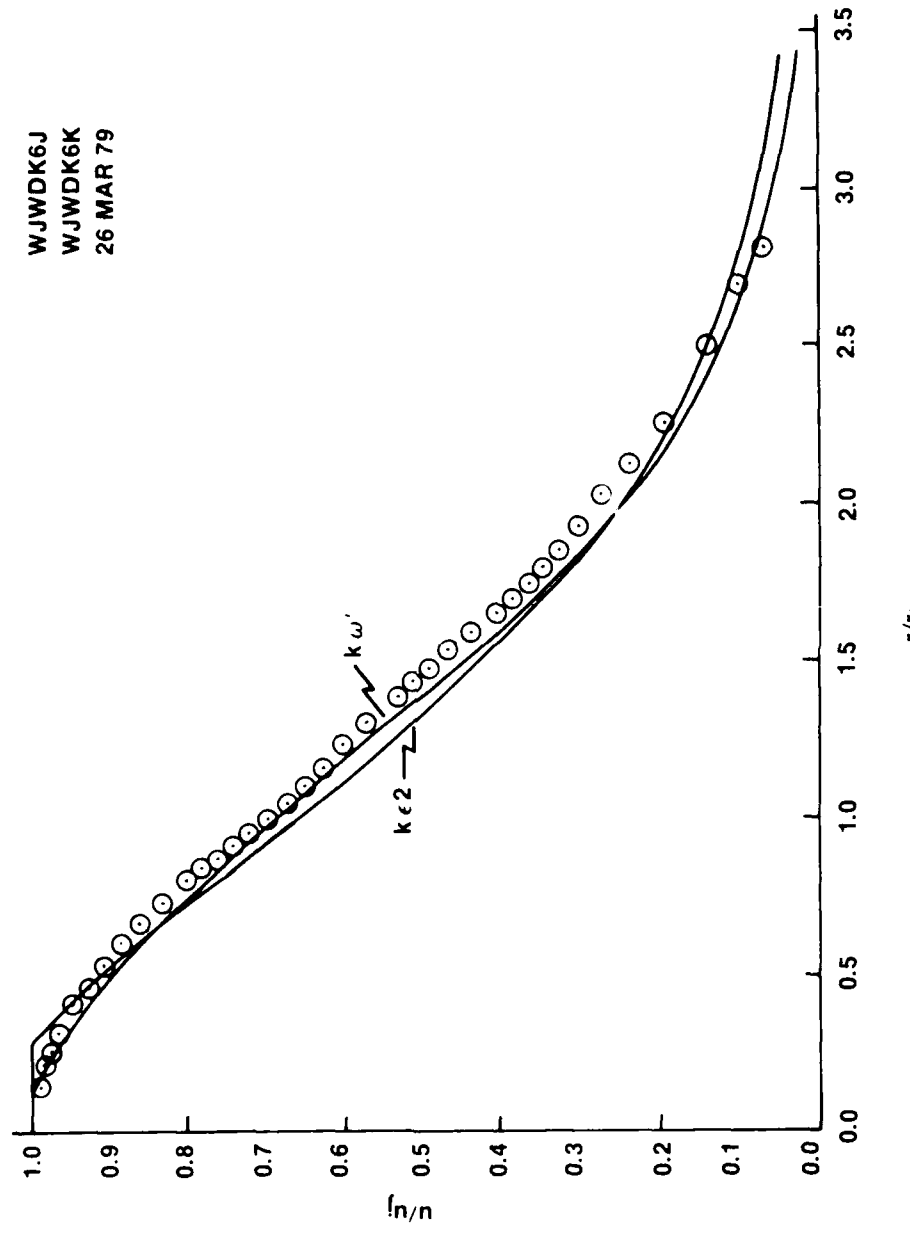


Figure 22. $M_j = 2.2$ air jet into still air. Comparison of k_{ϵ^2} and $k_{\omega'}$ turbulence models with compressibility radial profile at $x/r_j = 22.9$.

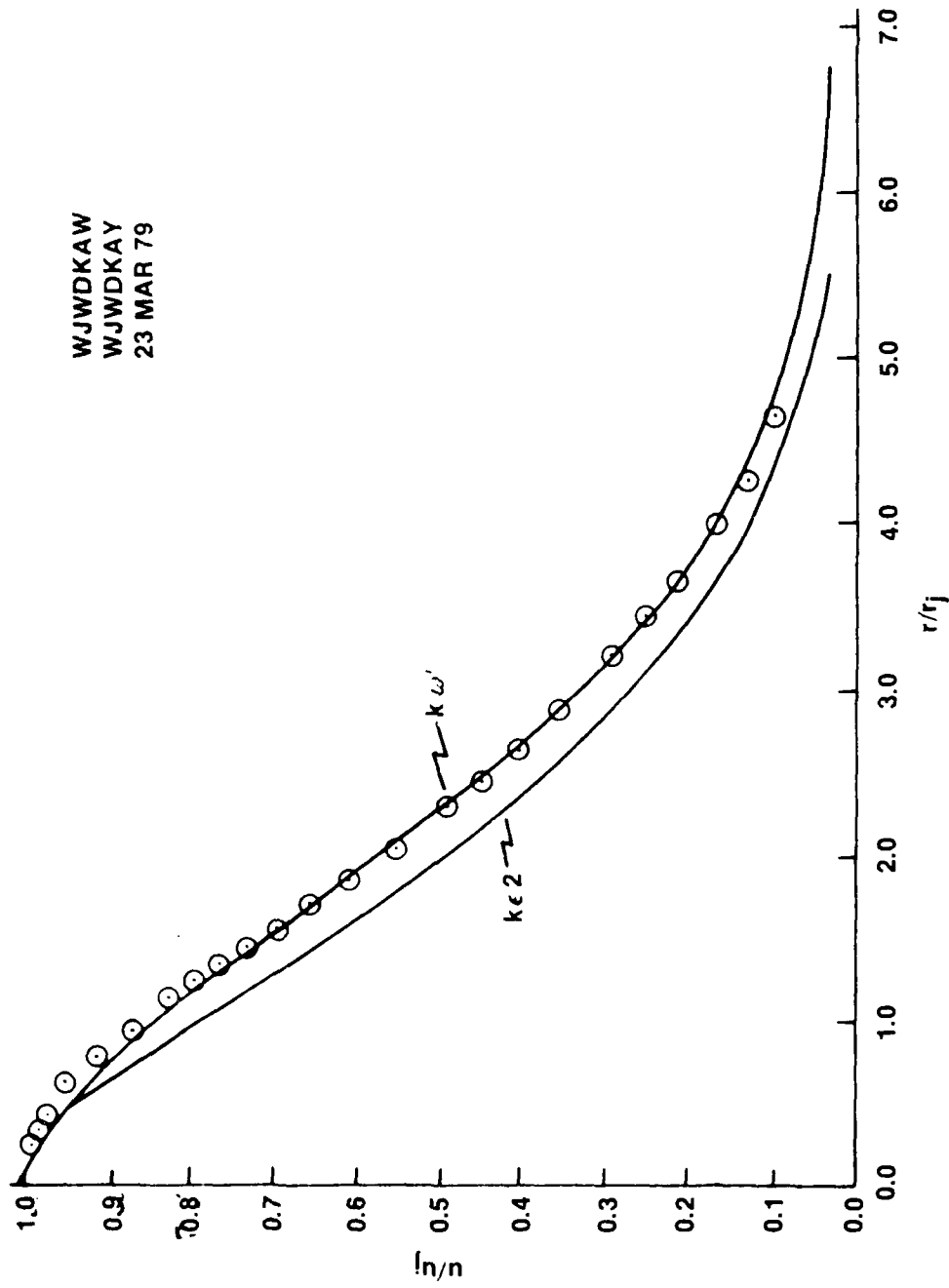


Figure 23. $M_j = 2.2$ air jet into still air. Comparison of $k \epsilon^2$ and $k \omega'$ turbulence models with compressibility radial profile at $x/r_j = 43.9$.

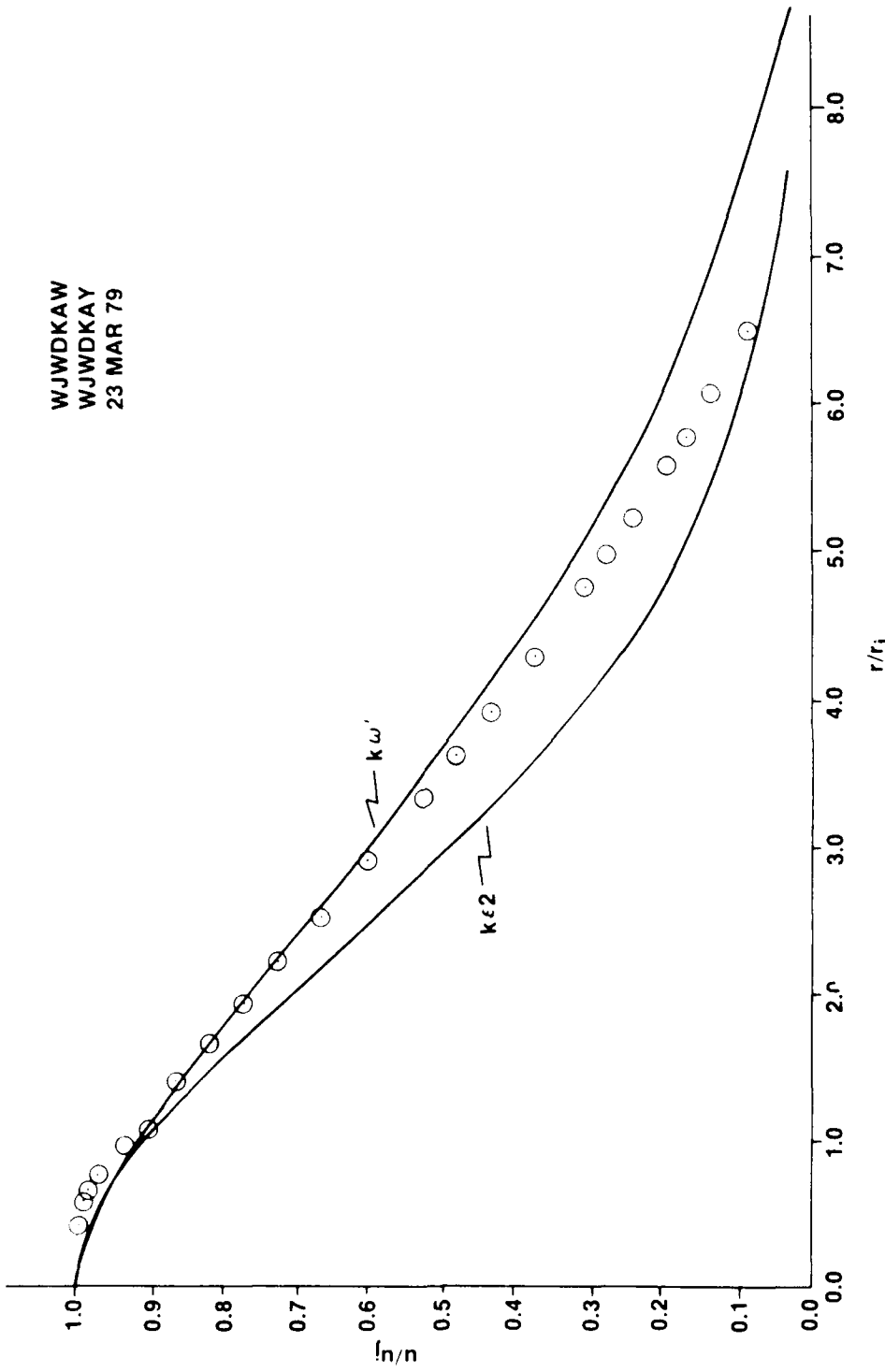


Figure 24. $M_j = 2.2$ air jet into still air. Comparison of $k\epsilon_2$ and $k\omega'$ turbulence models with compressibility radial profile at $x/r_j = 61.7$.

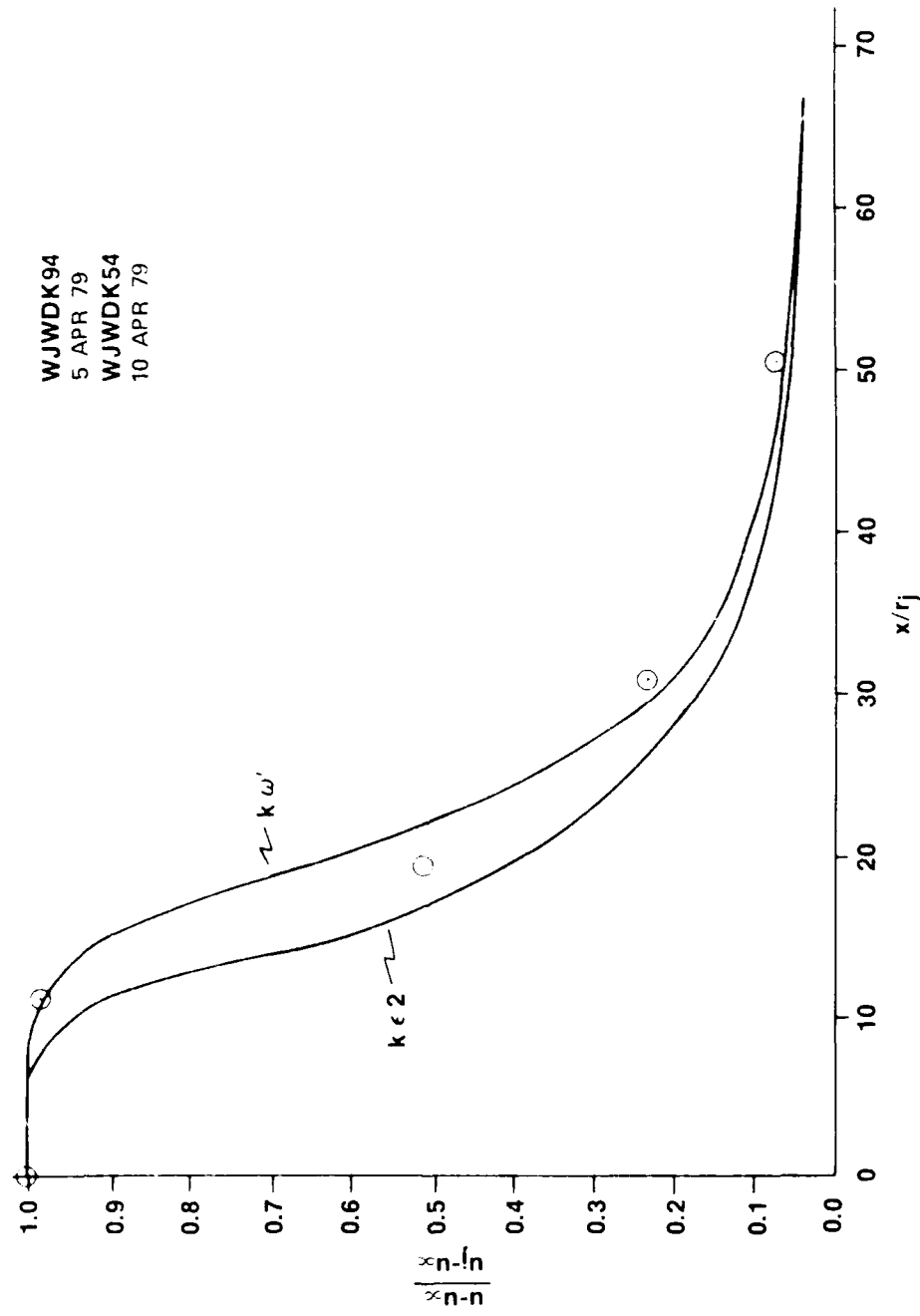


Figure 25. $M_j = 0.89$ H₂ jet into $M_\infty = 1.32$ air. Comparison of $k-2$ and k_ω turbulence models with compressibility centerline velocity profile.

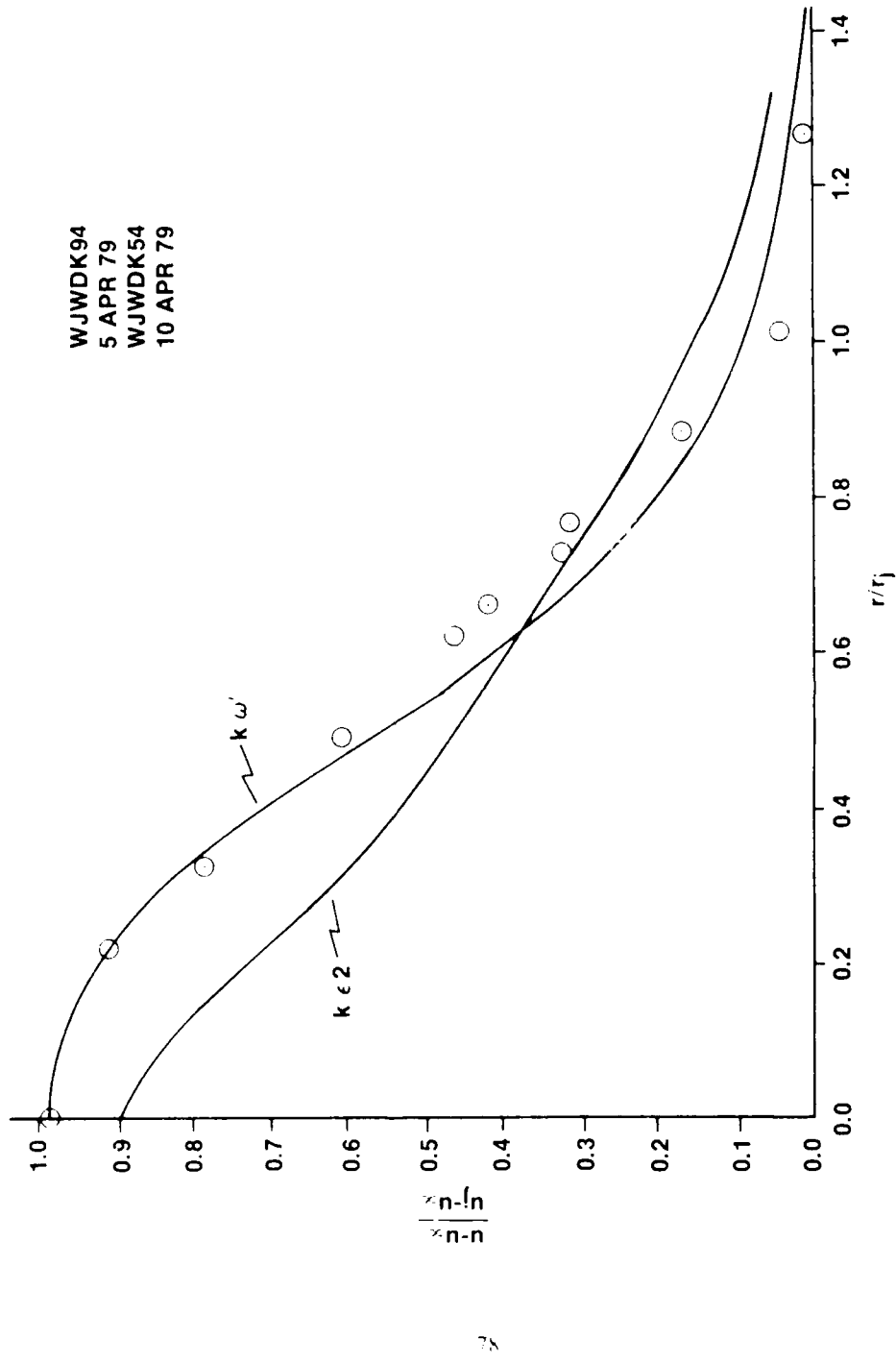
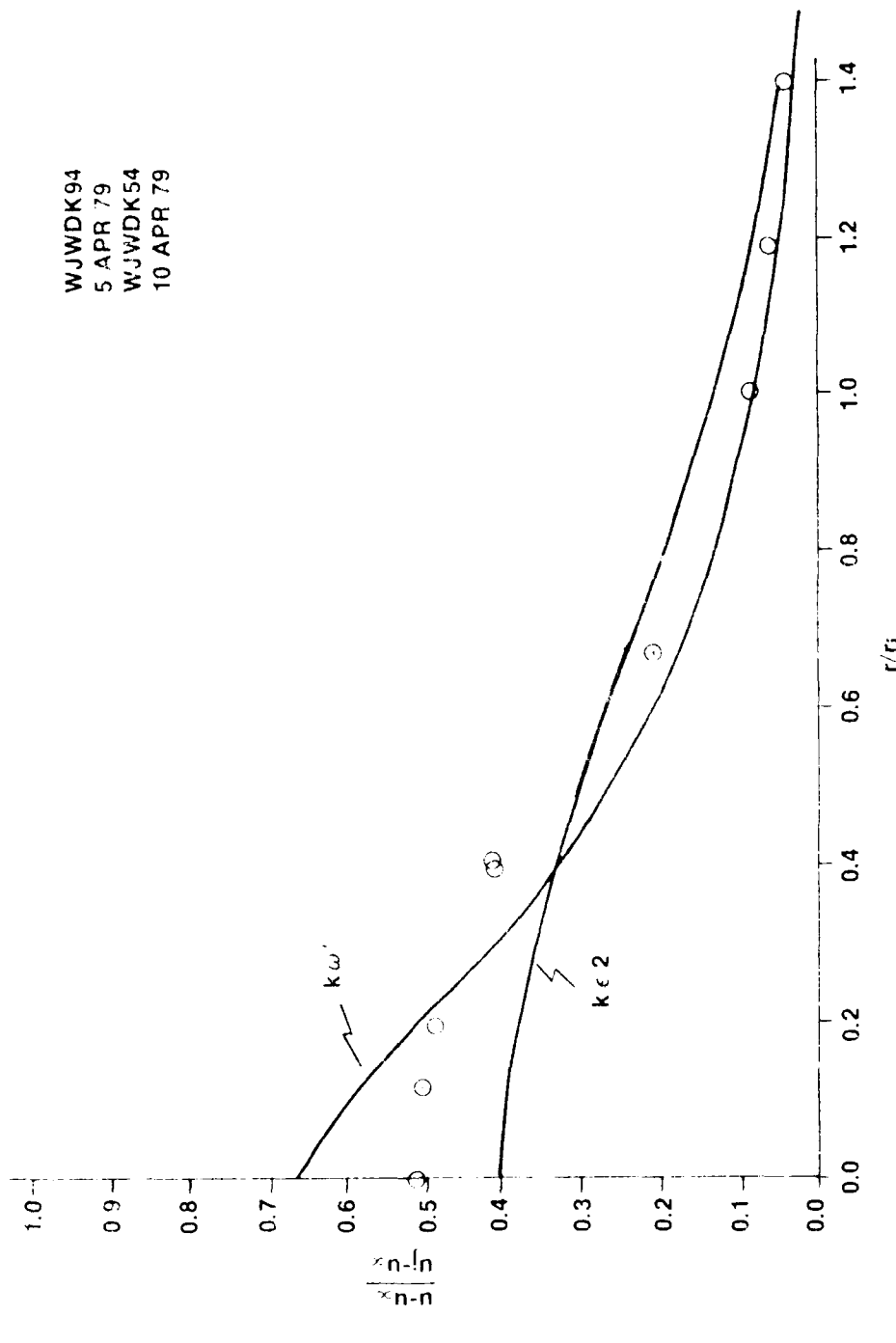


Figure 26. $M_j = 0.89$ H₂ jet into $M_{\infty} = 1.32$ air. Comparison of k_2 and $k_{\omega'}$ turbulence models with compressibility radial profile at $x/r_j = 11.02$.



$M_j = 0.89$ H_2 jet into $M_\infty = 1.32$ air. Comparison of $k_{\epsilon 2}$ and $k_{\omega'}$ turbulence models with compressibility radial profile at $x/r_j = 19.16$.

percent of its initial value. Use of the $k\epsilon 2$ model gives a noticeably poorer agreement with experiment over the entire range of comparison.

The next radial profile to be compared is shown in *Figure 27* at a downstream distance of 19.16 nozzle radii. Note that the comparisons do not agree at the $r = 0$ point because the core length is incorrectly predicted by both turbulence models. Both models do equally well over the entire range of parameters at this downstream distance with the most serious discrepancies occurring at $r = 0$.

The last radial profile comparison was made at a distance of 30.88 nozzle radii downstream of the exit plane as shown in *Figure 28*. Both models do reasonably well over the radius range covered with the largest discrepancy occurring at the lower values of the radius ratio.

The preceding comparisons demonstrate that the turbulence kinetic energy methods predict the velocity profiles, both radially and axially, reasonably well over a fairly wide range of velocities and densities. "Reasonably well" means an accuracy within ≈ 30 percent for a maximum error. They also demonstrate that compressibility effects are important and must be accounted for in the modeling in order to achieve this accuracy. Otherwise, even larger errors will occur.

These comparisons also demonstrate that the $k\omega'$ turbulence model show closer agreement to experiment than the $k\epsilon 2$ model over the range of comparisons made. Hence this model can be considered as a viable alternative to the $k\epsilon 2$ model.

VII. REACTING SHEAR LAYER COMPARISON

Thus far the turbulent mixing models have been compared against flows which have different velocities for each of the two streams or different velocities and different densities. The latter type flow is certainly more applicable to the rocket exhaust plume flows since large density ratios occur for these cases and since it is important to know the species distribution across the mixing layer. The next level of complexity in the modeling procedure is to examine the turbulent mixing of a reacting shear layer, preferably one in which the initial densities of the two streams are the same. This eliminates another variable in the problem if the initial density ratio can be held at unity. In addition, a kinetically simple reacting flow system is mandatory for an accurate test of the turbulence models since chemical reaction rates constantly change.

Reacting shear layer experiments of this kind have recently been completed at the University of Adelaide in Australia and have been reported at the Second Symposium on Turbulent Shear Flows by Wallace and Brown [5].

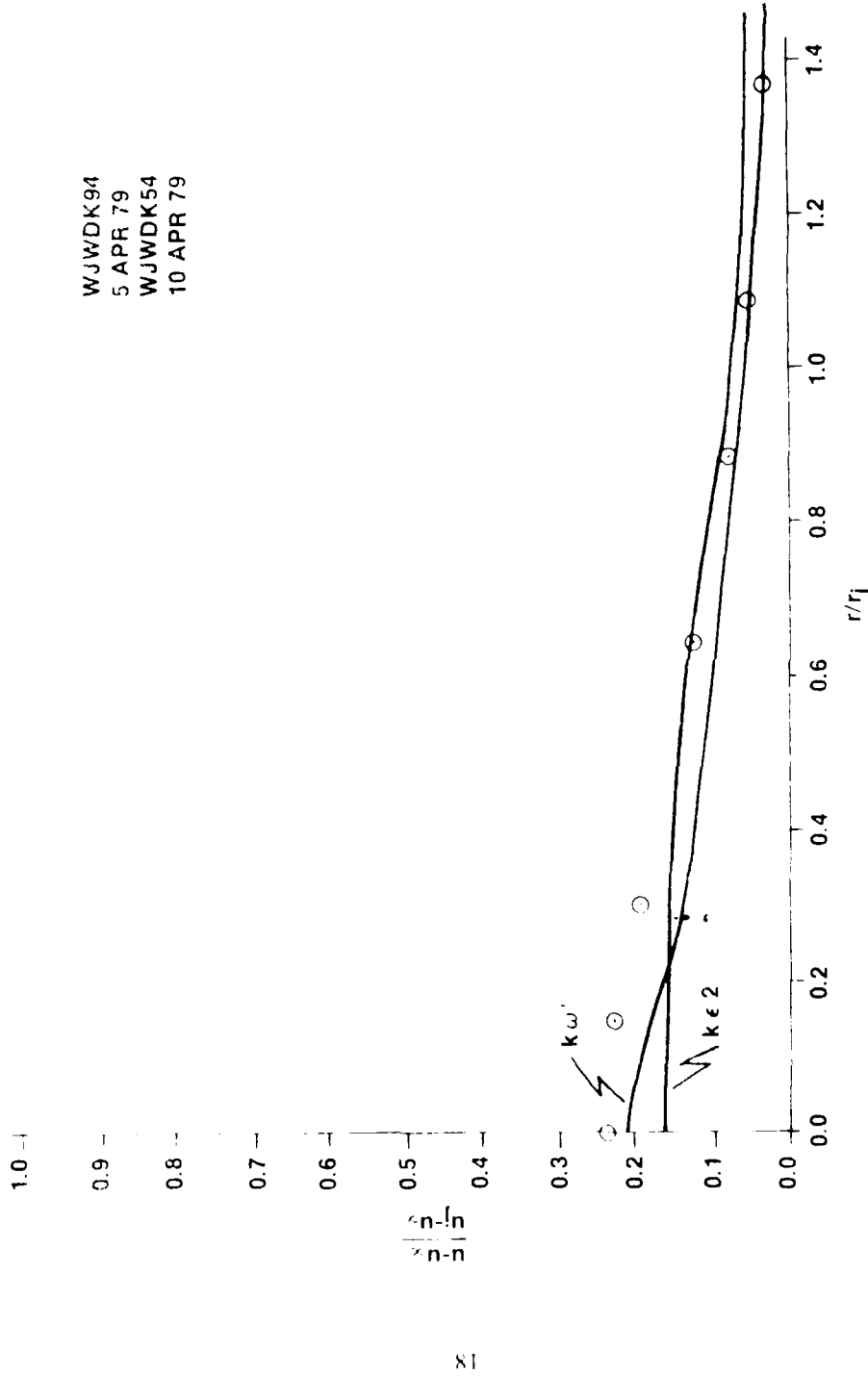


Figure 28. $M_j = 0.89$ H₂ jet into $M_\infty = 1.32$ air. Comparison of $k \epsilon^2$ and $k \omega'$ turbulence models with compressibility radial profile at $x/r_j = 30.88$.

In these experiments, the jet stream consisted of NO mixed with N₂ in various low level concentrations and the external stream consisted of O₃ mixed with N₂ in various other low level concentrations. The jet stream velocity was 82 feet/second and the external stream velocity was 16 feet/second. The flow channel was 3.94 inches wide and the height of the jet stream nozzle was 0.98 inches while the height of the external stream nozzle was 1.97 inches. The Re number based on the boundary layer height was ≈ 100 .

The chemical reaction involved in this experiment is very simple



This is a well known chemical reaction and its rate is known with a high degree of accuracy as long as the temperature remains below 500 degrees K. Therefore, this experiment allows the comparison of the turbulent mixing model directly since the chemical kinetics of this reaction are so well known.

Comparisons were made for three two-dimensional reacting shear layer cases shown in *Figure 29* and further details in *Table 8*.

Note in *Figure 29* that the jet stream contains the fuel NO and the external stream contains the oxidizer O₃. The low concentrations of fuel and oxidizer mixed with the carrier

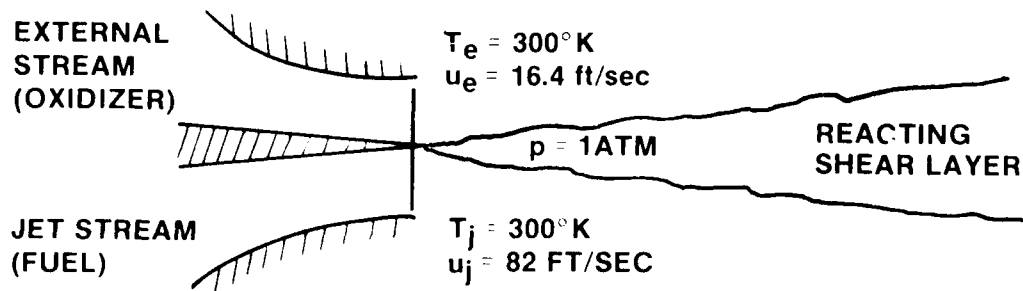


Figure 29. Two-dimensional reacting shear flow schematic.

TABLE 8. INITIAL CONDITIONS FOR REACTIVE SHEAR LAYER COMPARISONS

CASE NO.	u_j/u_e	p_j/p_e	T_j/T_e	JET STREAM CONSTITUENT*		EXTERNAL STREAM CONSTITUENT*	
				NO	N_2	O_3	N_2
I	5.0	0.996	1.0	0.05	0.95	0.010	0.990
II	5.0	0.977	1.0	0.05	0.95	0.0379	0.9621
III	5.0	0.95	1.0	0.05	0.95	0.078	0.922

* Constituents given as mole fractions.

stream, N_2 , is detailed in *Table 8* for the cases that were compared. The reason for such low concentrations of reactants is the degree of reactivity of the $NO + O_3$ reaction. A large amount of heat is produced from minute quantities of reactants.

Comparisons were made for the cases shown in *Table 8* where the amount of oxidizer in the external stream was constantly increased from 1 to 7.8 percent. This increased the O_3/F ratio and resulted in increasingly higher shear layer temperatures. Comparisons were made of both the velocity and temperature profiles for these cases. Density profiles were not measured.

The virtual origin x_v was not determined in these tests as it was for the non-reacting shear layer experiments presented earlier. Hence, for the theoretical predictions, x_v was taken as zero indicating that the shear layer starts growing exactly at the exit plane of the nozzle. This will produce some error by scaling the width of the predicted shear layer incorrectly. Hence, even if the theoretical and experimental results agreed perfectly, the width of the shear layer would show a discrepancy between the predicted and measured results. However, this is not considered to be a serious discrepancy in light of the magnitude of the disagreement of the temperature profiles as will be subsequently shown.

Both the $k\epsilon^2$ turbulence model and the $k\omega'$ turbulence models were utilized in the predictions of the reacting shear layers. These models produced virtually identical results and therefore the predictions shown were those obtained utilizing the $k\omega'$ turbulence model.

Results comparing the reacting shear layer for Case I given in *Table 8* predicted and measured are shown in *Figure 30*. This is a comparison of the velocity profile across the shear layer. The agreement between theory and experiment is excellent. This agreement compares favorably with the non-reacting shear layer results presented earlier for the case where the initial density ratio is 1. That is the situation here. The density ratio is 0.996 initially as shown in *Table 8*. Therefore it appears that the velocity profile is little affected by the reacting flow at least at this level and similarly good agreement between experiment and theory is shown.

Figure 31 compares the temperature profile predicted across the reacting shear layer with that actually measured. In contrast to the excellent agreement between the velocity profile determined from experiment and theory, these results are quite the opposite. The predicted temperature rise profile across the shear layer looks nothing like the measured profile. The predicted maximum temperature rise is more than twice what was actually measured. Likewise the predicted temperature gradient is much larger than that found experimentally. The shear layer width also does not agree but as was mentioned previously, this is scaled by the virtual origin x_0 and therefore cannot agree unless the origin of the shear layer lies at the exit plane of the two flows. In addition, it is worth noting that the location of the predicted maximum temperature rise from the dividing streamline is displaced toward the jet (fuel stream) side relative to the experimental results.

The results shown for both *Figures 30* and *31* were for an axial distance of 100 mm downstream of the shear layer exit plane.

For the 3.79 percent (mole) O_2 case given as Case II in *Table 8*, no experimental results were available with which to make a comparison of the velocity profile across the shear layer. Hence the temperature profile is compared again at 100 mm downstream of the shear layer exit plane. This comparison is shown in *Figure 32*. Note that the essential features that were discussed for the 1 percent O_2 case shown in *Figure 31* are applicable here as well. The predicted maximum temperature rise is more than twice the measured value. The location of the maximum is again shifted toward the jet stream side and the width of the shear layer is in disagreement.

A Lewis number variation was made to determine its effect on the width of the temperature shear layer compared with the velocity shear layer but only minor variations resulted. This did not affect the overall poor comparison between theory and experiment.

The next case compared is shown as Case Number III in *Table 8*. The O_2 mole fraction was increased to 7.8 percent for this comparison. The velocity profile is compared in *Figure 33*. Note that the agreement, while not as good as for the 1 percent O_2 case, is again excellent. This

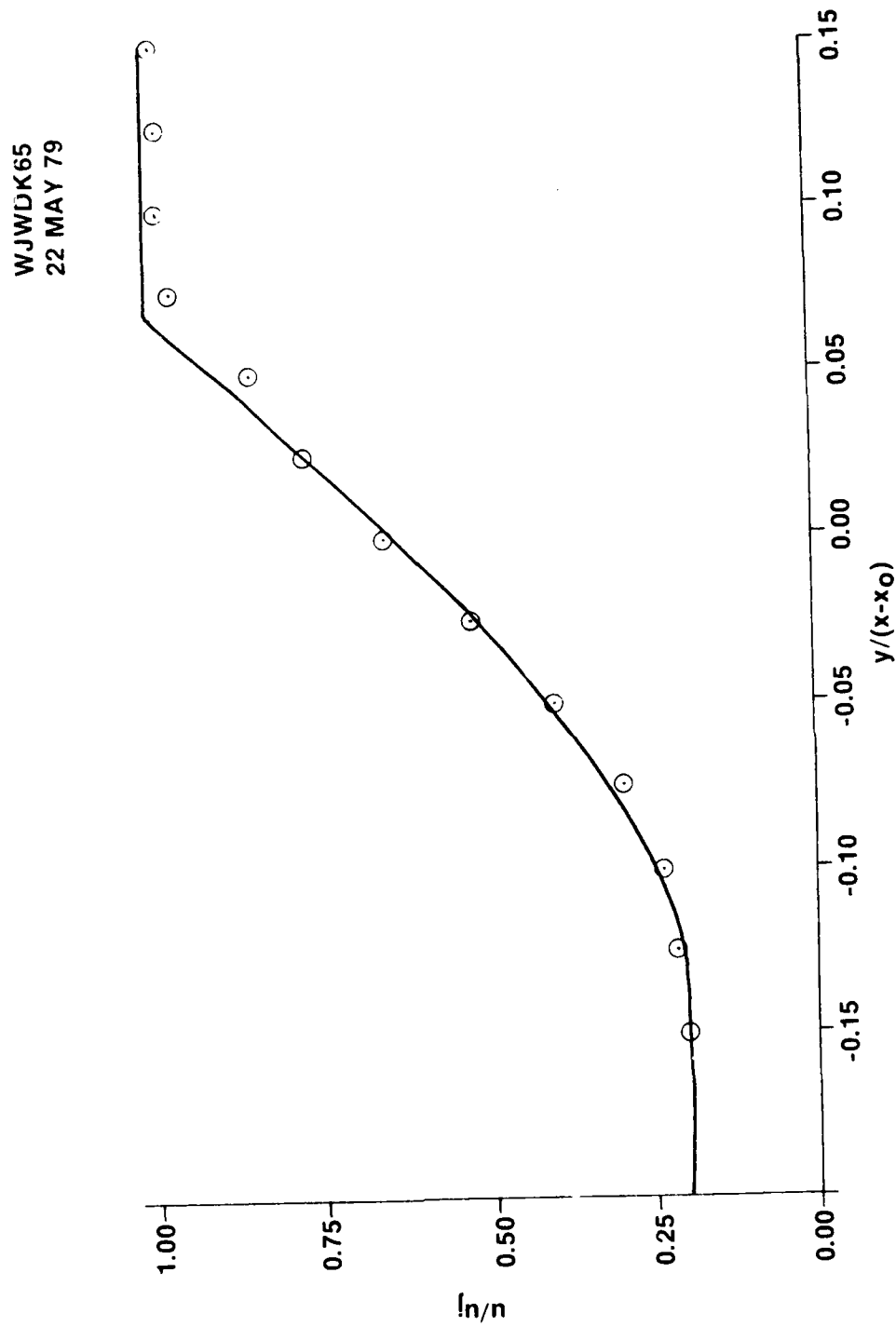


Figure 30. Velocity profile comparison for reacting shear layer - Table 8,
 case number 1.

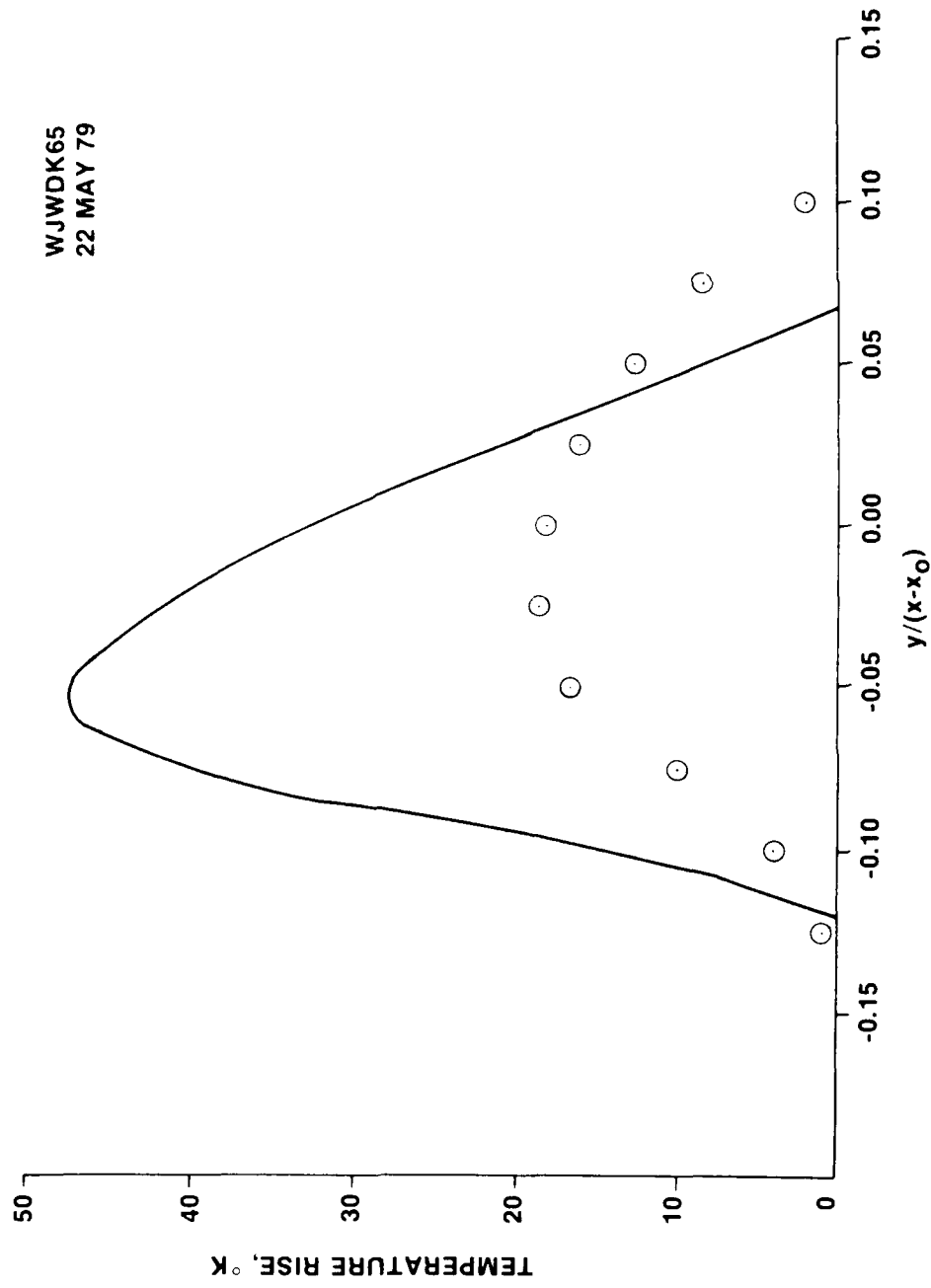


Figure 31. Temperature profile comparison for reacting shear layer -
Table 8, case number 1.

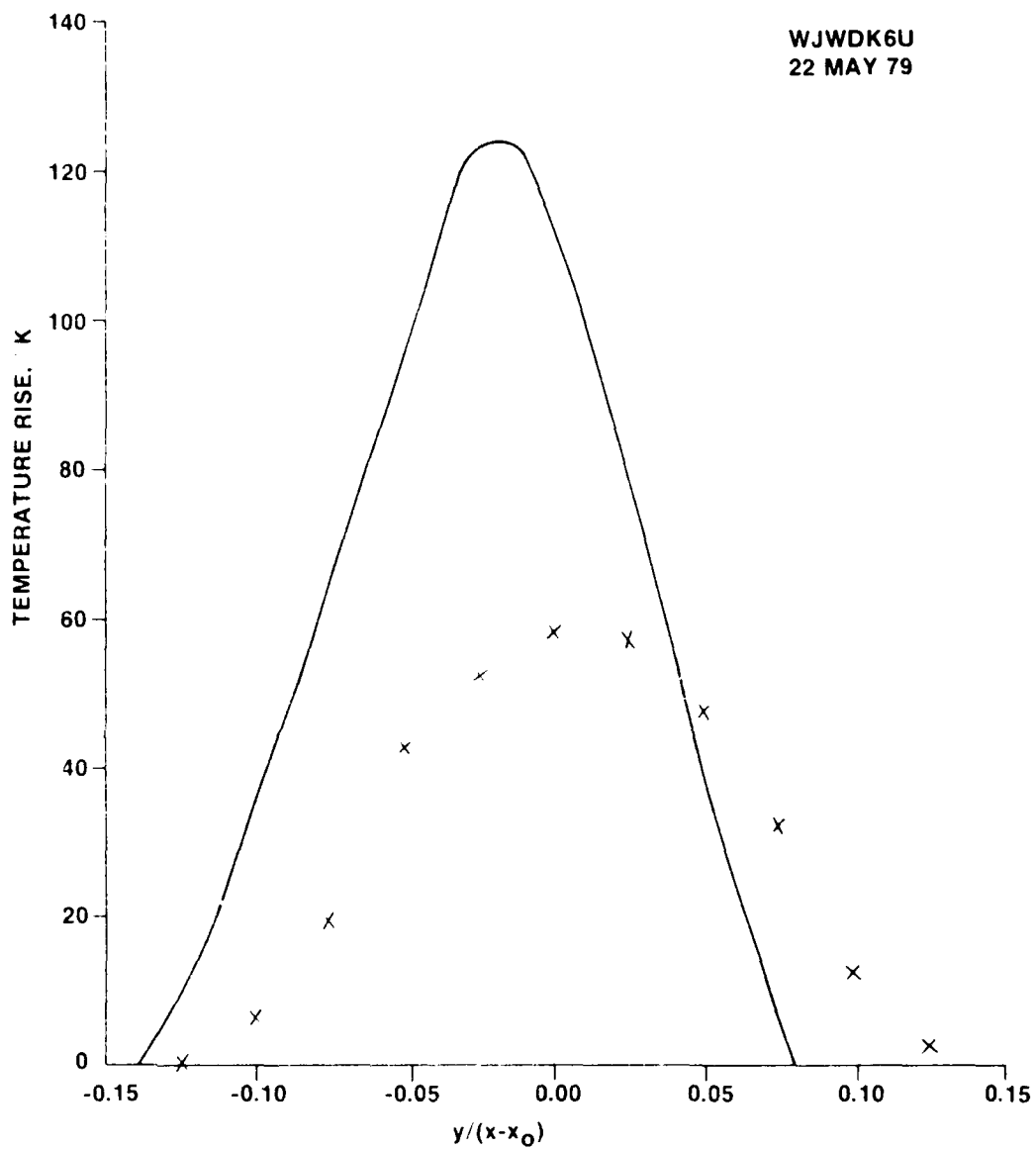


Figure 32. Temperature profile comparison for reacting shear layer -
Table 8, case number II.

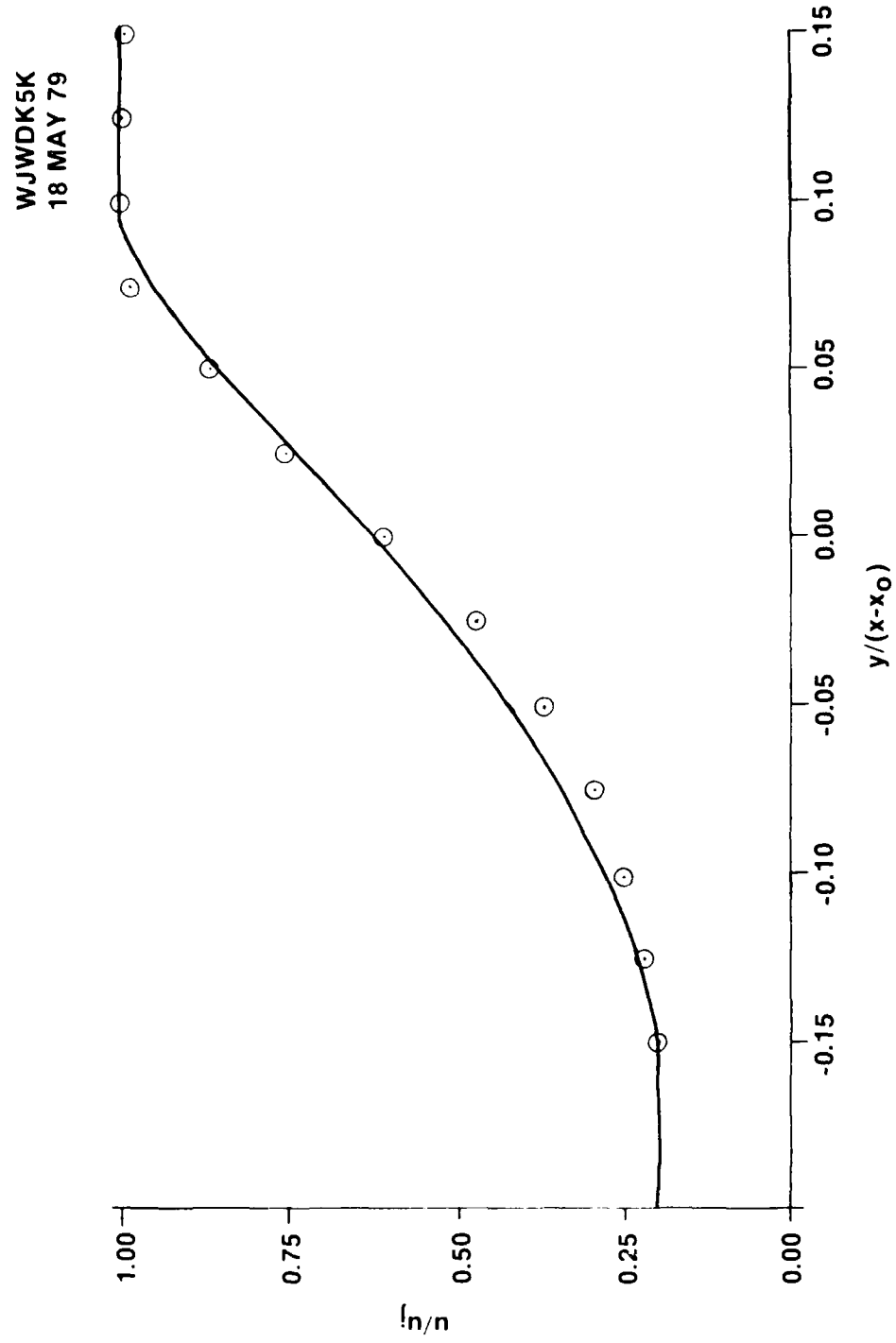


Figure 33. Velocity profile comparison for reacting shear layer -
Table 8, case number III.

should be expected however in light of the results presented in *Figure 29*. Again this is a nearly constant initial density case, the density ratio being 0.95 as given in *Table 8*.

Figure 34 illustrates the comparison of the predicted and measured temperature profile across the reacting shear layer. Similarly for this case the predicted maximum temperature rise is nearly twice the measured value. The predicted maximum is similarly skewed to the jet stream side. Hence the common features that were noted in Cases I & II (*Table 8*), are similarly evident in Case III.

It is instructive to examine the results for an increasing amount of oxidizer and noting the shift toward the fuel side. This is shown in *Figure 35* where the maximum temperature rise location moves toward the oxidizer stream monotonically with increasing oxidizer. This leads one to suspect that the turbulence model utilized in the predictions is behaving in a "laminar manner". Note that the experimental results show very little shift in the maximum temperature rise.

This hypothesis was confirmed after programming a laminar mixing model and introducing it as an option into the BOAT analysis. This was accomplished [8] and the results are shown in *Figure 36*. Note that the laminar mixing case results in virtually the same maximum temperature rise as for the $k\omega'$ turbulence model. The only difference is the spreading rate of the laminar shear layer compared to the turbulent shear layer.

Finally predictions were made with two other turbulence models; (i) Prandtl mixing length model and (ii) Donaldson-Gray eddy viscosity model. The results are shown in *Figures 37* and *38*, respectively. It is evident from these figures that neither of the simple models offers any hope of better agreement between experiment and theory.

VIII. CONCLUSIONS

Results of this study clearly show that matching of a theoretical velocity profile for mean velocities with experimental results is not a good indicator of the correctness of a turbulence model. This was shown most vividly for the reacting shear layer experiments where the velocity profile match was excellent and the temperature profile through the shear layer was in error by more than a factor of two. The velocity profile was the easiest parameter to match when utilizing the turbulence kinetic energy models given in this investigation. The constant initial density cases showed excellent agreement between experiment and theory for

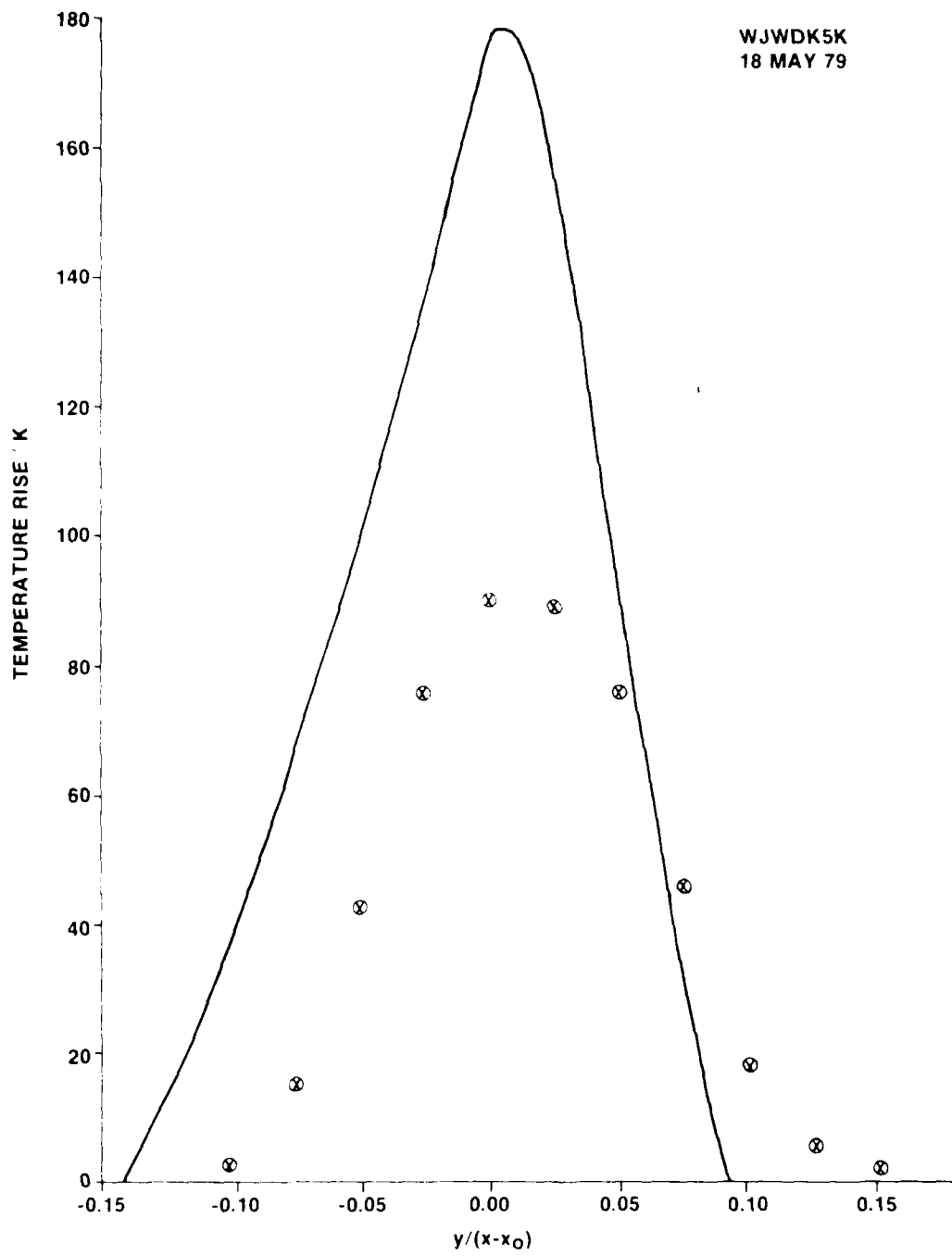


Figure 34. Temperature profile comparison for reacting shear layer -
Table 8, case number III.

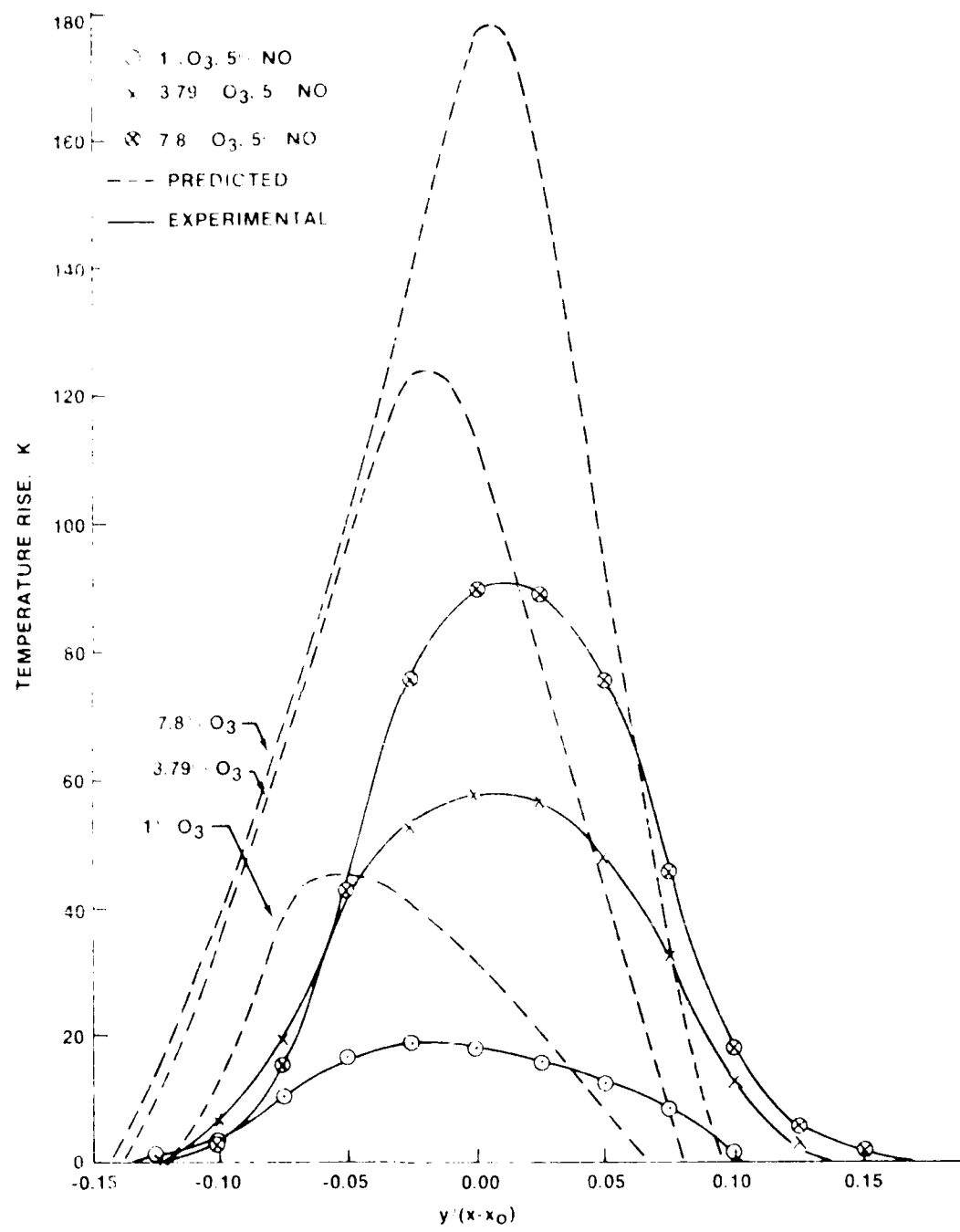


Figure 35. Measured and predicted temperature distribution in shear layers between nitric oxide and ozone.

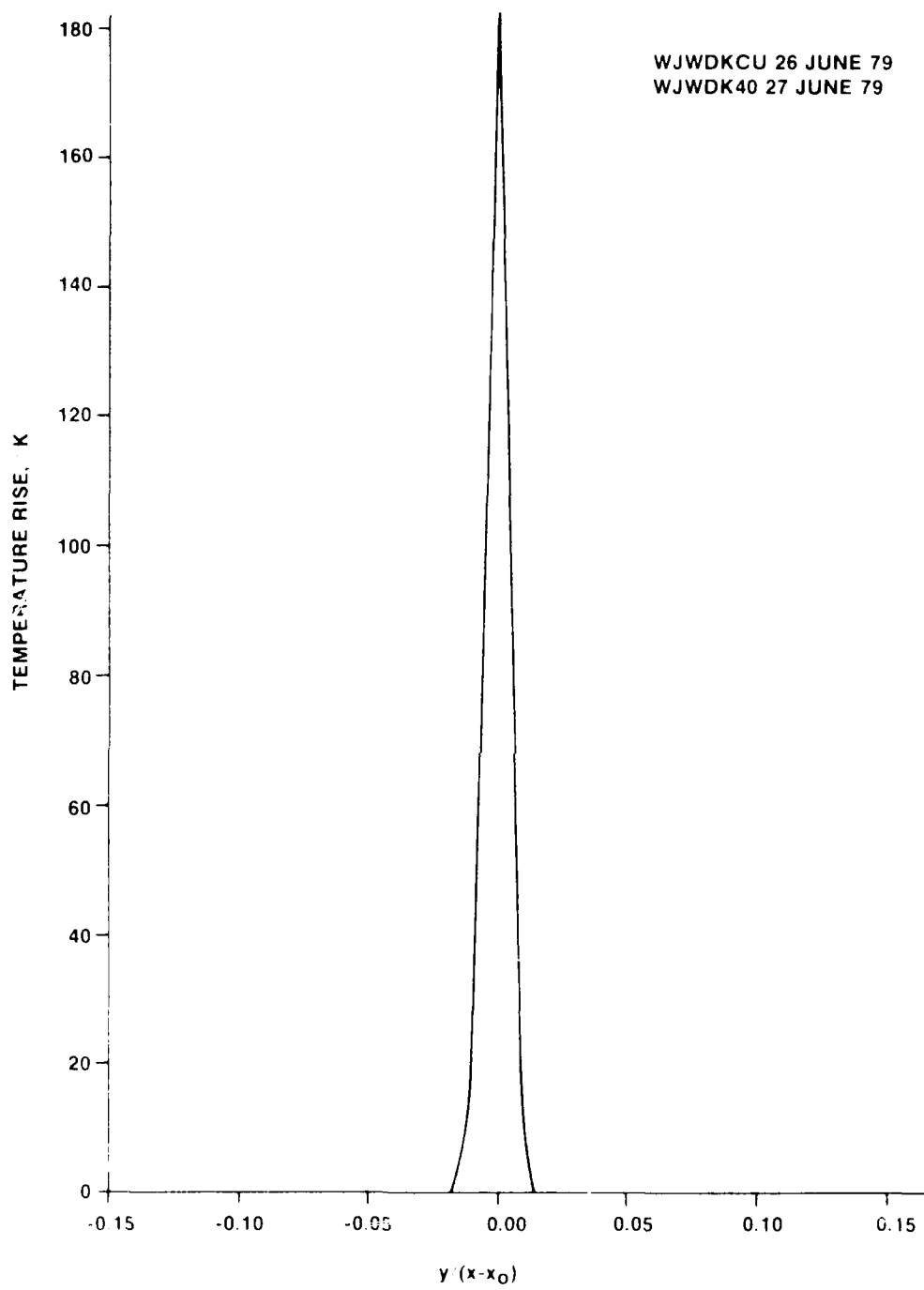


Figure 36. Temperature profile prediction for reacting shear layer using laminar viscosity model - Table 8, case number III.

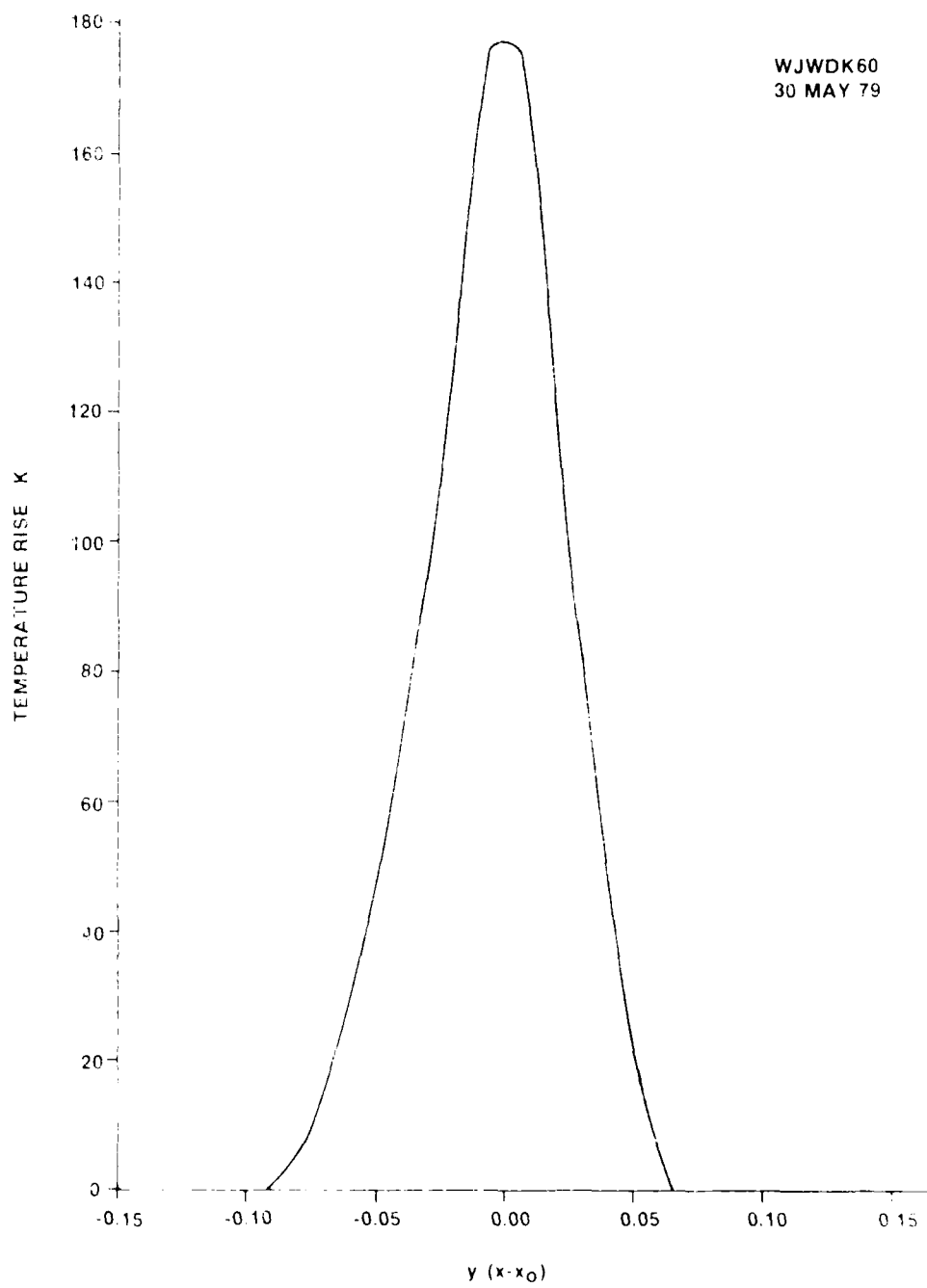


Figure 37. Temperature profile prediction for reacting shear layer using Prandtl mixing length turbulence model, Table 8 (1980), number III.

AD-A094 438

ARMY MISSILE COMMAND REDSTONE ARSENAL AL SYSTEMS SI--ETC F/0 12/1
TURBULENCE MODEL COMPARISONS FOR SHEAR LAYERS AND AXISYMMETRIC --ETC(U)
OCT 79 B J WALKER
UNCLASSIFIED DRSMI/RD-80-1-TR

SBIE-AD-E950 074

NL

2 cr 2
ACI
22-92146

END
DATE
FILED
2-81
DTIC

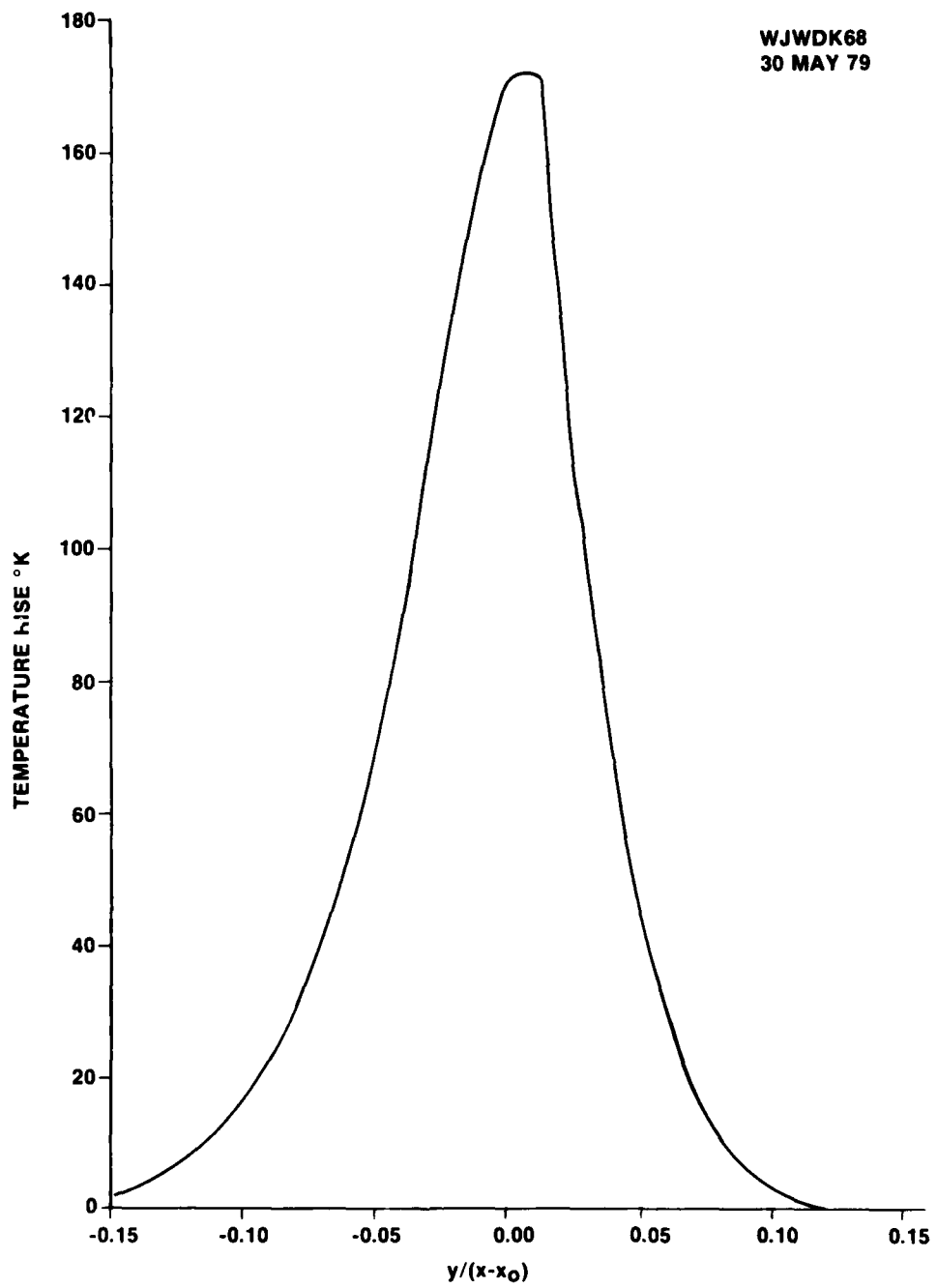


Figure 38. Temperature profile prediction for reacting shear layer using Donaldson-Gray eddy viscosity, turbulence model - Table 8, case number III.

all cases investigated. This was not true, however, for the case where the initial density ratios were significantly greater than one (≈ 7).

The density profiles across the shear layer were very poorly predicted for all cases examined in this investigation. This was especially true for the case when the high velocity jet fluid was simultaneously the low density fluid in the two-dimensional shear. This is a case that more nearly corresponds to the rocket exhaust plume.

The $k\omega'$ turbulence model gives comparable results with the $k\epsilon 2$ turbulence model. In all cases examined the $k\omega'$ model performed as well as the $k\epsilon 2$ model and in certain instances, it performed much better than the $k\epsilon 2$ model. This was especially true for the $M=2.2$ air jet exhausting into still air.

The temperature profiles that are predicted by the turbulence models are extremely poor. The temperatures are too high by approximately a factor of two. This indicates that there is a significant large structure in the flows examined. The turbulence models do not account for this structure in any way and hence are all deficient in the basic physics of the flow. *Figure 39* details the structure of a typical non-reacting shear layer and Wallace and Brown [5] have shown similar behavior for the reacting shear layer. Examination of this photograph makes it clear that the vortex structure must be included in the turbulence models in order to obtain reasonable predictions.

Just how much large structure exists in flows more typical of rocket exhaust plumes where the velocities are much higher is not known *a priori*. It is suspected that the large structure will be less evidenced. If this is true, then perhaps the current turbulence models will offer more hope for making reasonable predictions. However, this remains to be seen. Non-reactive flow tests will be run in the near future which will provide the basis for the reasonable assessment of this effect.

APPENDIX A

The comparison of the theory with the experimental data of Brown and Roshko [1] and Wallace and Brown [5] required that the position of the dividing streamline be known. In addition, this information is necessary when determining the amount of mass entrained by the jet or by the shear layer. This was accomplished in the prediction program by utilizing the subroutine DIVSL.

Consider the plane mixing layer shown in *Figure A1*. By taking an element of fluid whose bottom edge is parallel to the dividing streamline, a momentum balance along the fluid element parallel to the dividing streamline as shown in *Figure A2* gives the following

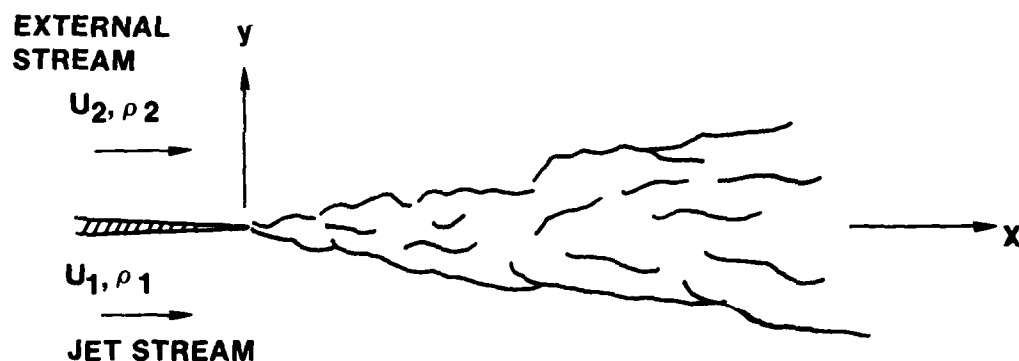


Figure A-1. Plane mixing layer.

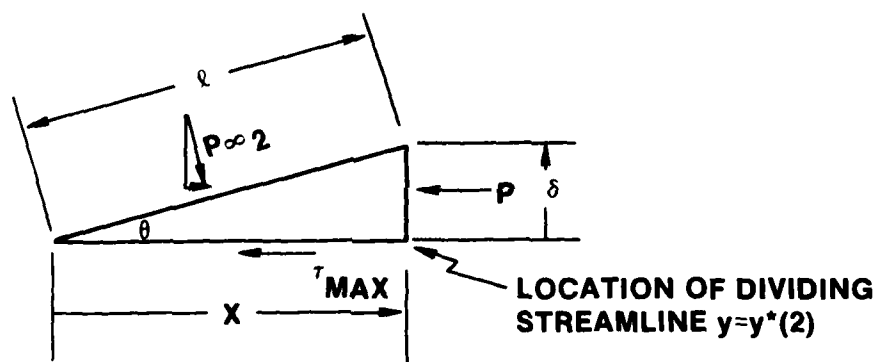


Figure A-2. Plane mixing layer fluid element (top half).

$$\begin{aligned}
 & -\tau_{\max} x + p_{\infty 2} \sin \theta \ell - \int_{y^*(x)}^{\delta(x)} p dy \\
 & = \int_{y^*(x)}^{\delta(x)} \rho u^2 dy + \int_{y^*(x)}^{\delta(x)} \rho u'^2 dy + U_{\infty 2}^2 \int_{y^*(x)}^{\delta(x)} \rho u dy
 \end{aligned} \tag{A1}$$

But

$$\ell \sin \theta = \delta$$

Hence

$$\begin{aligned}
 & -\tau_{\max} x + p_{\infty 2} \delta - \int_{y^*}^{\delta} p dy \\
 & = \int_{y^*}^{\delta} \rho u^2 dy + \int_{y^*}^{\delta} \rho \bar{u'^2} dy - U_{\infty 2}^2 \int_{y^*}^{\delta} \rho u dy
 \end{aligned} \tag{A2}$$

or rewriting

$$\begin{aligned}
 & -\tau_{\max} x + \int_{y^*}^{\delta} (p_{\infty 2} - p) dy \\
 & = \int_{y^*}^{\delta} \rho u^2 dy + \int_{y^*}^{\delta} \rho \bar{u'^2} dy - U_{\infty 2}^2 \int_{y^*}^{\delta} \rho u dy
 \end{aligned} \tag{A3}$$

But

$$p_{\infty 2} = p + \rho \bar{v'^2} \tag{A4}$$

Hence (A3) becomes

$$\begin{aligned}
 & -\tau_{\max} x + \int_{y^*}^{\delta} \rho \overline{v'^2} dy \\
 & = \int_{y^*}^{\delta} \rho u^2 dy + \int_{y^*}^{\delta} \rho \overline{u'^2} dy - U_{\infty 2}^2 \int_{y^*}^{\delta} \rho u dy
 \end{aligned} \tag{A5}$$

so that

$$\tau_{\max} x = \int_{y^*}^{\delta} (\rho \overline{v'^2} - \rho \overline{u'^2}) dy + \int_{y^*}^{\delta} \rho u (U_{\infty 2} - u) dy \tag{A6}$$

Similarly if we consider the bottom half of the fluid element shown in *Figure A3*

$$\begin{aligned}
 & \tau_{\max} x + p_{\infty 2} \delta - \int_{-\delta}^{y^*} p dy \\
 & = \int_{-\delta}^{y^*} \rho u^2 dy + \int_{-\delta}^{y^*} \rho \overline{u'^2} dy - U_{\infty 1} \int_{-\delta}^{y^*} \rho u dy
 \end{aligned} \tag{A7}$$

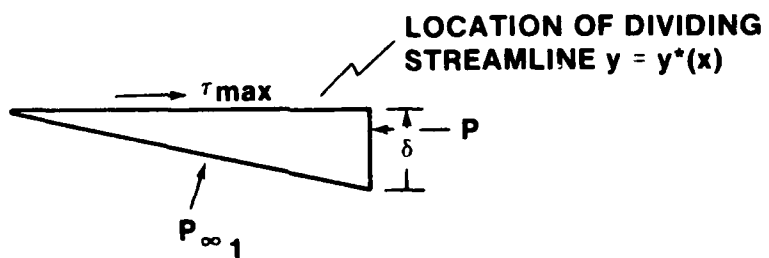


Figure A-3. Plane mixing layer fluid element (bottom half).

and since

$$p_{\infty 1} = p + \rho \overline{v'^2}$$

$$\tau_{\max} x + \int_{-\delta}^{y^*} \rho \overline{v'^2} dy = \int_{-\delta}^{y^*} \rho u (u - u_{\infty 1}) dy + \int_{-\delta}^{y^*} \rho \overline{u'^2} dy \quad (A8)$$

or

$$\tau_{\max} x = \int_{-\delta}^{y^*} \rho u (u - u_{\infty 1}) dy + \int_{-\delta}^{y^*} \rho (\overline{u'^2} - \overline{v'^2}) dy \quad (A9)$$

Equating (A6) and (A9)

$$\begin{aligned} & \int_{-\delta}^{y^*} \rho u (u - u_{\infty 1}) dy + \int_{-\delta}^{y^*} \rho (\overline{u'^2} - \overline{v'^2}) dy \\ &= \int_{y^*}^{\delta} \rho u (u_{\infty 2} - u) dy + \int_{y^*}^{\delta} \rho (\overline{v'^2} - \overline{u'^2}) dy \quad (A10) \end{aligned}$$

and by assuming $\overline{u'^2} = \overline{v'^2}$, (A10) becomes

$$\int_{y^*(x)}^{\delta(x)} \rho u (u_{\infty 2} - u) dy - \int_{-\delta(x)}^{y^*(x)} \rho u (u - u_{\infty 1}) dy \quad (A11)$$

Equation (A11) is utilized to determine the location of the dividing streamline.

Figure A4 illustrates a program that was written to check out the dividing streamline location. Data from a realistic 2-D shear layer in the form of streamwise velocity u and density ρ at normal locations y were input via DATA statements. Utilizing this data the dividing streamline was located utilizing equation (A11) which is coded in subroutine DIVSL. The jet side integral I_1 is given by the RHS of equation (A11) and the external side integral I_2 is given by the LHS of equation (A11). The trapezoidal rule is utilized for these integrals.

Detailed output for the subroutine DIVSL is given by the namelist OUT2 and for the overall check routine by OUT1. Note the location of the dividing streamline y^* given in both namelists. This illustrates a behavior common to the 2-D shear layers studied — a bending of the dividing streamline toward the jet.

Once the dividing streamline has been located, the entrainment can be calculated for both the jet side and the external side. *Figure A5* illustrates some additional calculations which define two integrals utilized in the entrainment calculations. The mass flow integration above and below the dividing streamline is given by I_3 and I_4 , respectively. These integrals are defined as

$$I_3 \equiv \int_{-\delta}^{y^*} \rho u dy \quad (A12)$$

$$I_4 = \int_{y^*}^{\delta} \rho u dy \quad (A13)$$

These integrals are utilized to calculate the mass flow changes at streamwise locations and differences in these integrals give the mass flow entrainment. The jet side integral is given by I_3 and the external side integral is given by I_4 .

Detailed output for these integrals is given in namelist OUT3. The dividing streamline location is given in namelist OUT1 and OUT2 as before.

Figure A-4. Checkout program listing for dividing streamline location.

Figure A-4. (Continued).

\$OUT2
UINr1 = .3281E+02,
UINF2 = .469E+01,
UAVG = .469465E+01,
RHOUAVG = .791555E-02,
DELY = .7999999996855E-04,
UX11 = .44190738442919E-04,
UX12 = .17279742611142E-07,
X11 = .45976435164897E-03,
X12 = .43022827818738E-03,
UEL1 = -.29536073461593E-04,
UELIS = .47861884528152E-04,
SLOPE = -.96747447525215E+00,
YY = .99997494704532E+01,
N = 22,
I = 23,
J = 51,
TEST = -.14136521374338E-08,
NMAX = 50,
\$END

Figure A-4. (Continued).

151

109

PRECEDING PAGE BLANK-NOT FILED

Figure A-5. (Continued).

```

      SUBROUTINE F1VS1      T4/T4      T4/T4      WJWDK98      04/19/79  17.14.26
      C   EVALUATE STREAMLINES FOR DIVIDING STREAMLINE
      C   HAVE ((1-L1)(1-N1)) />
      C   ((1-L1)(1-N1)) />
      C   EVALUATE STREAMLINES FOR DIVIDING STREAMLINE
      C   X1 = X13 + L13
      C   X1 = X14 + L13
      C   X1 = 5.542625*10
      C   Y01 = X13/FR(1)/DX/DY(1)
      C   Y01 = X14/H0(MUSI)/DX/DY(1)
      C   WRITE(6,0013)
      C   STOP
      C   END

      SUBROUTINE WATL1      T4/T4      T4/T4      WJWDK98      04/19/79  17.14.39
      C   INPUT OUTPUT INPUT
      C   READ(LIF,50),Y(50)
      C   50  IF (X11.LT.0.2*(K)) GO TO 10
      C   IF (X11.GT.0.2*(K)) GO TO 10
      C   IF (K.GT.10) CALL EXIT
      C   10  X11=0.2*(K-1)
      C   Y11=Y(Y(1)+FR((K-1))/((X11-X11)*(K-1)))
      C   END

```

\$OUT2
UINF1 = .3281E+02,
UINF2 = .469E+01,
UAVG = .469465E+01,
PHOAVG = .791555E-02,
DELY = .7999999996855E-04,
DXI1 = .44190738442919E-04,
DXI2 = .17279742611142E-07,
XI1 = .45976435164897E-03,
XI2 = .43022827818738E-03,
DELI = -.29536073461593E-04,
DELI3 = .47861884528152E-04,
SLOPE = -.96747447525215E+00,
YY = .99997494709532E+01,
N = 22,
I = 23,
J = 51,
TEST = -.14136521374338E-08,
NMAX = 50,
SEND

\$OUT3
UDSL = .16656950569018E+02,
FDUL = .20628433469309E-02,
UAV = .16499325284509E+02,
RAVG = .20779666734655E-02,
DELI3 = .10466898351745E-05,
XI3 = .63730432656421E-04,
XI4 = .89289814486664E-04,
VOUJ = .29198329263413E+02,
VOUE = .99315082233911E-02,
SEND

Figure A-5. (Continued).

APPENDIX B

115

PRECEDING PAGE BLANK-NOT FILMED

For the reacting shear layer comparison, it became of interest to compare the resulting temperature rise in the shear layer with that predicted by a laminar mixing model. Hence, it was necessary to add this capability to the shear layer program BOAT. The following extension to the code (*Figure B1*) is necessary to accomplish this. The details of the laminar mixing model are given in a separate report [8].

```

SUBROUTINE LAMVISC 74/74  OPT#1  WJWDRK4I  FTN 4.6+439  06/26/79
1
      SUBROUTINE LAMVISC(NS*WPSI*XMUL*T*WTMOLE,ALPHA*WTMIX)
      DIMENSION XMUL(150),XMF(125,50),T(50),WTMIX(50),
      1XMU(5),PHI(25,25),WTMOLE(25,50).
      NT=9
      DO 30 K=1,MPST
      XMUL(K)=0.
      DO 20 I=1,NS
      DO 40 J=1,NS
      40 XMF(J,K)=ALPHA(J,K)/WTMIX(K)
      CALL MUSPEC(INT(NS*T(K))/XMU())
      SUMD=0.
      DO 10 J=1,NS
      PHI(I,J)=1./SAPT(B.)*(1./WTMOLE(I)*WTMIX(J))/WTMOLE(J)*WTMOLE(I)**(-5)**2
      10 SUMD=SUMD+XMF(J,K)*PHI(I,J)
      XMUL=XMUL(I)*XMU(I)/SUMD
      20 XMUL(K)=XMUL(K)+XNUM
      30 CONTINUE
      RETURN
      END

      SUBROUTINE MUSPEC 74/74  OPT#1  WJWDRK4I  FTN 4.6+439  06/26/79
1
      SUBROUTINE MUSPEC(INT(NS*T(XMU)),
      1DIMENSION C(4,9),X(9),S(2),C1(9,5),FX(9),C2(4,9,5),XMU(5),
      2THIS DATA HAS BEEN ARRANGED ASSUMING THE SPECIES ARE READ IN THE FOLLOWING
      3ORDER - NO.03.NO2.02 - SPECIES INPUT IN ANY OTHER ORDER WILL
      4IN AN ERROR - DATA(C1)(1,1)=1,9,136,5,192,0,239,7,282,0,320,5,356,2,
      5,139,9,421,9,452,4,DATA(C1)(1,2)=1,9,131,3,177,7,217,2,252,7,285,4,315,6,
      6,134,4,0,371,0,397,1,DATA(C1)(1,3)=1,9,114,7,170,1,220,1,265,0,305,9,343,5,
      7,104,4,0,443,6,1378,8,4,12,0,443,6,DATA(C1)(1,4)=1,9,78,9,119,1,158,6,195,9,230,8,263,3,
      8,1293,9,322,8,350,1,DATA(C1)(1,5)=1,9,147,9,206,4,256,5,301,0,341,4,379,1,
      9

```

Figure B-1. Capability of the shear layer program BOAT.

```

1414 8.444 5.480 .6/
DATA NCNT/0/
IF(NCNT.EQ.0)GO TO 100
NCNT=1
N=NT
10 X1(1,1)=200.
DO 11 I=1,NT
  DO 12 J=1,NCNT
    C1(1,I,J)=C1(1,J)
11 12 CALL FNPTSL(X1,FXI,NCNT,5)
DO 13 I=1,NCNT
  DO 14 J=1,NCNT
    C1(2,I,J)=S(I,J)
13 14 CALL SPLINE(N,X1,C)
DO 15 L=1,4
  DO 16 J=1,9
    C1(2,L,J)=C1(L,J)
15 16 CONTINUE
20 NCNT=1
DO 21 I=1,NT
  DO 22 J=1,NCNT
    C1(I,J)=PCURIC(I,J,N,X1,C)
21 22 RETURN
30 CONTINUE
40 DO 41 K=1,NS
  DO 42 I=1,4
    DO 43 J=1,NT
      C1(I,J)=C2(I,J,K)
41 42 43 X1(I,J)=PCURIC(I,J,N,X1,C)
44 RETURN
END

```

119

```

SUBROUTINE CALCCF(N,X1,C)
DIMENSION X1(100),C(4,100)
DO 10 I=1,N
  DO 11 J=1,4
    X1(I,J)=X1(I,J)
10 11 DIVDF1=(C(1,I)-C(1,I-1))/DX
  DIVDF3=C(2,I)-C(2,I-1)-2*DIVDF1
  C(3,I)=(DIVDF1-C(2,I)-DIVDF3)/DX
10  C(4,I)=DIVDF3/DX
END

```

119

Figure B-1. (Continued).

Figure B-1. (Continued).

```

10      SUBROUTINE SPLINE      74/74      OPT=1      WJWDK4I      FTN 4.6+439
11      I=1+1
12      IX=NDX
13      IF (1.0E-16 .GT. IX) GO TO 30
14      DX=X-RA-B-X1*I+1
15      IF (NDX) 30, 19, 19
16      PC1=TC1*(I+1)+DX*(C12*I)+DX*(C13*I)+DX*C14*(I+1)
17      RETURN
18      END

19      I=I+1
20      IX=NDX
21      IF (1.0E-16 .GT. IX) GO TO 30
22      DX=X-RA-B-X1*I+1
23      IF (NDX) 30, 19, 19
24      PC1=TC1*(I+1)+DX*(C12*I)+DX*(C13*I)+DX*C14*(I+1)
25      RETURN
26      END

      SUBROUTINE SPLINE (N,X1;C)
      DIMENSION X1(100),C(4,100),D(100),DIAG(100)
      NP1=N+1
      DO 10 M=2,NP1
      DATA DIAG(1),D(1)/1.0,0./
      10  D(M)=X1(M)-X1(M-1)
      10  DIAG(M)=(C11,M)-C11,M-1)/D(M)
      10  DO 20 M=2,N
      11  C12,M)=3.0*(D(M)*DIAG(M+1)+D(M+1)*DIAG(M))
      12  20  DIAG(M)=2.0*(D(M)+D(M+1))
      13  DO 30 M=2,N
      14  G=-D(M+1)/DIAG(M+1)
      15  30  DIAG(M)=DIAG(M)+G*D(M-1)
      16  C12,M)=C12,M)+G*C12,M-1)
      17  NJ=NP1
      18  30  C12,NJ)=(C12,M)+G*C12,M-1)
      19  NJ=NJ-1
      20  40  M=2,N
      21  C12,NJ)=(C12,NJ)-D(NJ)*C12,NJ+1)
      22  40  RETURN
      END

```

Figure B-1. (Concluded).

REFERENCES

1. Brown, G. L. and Roshko, A., "On Density Effects and Large Structure in Turbulent Mixing Layers," *Journal of Fluid Mechanics*, Vol. 64, 1974, pp. 775-816.
2. Roshko, A., "Structure of Turbulent Flows: A New Look," *AIAA Journal*, Vol. XIV, No. 10, October 1976, pp. 1349-1357.
3. Klebanoff, P. S., "Characteristics of Turbulence in a Boundary Layer with Zero Pressure Gradient," NACA Report 1247, 1955.
4. Milinazzo, F. and Saffman, P. G., "Turbulence Predictions for the Inhomogeneous Mixing Layer," *Studies in Applied Mathematics*, Vol. 55, 1976, pp. 45-63.
5. Wallace, A. K. and Brown, G. L., "A Reacting Shear Layer with Significant Heat Release: An Experiment," Second Symposium on Turbulent Shear Flows, Imperial College, London, July 1979.
6. Brown, G. L., "The Entrainmental Large Structure in Turbulent Mixing Layers," 5th Australasian Conference on Hydraulics and Fluid Mechanics, University of Canterbury, Christ-Church, New Zealand, 9-13 December 1974.
7. Anon., *Free Turbulent Shear Flows*, Volumes I & II, NASA SP-321, Langley Research Center, July 1972.
8. Walker, B. J., "Calculation of the Laminar Viscosity of a Gaseous Mixture for Gas Dynamic Mixing Comparisons for a Reacting Shear Layer," US Army MCOM Report TR-RD-80-2, Redstone Arsenal, Alabama, October 1979.
9. Dash, S. M. and Pergament, H. S., "A Computational Model for the Prediction of Jet Entrainment in the Vicinity of Nozzle Boattails (The BOAT Code)," NASA Contractor Report 159001, Langley Research Center, Hampton, Virginia, November 1978.

REFERENCES (CONCLUDED)

10. Mikatarian, R. R., Kau, C. J. and Pergament, H. S., "A Fast Computer Program for Nonequilibrium Rocket Plume Predictions," Air Force Rocket Propulsion Laboratory Report No. AFRPL-TR-72-94, August 1972.
11. Dash, S., Weilerstein, G., and Vaglio-Laurin, R., "Compressibility Effects in Free Turbulent Shear Flows," AFOSR Report TR-75-1436, August 1975.
12. Dash, S. M., Pergament, H. S., and Thorpe, R. O., "A Modular Approach for the Coupling of Viscous and Inviscid Processes in Exhaust Plume Flows," AIAA Paper 79-0150, 17th Aerospace Sciences Meeting, New Orleans, Louisiana, January 15-17, 1979.

SYMBOLS

x	Axial Coordinate
r	Radial Coordinate
u	Axial Velocity
v	Radial Velocity
ρ	Density
Pr	Turbulent Prandtl Number, $\frac{\mu C_p}{K}$
Sc	Turbulent Schmidt Number, $\kappa / \rho D$
Le	Turbulent Lewis Number, Pr/Sc
p	Pressure
μ	Viscosity
F	$N \cdot MW$
X_i	Mole Fraction of i^{th} Species
W	Mixture Molecular Weight
h_i	Enthalpy of i^{th} Species
T	Static Temperature
h_f	Heat of Formation of i^{th} Species
k	Thermal conductivity

SYMBOLS (Continued)

w_i	Net Rate of Chemical Production of i^{th} Species
ψ	Stream Function (Equation 6)
MW	Molecular Weight
k	Turbulent Kinetic Energy, $\frac{1}{2}(u'^2+v'^2)$
α_k	Prandtl Number for Turbulent Kinetic Energy
α_ϵ	Prandtl Number for Turbulent Dissipation
ϵ, ϵ (same throughout report)	Turbulent Dissipation Rate
δ	Shear Layer Thickness
M	Mach Number
a	Sonic Velocity
\bar{k}	Compressibility Factor
ω	Pseudo-Vorticity
C_p	Heat Capacity at Constant Pressure
u_τ	Wall Shear Stress Velocity, $\sqrt{\tau_w}$
δ^*	Boundary Layer Displacement Thickness
θ^*	Momentum Thickness
γ	Ratio of Specific Heats
\bar{R}	Universal Gas Constant
R	$\bar{R} \cdot \text{MW}$
Λ	Defined in Equation 1
H	Enthalpy

SYMBOLS (Continued)

$C_{\epsilon 1}$	kc2 Turbulence model constants (Equations 10 and 11)
$C_{\epsilon 2}$	
C_{μ}	
a_k	
a_c	kc ω Turbulence model constants (Equations 18-20)
$C_{\omega 1}$	
$C_{\omega 3}$	
$C_{\omega 4}$	
$C_{\omega 5}$	Empirical constants in kc2 formulation
C_{k1}	
C_{k0}	
C_{μ}	
$C_{\epsilon 1}$	Functional corrections for weak shear flows in kc2 formulation (Ref. 7)
$C_{\epsilon 2}$	
\tilde{P}/ϵ	
F	
e	Specific turbulent kinetic energy
P	Defined by Equation 25
ω	Cole's Universal Wave Function (Equation 29)
τ_w	Wall shear stress
δ^*	Displacement thickness
η	Non-dimensional radial coordinate, $\frac{r - r_j}{r_e - r_j}$
θ	Momentum thickness
y	Cross stream distance from dividing streamline

SYMBOLS (Concluded)

β'	Constants in $k\omega'$ formulation
α'	
α''	
C_1	
C_2	
C_3	
C_4	
C_5	
C_6	
U	Mean axial velocity
V	Mean radial velocity
z	ω^2
ν	μ/ρ

Subscripts

max	Maximum
o	Initial value
c	Centerline
e	External stream
j	Jet stream
∞	Free stream
t	Turbulent

DISTRIBUTION

	<u>No. of Copies</u>		<u>No. of Copies</u>
University of Illinois Dr. A. L. Addy 208 Mechanical Engineering Laboratory Urbana, IL 61801	1	Aerochem Research/Princeton Dr. Hartwell Calcote PO Box 12 Princeton, NJ 08540	1
BMDATC ATC-14, Dr. Larry C. Atha PO Box 1500 Huntsville, AL 35807	1	Rockwell International Rocketdyne Division Code D/536, Mr. R. Campbell 6633 Canoga Avenue Canoga Park, CA 91304	1
Rockwell/Downey Mr. Harold J. Babrov Space Information Systems Division 12214 Lakewood Blvd Downey, CA 90241	1	Aerojet Solid Propulsion Company Attn: Mr. James P. Coughlin Mr. A. W. McPeak PO Box 13400 Sacramento, CA 95813	1
Bell Aerospace Corporation Mr. Arthur H. Blessing PO Box 1 Buffalo, NY 14240	1	SAI/Princeton Attn: Dr. Sanford M. Dash Dr. E. S. Fishburne 1101 State Road, Bldg 11 Princeton, NJ 08540	1
Calspan Corporation Attn: Dr. Donald W. Boyer Dr. Paul V. Marrone Dr. Walter H. Wurster PO Box 400 Buffalo, NY 14221	1	Grumman/Bethpage Grumman Aerospace, Inc. Attn: Dr. Paul D. Del Guidice Dr. Stanley Rudman S. Oyster Bay Road Bethpage, LI, NY 11714	1
Physics Dynamics/La Jolla Dr. Frederick P. Boynton PO Box 556 La Jolla, CA 92038	1	ARC/Alexandria Dr. Mark Director 5390 Cherokee Avenue Alexandria, VA 22314	1
Naval Weapons Center Attn: Code 3245, Mr. S. Breil Code 3241, Mr. A. Victor China Lake, CA 93555	1	Hercules/Cumberland Aerospace Division-Allegany Ballistics Laboratory Attn: Mr. Thomas E. Durney Mr. Robert C. Foster PO Box 210 Cumberland, MD 21502	1
Naval Ordnance Station Attn: Code 5252E, Mr. G. Buckle Code 5233D, Mr. H. Hodgkins Indian Head, MD 20640	1	AFATL/DLMQ Dr. D. E. Ebeoglu Eglin AFB, FL 32542	1
Spectron/Costa Mesa Dr. C. W. Busch 3303 Harbor Blvd Costa Mesa, CA 92626	1	University of Tennessee Space Institute Attn: Dr. W. Michael Farmer Dr. James M. Wu Dr. Kenneth E. Harwell Tullahoma, TN 37388	1
AFRPL/PACP Attn: Dr. David Mann Dr. T. D. McCay Edwards AFB, CA 93523	1		

DISTRIBUTION (Continued)

United Technologies Corporation Chemical Systems Division Mr. B. R. Felix PO Box 358 Sunnyvale, CA 94088	1	Martin-Marietta Corporation Mr. Larry B. Blow Mail Stop 0482 PO Box 179 Denver, CO 80201	1
Ford Aerospace & Commercial Corporation Aeronautic Division Attn: Mr. Alson C. Frazer Mr. L. E. Horowitz Ford & Jamboree Roads Newport Beach, CA 92663	1	AFAPL/RJA Mr. Norman A. Hirsch Wright-Patterson AFB, OH 45433	1
Photon Research Associates, Inc. Attn: Dr. G. Newton Freeman Dr. Claus B. Ludwig PO Box 1318 La Jolla, CA 92038	1	Naval International Interpretational Service Center (NISC) Code 452, Mr. James Hyland 4301 Suitland Road Washington, DC 20390	1
Aerodyne Research, Inc. Attn: Dr. Michael E. Gersh Dr. James S. Draper Crosby Drive Bedford Research Park Bedford, MA 01730	1	Thiokol Chemical Corporation Wasatch Division Mr. M. J. Janis Brigham City, UT 84302	1
Johns Hopkins University Applied Physics Laboratory-Chemical Propulsion Information Agency Attn: Mr. Theodore M. Gilliland Mr. Andreas V. Jensen Johns Hopkins Road Laurel, MD 20810	1	Aerospace Corporation Attn: Dr. Richard H. Lee Dr. Duane Nelson Dr. Ronald R. Herm PO Box 92957 Los Angeles, CA 90009	1
NASA-Marshall Space Flight Center Attn: Code ED-33, Dr. T. Greenwood Technical Library Mr. Joseph L. Sims Huntsville, AL 35812	1	Lincoln Laboratory/MIT Dr. J. Lowder PO Box 73 Lexington, MA 02173	1
United Technologies Corporation Research Center Dr. Roy N. Guile 400 Main Street East Hartford, CT 06108	1	AFSC/FTD Attn: Mr. S. Marusa Mr. R. Farnolli Wright-Patterson AFB, OH 45433	1
McDAC/Huntington Beach Attn: Dr. Donald W. Harvey A3-328, Library Dept 204/13-3, Mr. G. F. Greenwald 5301 Bolsa Avenue Huntington Beach, CA 92647	1	Naval Missile Center Mr. D. E. Papche Code 5351 Point Mugu, CA 93042	1
	1	Lockheed Missile & Space Company Attn: Mr. Morris M. Penny Ms. Beverley J. Audeh Mr. L. Ring PO Box 1103 Huntsville, AL 35802	1
	1	AFGL (OPR) Mr. B. P. Sandford Hanscom AFB, ME 01731	1

DISTRIBUTION (Continued)

Environmental Research Institute of Michigan Dr. L. M. Peterson PO Box 8618 Ann Arbor, MI 48107	1	AEDC/DOT Attn: Mr. E. Thompson Dr. Herman E. Scott Arnold AFS, TN 37389	1
General Dynamics-Pomona Division Attn: Mr. E. T. Piesik Technical Library PO Box 2507 Pomona, CA 91766	1	AFOSR LT Robert F. Sperlein Bldg 40 1	
Chrysler Corporation Michoud Defense Space Division Mr. E. A. Rawls PO Box 29200 New Orleans, LA 70189	1	Bolling AFB Washington, DC 20332	
Physical Sciences, Inc. Mr. Curt Ray 30 Commerce Way Woburn, MA 01801	1	Naval Weapon Space Center Code 5042, Dr. J. E. Tanner Crane, IN 47522	
Remtech, Inc. Dr. John S. Reardon 2603 Arties Street Huntsville, AL 35805	1	Armament R&D Command Attn: DRDAR-IC, Mr. J. Tyroler Dover, NJ 07801	
ARO, Inc. Arnold Engineering Development Center Attn: Mr. Robert P. Rhodes Dr. Wheeler K. McGregor Dr. Charles C. Limbaugh Mr. W. D. Williams Mr. R. C. Bauer Dr. C. E. Peters Technical Library Arnold AFS, TN 37389	1	Thiokol Chemical Corporation Dr. C. Mikkelsen Huntsville, AL 35807	
NASA/JSC Code EX-3, Mr. B. B. Roberts Houston, TX 77058	1	TRW, Inc. Attn: Mr. Orvil E. Witte Dr. John T. Ohrenberger One Space Park Redondo Beach, CA 90278	
ARDC CPT William E. Rothschild Code XRB Eglin AFB, FL 32542	1	Institute of Defense Analysis Dr. Hans G. Wolfhard 400 Army-Navy Drive Arlington, VA 22202	
Army Ballistic Research Laboratories Attn: DRDAR-ELL, Mr. E. Schmidt Aberdeen Proving Ground, MD 21005	1	Defense Advanced Research Projects Agency Dr. Stephen Zakanycz 1400 Wilson Blvd Arlington, VA 22209	
	1	Commander Air Force Armament Laboratory Mr. C. Butler Eglin AFB, FL 32542	
	1	Air Force Flight Dynamics Laboratory Attn: FDMM, Mr. Gene Fleeman Wright-Patterson AFB, OH 45433	
	1	US Air Force Academy CAPT Brilliant, DFAN USAF Academy, CO 80840	

DISTRIBUTION (Continued)

Commander	Jet Propulsion Laboratory
Naval Surface Weapons Center	California Institute of Technology
White Oak Laboratory	Attn: Mr. R. Martin
Attn: Code WA-41, Dr. W. Yanta	1 Mr. R. Kenneth Baerwald
Code WO, Mr. E. Elzufon	1
Silver Springs, MD 20910	4800 Oak Grove Drive
	Pasadena, CA 91109
 NASA-Langley Research Center	Boeing Company
Attn: Code MS423, Mr. R. Wilmoth	1 Attn: Library Unit Chief
Mr. Charles Jackson	1 Mr. R. J. Dixon
Technical Library	1 Mr. H. L. Giles
Hampton, VA 23665	1 Mr. J. M. Barton
	PO Box 3707
Commanding Officer and Director	Seattle, WA 98124
Naval Ship Research and	
Development Center	
Attn: Aerodynamic Laboratory	Vought Corporation
Craderock, MD 20007	1 Attn: Mr. C. R. James
	1 Mr. D. B. Schoelerman
	1 Mr. Richard Summerhays
	Box 5907
NASA-Ames Research Center	1 Dallas, TX 75222
Attn: Mr. G. S. Deiwert 202A-1	1
Technical Library	
Moffet Field, CA 94035	
 NASA-Lewis Research Center	Lockheed Aircraft Corporation
Attn: Mr. M. A. Beheim	Missile and Space Division
Technical Library	Attn: Technical Info Center
Cleveland, OH 44315	1 Dr. Dwayne A. Sheets,
	1 Org 62-13, B-104
	PO Box 504
Sandia Corporation	Sunnyvale, CA 94086
Sandia Base Division 9322	
Mr. W. Curry	Martin-Marietta Corporation
Box 5800	Orlando Division
Albuquerque, NM 87115	1 Attn: J. Burns
	1 L. Gilbert
	1 Dr. L. Sakell
University of Notre Dame	PO Box 5837
Department of Aerospace Engineering	Orlando, FL 32804
Dr. T. J. Mueller	1
Notre Dame, IN 46556	
 Naval Air Systems Command	McDonnell-Douglas Corporation
Mr. William Volz	Attn: Technical Library
Air 320-C, JP-1	1 PO Box 516
Washington, DC 20361	1 St. Louis, MO 63166
 Nielsen Engineering & Research, Inc.	Northrop Corporation
Dr. Jack N. Nielsen	Electro-Mechanical Division
850 Maude Avenue	1 Mr. E. Clark
Mountain View, CA 94040	1 500 East Orangethorpe Y20
	Anaheim, CA 92801
 Director of Defense Rsch & Engng	Rockwell International
Room 3C128, Technical Library	Columbus Aircraft Division
The Pentagon	1 Mr. Fred Hessman
Washington, DC 20301	1 4300 East Fifth Avenue
	Columbus, OH 43216

DISTRIBUTION (Concluded)

Hughes Aircraft Company	DRSMI-LP, Mr. Voigt	1
Missile Systems Division	DRSMI-R, Dr. McCorkle	1
Mr. J. B. Harrisberger	-RK	1
Canoga Park, CA 91304	-RL	1
	-RR	1
US Army Materiel Systems Analysis	-RN	1
Activity	-RS	1
Attn: DRXSY-MP	-RDK	1
Aberdeen Proving Ground, MD 21005	-RDK, Dr. Walker	20
	-RPR	15
	-RPT (Reference Copy)	1
	(Record Copy)	1

DATE
ILMED
- 8